WESLEYAN UNIVERSITY

Swirling Superfluid ^{4}He Films

by
Crista Louise Wilson

A Thesis Submitted to the Faculty
of Wesleyan University in partial fulfillment of
the requirements for the degree of Doctor of Philosophy

Middletown, Connecticut

May, 1998

Thanks to Fred, who was absolutely indispensible, Ralph and Rollie for invaluable assistance, Dave, for feeding me, and Tom and Rose for feeding Molly.

Table of Contents

Chapter 1: Introduction

Overview of Thesis 1

Two Fluid Model, Superfluids 4

Sound in ^{4}He Films 6

Vortices 7

Chapter 2: The Experimental Cell and Driven Wave Information

Cell Geometry and Function 9

Experimental Techniques 11

Bessel's Equations and Modes of Oscillation 13

Applications of Cell Geometry and Bessel Functions 14

Dispersion Relation

Fluid Dynamics

Power Calculation

High Amplitude Third Sound Waves and Overdriven Modes 24

Mode Shapes and Different Ways to Plot Them 25

Mode Splittings 31

Chapter 3: Vortex Dynamics

Pinning and Drag Forces, 34

Vortex Interaction with Moving Fluid,

and Induction of Flow

Chapter 4: Programs and Models

Splitting Prediction Program 39

Flow Field Prediction Program 49

Non-linear Waves

Comparison to Experiment

Comparison to Classical Drift

Chapter 5: Effects of High Amplitude Waves

(1,1) Non-Linear Down Crashes and Duffing's Equation 63

(2,1) Linear and Non-Linear Crashes (Surfs and Down Crashes) 68

Power and Drag Force Analysis 73

Appendices:

A. Cell Building Procedures 91

B. Capacitor Experiment to Determine Film Thickness 95

C. MathCad Documents 102

D. Three Calculations of Wave Amplitude 112

E. Surfing Simulation and Results 114

BIBLIOGRAPHY 123

CHAPTER 1

Introduction

Helium appears to present several exceptions to the laws of Classical Mechanics, making it exceedingly interesting to physicists. The most easily understandable of its unexpected behaviors is helium's refusal to solidify at reasonable pressures, even at absolute zero. All elements other than helium are solid below 4.2 K at any pressure. ^{4}He, the most common isotope of helium and the subject of this thesis, liquefies at 4.2 K but remains a liquid unless a pressure greater than 25 atmospheres is applied (figure 1-1). Helium is difficult to crystallize because the atoms have a low binding energy. To form a solid, the helium atoms must be forced together against the zero point motion so that they fall into the shallow, narrow potential well of the diatom (figure 1-2).

After the process was developed to liquefy helium in 1908, it was commonly used to cool superconductivity experiments. The researchers, whose primary concern was not their refrigerant, had noticed that the fluid stopped boiling and that odd leaks appeared below 2.2 K, but they had left these phenomena unstudied until about 1938. The first experiments by Kapitza and at the same time by Allen and Misener (1938) demonstrated the existence of "superleaks," where helium was capable of flowing though submicron channels with no pressure difference between the ends. The lack of a pressure head indicated that the fluid had no viscosity, unlike any other known fluid. Kapitza coined the term "superfluid" that year. Later, persistent currents, flows in the superfluid that never slow down, were discovered by Reppy and Depatie (1964) in helium in a packed powder filled torus, and by Henkal et al. (1968) in helium films. Both studies confirmed the lack of viscous drag.

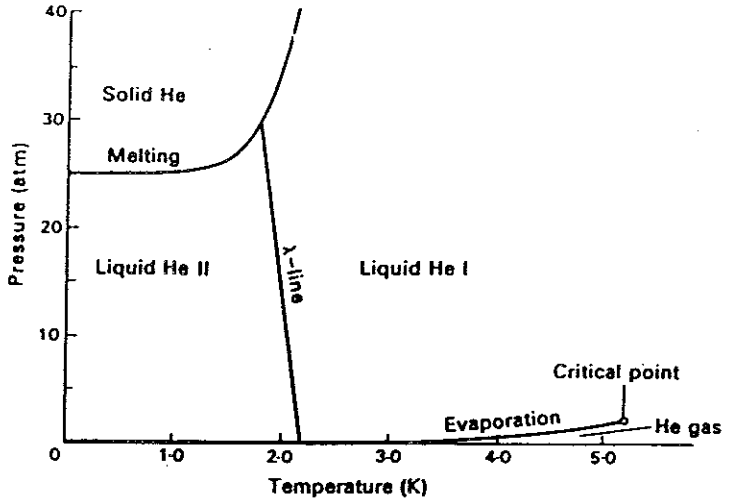

Figure 1-1: Phase diagram of helium (after Tilley 1974).

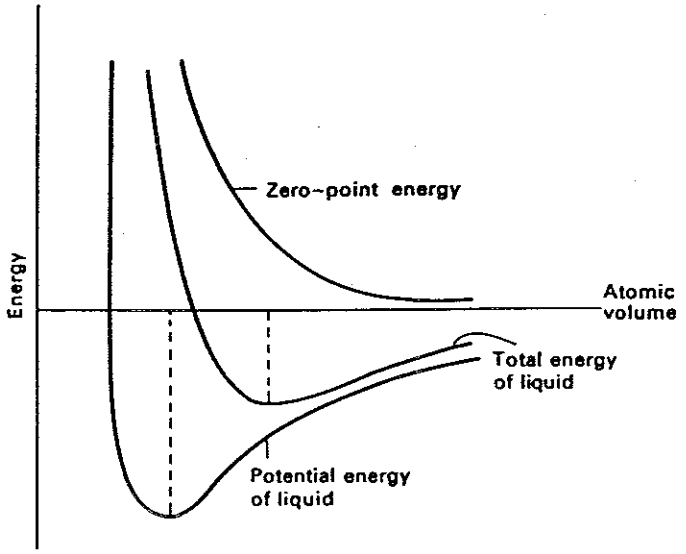

Figure 1-2: Potential energy well for helium atoms (after Tilley 1974).

Another experiment, by Allen and Jones (1938), took advantage of superleaks to explore heat transfer in liquid helium. They found that helium prefers to have no temperature variation in a film or in bulk. They constructed a superleak out of a tube filled with packed powder and attached it to a reservoir of liquid helium. When they heated the end of the superleak, the superfluid flowed through the leak to cool the heated region. If more heat was applied, the superfluid squirted out of the leak as it flowed faster to supply more cooling. Their result was dubbed the fountain effect, and demonstrated what came to be called the thermomechanical effect. The latter is important to our later discussion of waves traveling on superfluid films.

Helium makes a film on most substrates because the van der Waal's attraction to the substrate exceeds the surface tension of the fluid. Any fluid under similar conditions will wet the surface it is touching and form a film, but in helium there are some unusual side effects. Because the superfluid has no viscosity, it can spread much farther. The film can form a siphon to reduce its potential, so that superfluid in a bucket will make a film that can flow up and out of the container, and down the sides, emptying the bucket. Researchers wishing to work with certain amounts of bulk helium or specific film thicknesses must eliminate helium's escape routes by sealing their apparatus.

In our experiment, we seal a small container with the correct amount of helium inside to evenly coat the interior with a uniform film. Our purpose is to study how persistent currents in helium films can be changed. We have shown that a high amplitude wave traveling on the film can induce a circulation of fluid in our cell.
For a complete understanding of the mechanisms involved, the two fluid model, sound waves in helium, and vortices must be introduced.

The Two Fluid Model

Up until this point, I have discussed only experiments that showed that helium has no viscosity. When other researchers tried dragging objects through the fluid, they found a viscous drag force. This paradoxical evidence can be explained by helium's ability to act as a combination of normal fluid and superfluid. The two fluids are actually two different states in the liquid. Because ^{4}He is a boson, and any number of bosons can populate an energy level, a bulk population of only two states is possible. The ground state acts as the superfluid component, sometimes called a "quantum fluid" for the rules it follows, and the higher states act together as a classical fluid. The lowest level is a Bose condensate and is described by the Bose-Einstein distribution function for the number of atoms in a particular energy level:

$$n(\varepsilon) = \frac{1}{e^{\frac{\varepsilon-\mu}{kT}} - 1} \qquad 1\text{-}1$$

where n is the population of the state, ε is the energy state, μ is the chemical potential, k is Boltzman's constant, and T is the temperature. For any state above the ground state, as temperature drops, the denominator goes towards infinity and the energy level population falls to zero. When the energy is extremely close to the chemical potential, as it is for the ground state, the denominator approaches zero, and the population explodes.

The switch between one extreme and the other occurs at the transition temperature, T_λ (figure 1-3). Experimentally, the transition occurs at 2.17 K; the Bose-Einstein theory is suprisingly close with a prediction of 3.1 K, using the liquid density instead of the gas density and considering the non-ideal nature of the helium atom.

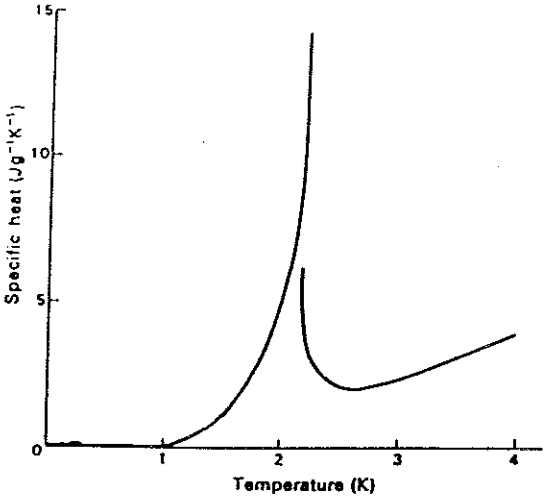

Figure 1-3: Heat capacity of helium (after Tilley, 1974). The graph resembles the greek letter lambda, and thus the singularity is referred to as the lambda transition.

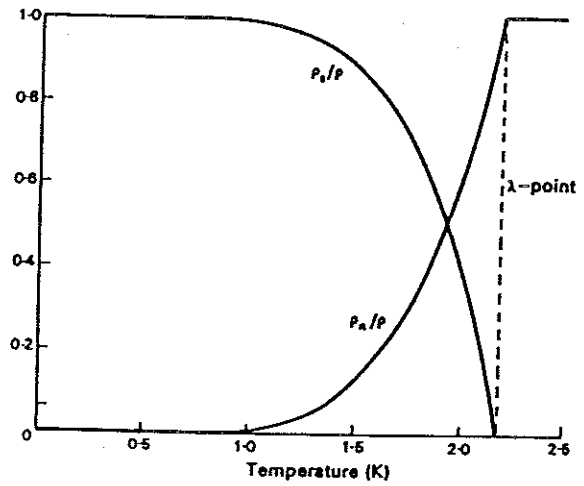

Figure 1-4: An experiment by Andronikashvili using a torsional pendulum (after Tilley, 1974) demonstrated from the oscillation frequency of the pendulum that the concentration of the superfluid and normal fluid varies as a function of temperature. The pendulum had very closely spaced disks hung on a wire, and the normal fluid between the disks caused a drag that decreased as the temperature dropped and more of the fluid became superfluid.

Figure 1-4 illustrates the ratio of the ground state fraction to the excited state fraction as a function of temperature as found by Andronikashvili (1946). Using many stacked disks suspended from a wire, Andronikashvili constructed a torsional pendulum whose oscillation frequency varied as a function of temperature. The disks were closely spaced so that normal fluid would be unable to move between them, and he was able to determine the ratio of normal fluid to superfluid by monitoring the frequency changes. The results indicated that below 1 K, essentially all the fluid is superfluid. This is the realm in which we work.

Sound in ^{4}He Films

The odd coexistence of the two types of liquid helium allows waves to travel in several ways through films or bulk helium. The most familiar methods of propagation are those for first sound and third sound. First sound is exactly the same kind of compression wave that occurs in air, and it occurs in both components of the fluid working together. It is characterized by density changes and no temperature variation. Third sound is a pressure wave that is relieved by surface motion and exists in superfluid only. The normal fluid is fixed. It is the same as a gravity, or shallow water, wave but also has a temperature oscillation, which is a common way to detect it. The troughs of the wave are warmer than the peaks because there is less superfluid present, and superfluid flows toward warm places to cool them. The troughs are the next peak locations, which sets up a standing wave. Both of these kinds of sound are fairly easily understood because their motions at least are the same as those found in fluids such as air and water, although the actual mechanics are very different.

Other types of sound in liquid helium travel in unexpected ways. The less familiar versions are second sound and fourth sound. Both require different actions from

superfluid and normal fluid. Second sound is a temperature wave. The superfluid and normal fluid fractions oscillate out of phase, so there is more normal fluid in some areas and more superfluid in others, but the fluid density remains constant. The various ratios are related to specific temperatures in the concentration graph (figure 1-3), resulting in the temperature wave, but here there are no surface effects. Fourth sound is a pressure wave in the superfluid in a porous medium where the pore size is small enough that the normal fluid cannot move, but the superfluid can. Because there is no free surface, there are temperature and density waves as well. There are even more types of wave travel than these, but they are even stranger, and will be left to the reader to discover.

Vortices

The last and most important part of our experiment to be introduced here is vortices, without which we could not have superfluid circulation. Vortices arise from the fact that the superfluid fraction is made up of ground state atoms, for which we can write the wavefunction as an amplitude and a phase

$$\Psi=\Psi_0 e^{\phi(r)}. \qquad 1\text{-}2$$

where Ψ_0 is a constant amplitude and $\phi(r)$ is the phase. By the Bohr Sommerfeld condition, integration of the phase changes around a loop in space must result a multiple of 2π. The phase $\phi(r)$ may be written as kl, the wave vector times a length and integrated:

$$\oint k \cdot dl = 2\pi n. \qquad 1\text{-}3$$

From there we may use a substitution for the momentum, $\hbar k = mv$, to change variables to the velocity:

$$\oint v \cdot dl = \frac{h}{m_4} n \quad , \qquad 1\text{-}5$$

and assuming n = 1, complete the integral around a circular loop:

$$v \cdot 2\pi r = \frac{h}{m_4} \qquad 1\text{-}6$$

When we solve for the velocity of the fluid,

$$v = \frac{\hbar}{m_4 r} \hat{\phi} \qquad 1\text{-}7$$

we get the velocity field of a vortex. A vortex is a line around which fluid flows quickly close to the core and slowly far away. Depending on our choice of n, we can choose any number of vortices to be enclosed in the integration loop; they are quantized such that whatever the strength of the velocity field, it must be a multiple of $\hbar/m_4$. To be strictly accurate, an arrangement of many vortices in one place is unstable because they repel each other. A collection of vortices near each other produces the same flow field as the bunched vortices when observed from outside the loop enclosing them.

This thesis describes our experiments on the interaction between third sound waves and vortices. Different distributions of vortices in our experimental cell maintain different flow fields around its interior. When the waves and the velocity fields of the vortices interact, the vortices may move. Wave amplitude data and vortex configuration information taken before and after the wave has passed allow us to determine how much power is used to move the vortices. Our power data indicates that vortices can move in two different fashions, and currently we have no model that can explain both behaviors.

CHAPTER 2

The Cell and Wave Driving Information

The experimental cell in which we study flow in superfluid helium films is a small, hollow disk. On the top and bottom of the disk are capacitor plates. Because the helium film is a weak dielectric, the changing electric fields between the capacitor plates make waves in the film. The amplitude and frequency of the waves can be detected using another capacitor, and from the amplitude measurements a myriad of information can be deduced.

The waves caused by the changing fields are third sound waves, and the chamber is often referred to as the third sound resonator. As was mentioned in Chapter 1, third sound waves are analogous to shallow water waves, but the restoring force is the van der Waal's attraction to the substrate instead of gravity. The films are in general about 3 nm thick (around 10 layers of atoms), and the radius of the cell is about 1 cm, so the wavelength of the third sound is very much greater than the film thickness. The film thickness oscillations can be as small as a fraction of a layer or as large as a third of the film thickness.

The cell is located under the mixing chamber of a homemade dilution refrigerator (Kittel, 1980) that we usually run at 100 mK. The cell that has been used for all the experiments in this work except for the film thickness calibration in Appendix B was constructed in 1991. The capacitors in the cell are arranged in a circle, with the plates made of 100 nm thick gold film. The gold was deposited on glass pieces using thermal evaporation (see Appendix A). When the gold was evaporated, one of the pieces was masked to make one circular plate, and the other was divided into five

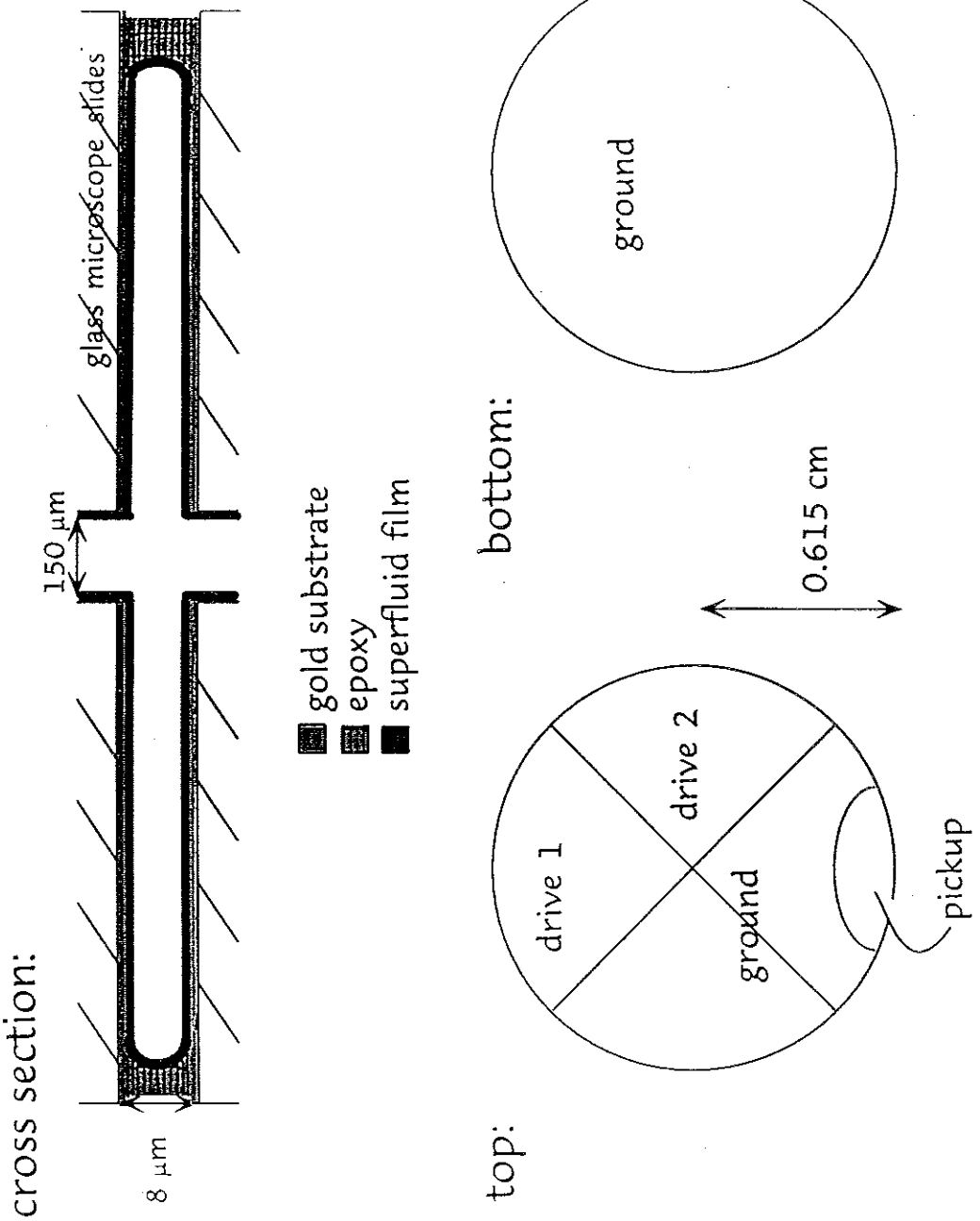

Figure 2-1: Sketch of the third sound resonator

regions. When the two pieces were placed face to face, they formed five capacitors. The circular area containing the capacitors was then sealed with glue so that the resonating film is enclosed in a hollow disk (figure 2-1).

Third sound waves are driven in the cell by the capacitors because helium is a weak dielectric and feels a force per unit mass when it is in a changing electric field.

$$\vec{f} = -\frac{1}{2}\frac{(\varepsilon - \varepsilon_0)}{\rho}\vec{\nabla}E^2 \qquad 2\text{-}1$$

where ε is the dielectric constant of helium, ε_0 is the permittivity of free space, ρ is the density of liquid helium, and E is the electric field between the capacitor plates. Restated, an AC voltage applied across a capacitor pulls a dielectric into the capacitor region. Two of the capacitors in the cell are used in this way to drive third sound waves in the cell. A single drive can be used to excite a standing wave, or the two drives can be used together to drive a rotating wave if they are driven out of phase. The traveling wave moves around the cell in the $\pm\hat{\phi}$ direction, depending on the phase of the drivers, through all the capacitors. Similarly, another of the other capacitors serves as the pickup. As the level of the helium in the pickup capacitor changes as a wave travels in the cell, so changes its capacitance. The pickup is part of an LC circuit that oscillates at 76 MHz, and the changes in capacitance are translated into a frequency. Standard RF detection equipment is used to detect the frequency change on the 76 MHz carrier wave. This arrangement allows us to determine the amplitude of the third sound wave, something that groups using temperature to track the waves cannot do.

Experimental Techniques

The amplitude information that we collect from the pickup comes in terms of a

magnitude and a phase relative to the resonance being examined. This data is usually tracked as a function of time or of frequency. After a resonance has been driven and the drive is turned off, the resonance amplitude decays in an exponential free decay. A recording of the film displacement as a function of time yields the frequency and the Q of the resonance. The same frequency and Q information can be gathered by turning on the drive at low voltage and stepping the frequency across the resonance and collecting amplitude vs. frequency data.

A free decay is the fastest way to characterize a resonance, but it is only useful if the resonance is easy to drive. A combination of high frequency, about 1000 Hz, and a Q lower than about 20,000 is typical of a resonance that decays too fast to produce accurate data. The drive oscillator must be set very close to the resonance, if not on it, so that a drive under about 15 V (of a 30 V maximum) can excite a raw amplitude of about .5 mV. At that point the drive is turned off and the amplitude and time are recorded. When the amplitude falls, the amplitude and time are recorded again, and from the two points, the Q is found.

$$Q = -2\pi f_D \frac{t_2 - t_1}{\ln A_2 - \ln A_1} \qquad 2\text{-}2$$

where f_D is the drive frequency, and t_1, t_2, A_1, and A_2 are the initial and final times and amplitudes. If the drive was set on resonance, the phase stays constant during the decay. If it drifts, the rate of drift can be used to determine how far the drive frequency is from the resonance:

$$\Delta f = \frac{1}{4\pi}\frac{d\phi}{dt}. \qquad 2\text{-}3$$

The standard program for this type of data is CheckFQ. It takes many free decays, adjusting the drive frequency according to any drift each time, and averages the results when the operator stops it, typically after about 4 iterations for Q's around

30,000.

Stepping the frequency with a fixed drive amplitude and recording the wave amplitude is the best way to find frequency and Q data when the resonance is difficult to drive because it can be fitted very accurately. Taking 10 or more seconds at each point can average out noise that obscures free decay shapes. However, the frequency range of the scan must include the tails of the peak, so these scans can take the greater part of an hour.

Bessel's Equation and Modes of Oscillation

The resonances are standing waves set up in the cell. Because the cell is circular, the shapes of the waves are determined by Bessel's equation, which we can derive using the equations of motion of the superfluid:

$$\frac{\partial h}{\partial t} = -\vec{\nabla} \cdot (h\vec{v}) \qquad 2\text{-}4$$

$$\frac{\partial v}{\partial t} + (\vec{v} \cdot \vec{\nabla})\vec{v} = -g\vec{\nabla}h \qquad 2\text{-}5$$

where h is the film thickness, g is the van der Waal's force between the fluid and the substrate, and v is the velocity of a particle of fluid. Equation 2-4 is the continuity equation and merely states that if fluid is flowing into (out of) a region, the height must increase (decrease). Equation 2-5, Euler's equation, is more difficult to interpret because of the convective derivative term but is in fact Newton's second law. The convective derivative arises because we work mathematically with particles of fluid instead specific locations in the film (Kundu, 1990). By assuming an oscillatory film thickness and velocity,

$$h = h_o(r) + \eta e^{im\phi} e^{-i\omega t} \qquad 2\text{-}6$$

$$\vec{v} = \left(\hat{r}v_r(r) + \hat{\phi}v_\phi(r)\right)e^{im\phi}e^{-i\omega t}, \qquad 2\text{-}7$$

we can make substitutions in the continuity and Euler equations to derive the equations of motion in terms of $\frac{\partial \eta}{\partial r}, \frac{\partial v_r}{\partial r}$, and v_ϕ. Ignoring non-oscillatory and second order terms, the combination of these results forms Bessel's equation:

$$r^2\frac{d^2\eta}{dr^2} + r\frac{d\eta}{dr} + \left(k^2r^2 - \omega^2\right)\eta = 0. \qquad 2\text{-}8$$

The wave amplitude, η, is a Bessel function, and thus the modes of oscillation are similar to the familiar drumhead modes except the edges of the fluid are free to move.

The modes are referenced as the number of angular node lines first and then the number of radial antinodes. The modes that we drive most frequently are the (1,1), (2,1), and (3,1), but we have in the past been able to reach as high as the (11,1) (figure 2-2). The geometry of the cell prevents us from coupling to multiples of the (4,1). At thinner films the mode frequencies are higher and the Q's of the resonances are lower, and the modes are thus harder to detect. Also, as the number of radial nodes increases, the possibility of the thickness oscillations from a wave canceling out over the drive and pickup regions increases, and the modes are accordingly more difficult to drive and find.

Applications of Cell Geometry and Bessel Functions

The third sound wave speed can be found using the cell geometry, the dispersion relation, and the measured frequency.

$$\omega = ck \qquad 2\text{-}9$$

where ω is the resonance frequency, c (or c_3) is the third sound speed, and k is the wavenumber. k can be replaced using a standard substitution in Bessel equations:

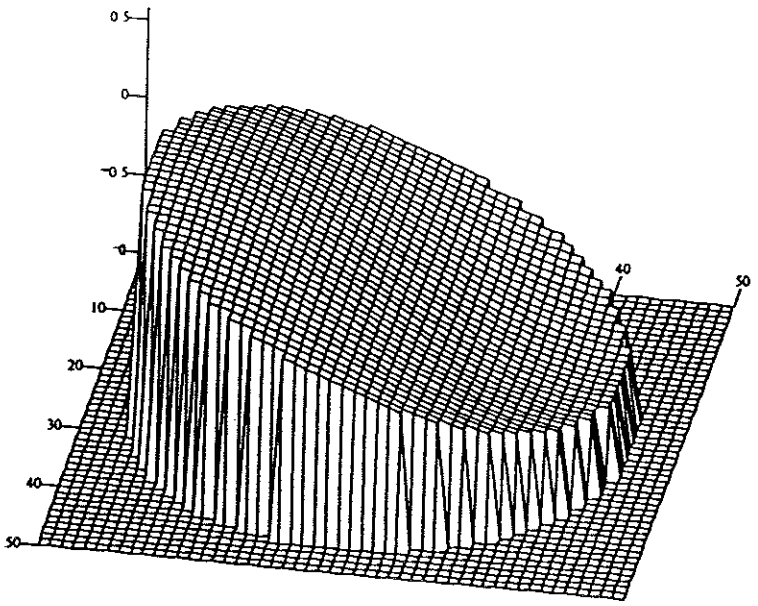

Figure 2-2a: The (1,1) and (2,1) modes of oscillation of the film in the resonator.

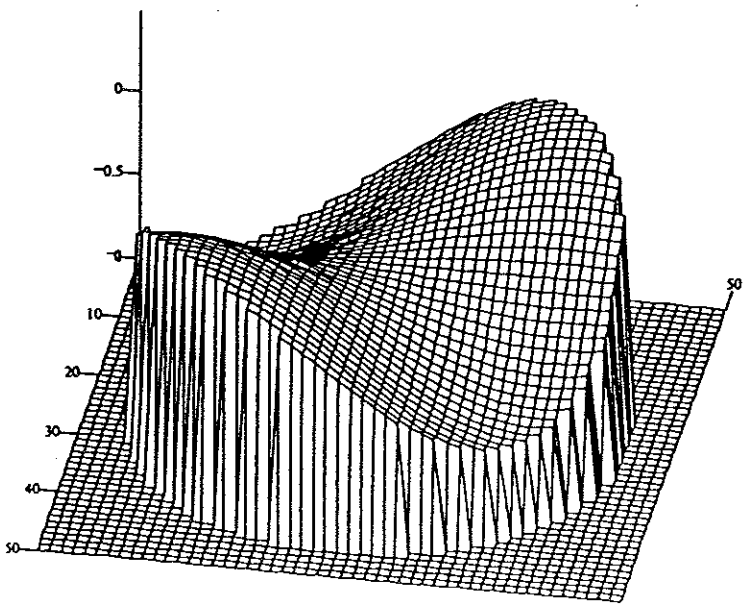

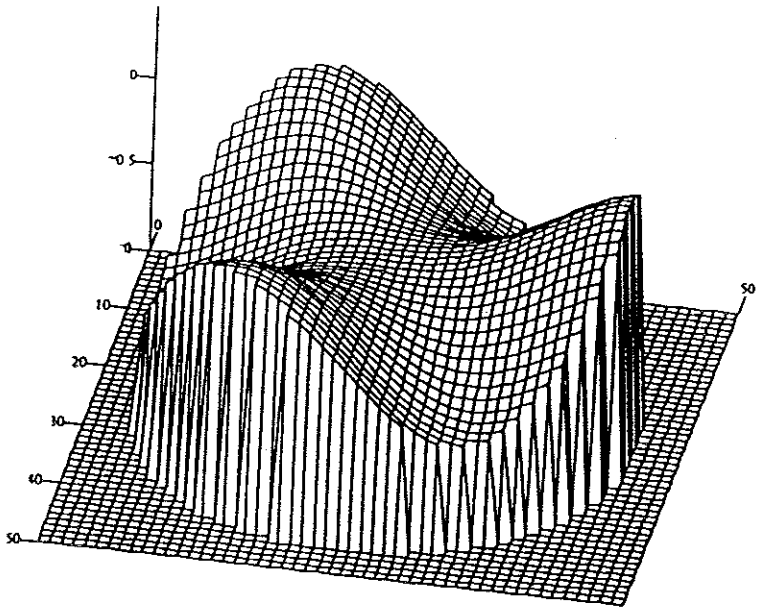

Figure 2-2b: The (3,1) and (1,2) modes.

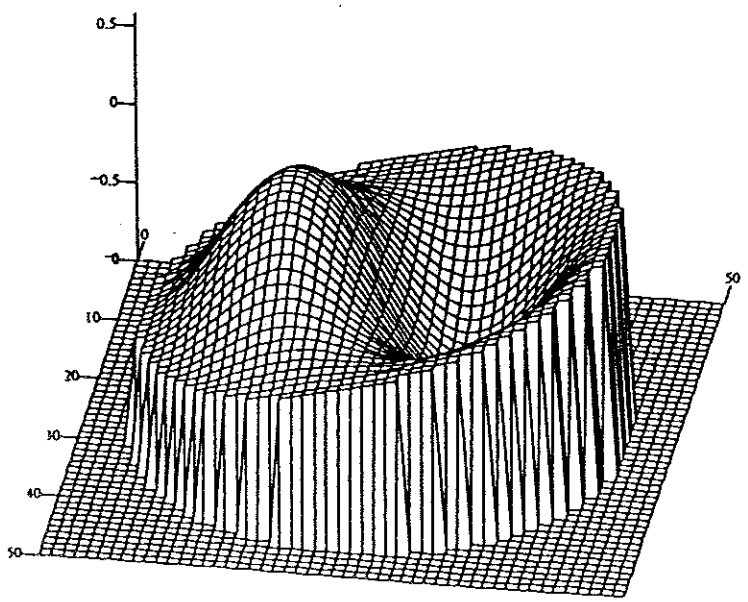

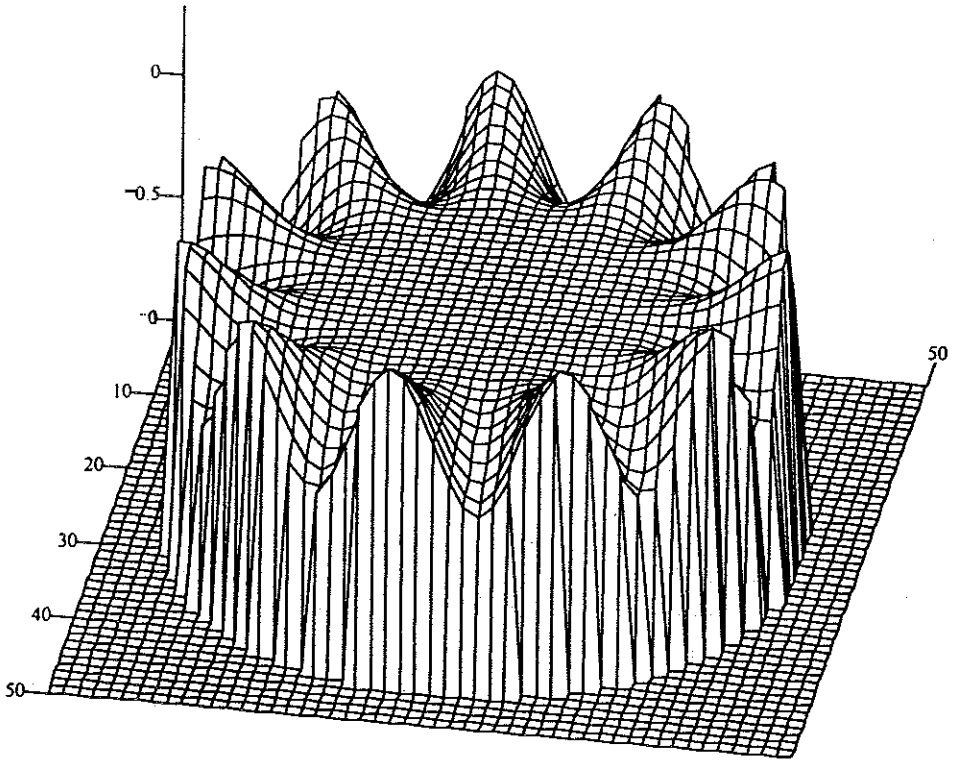

Figure 2-2c: The (11,1) mode. This is the highest mode we have detected to date. The pickup capacitor is more likely to be overlapped by many ripples of the (11,1), causing cancellation and making higher modes more difficult to detect.

$kr = x$. At the outer radius of the cell

$$ka = x_{mn}, \qquad 2\text{-}10$$

where a = 0.00615 m, the radius of the cell, and x_{mn} is the argument value required for the derivative of Bessel function to be zero, as it must be at the edge. With this information, we can write the third sound speed in terms of the experimental frequency and some constants

$$c_3 = \frac{\omega a}{x_{mn}}. \qquad 2\text{-}11$$

In reality, the film responds at twice the drive frequency, so $\omega = 2\pi(2f_D) = 4\pi f_D$. The electric field oscillates at ω, but the force on the film is from the square of the field. The squared sine function of the drive generates the frequency doubling.

The third sound speed is related to the film thickness by

$$c = \sqrt{gh} \qquad 2\text{-}12$$

where g = the acceleration of a helium atom toward the gold substrate from the van der Waal's attraction between the two, and h is the film thickness. (This formula also works for water waves, using gravity and water depth (Kundu 1990).)

g can be found from the Van der Waal's potential between a point and a plane.

$$U = -\frac{\alpha}{z} \qquad 2\text{-}13$$

where α is the binding energy per atom, and z is the distance from the atom to the substrate. α can be rewritten in terms of the binding energy and the atomic size:

$$U = -\frac{\varepsilon_B}{m_4}\left(\frac{z_1}{z}\right)^3 = -\frac{k_B T_V}{m_4}\left(\frac{z_1}{z}\right)^3. \qquad 2\text{-}14$$

where $z_1 = \left(\frac{m_4}{\rho}\right)^{\frac{1}{3}}$ and $\rho = {}^4\text{He}$ density at .1 K.

By taking the derivative of the potential

$$g = \left(\frac{\partial}{\partial z}U(z)\right)\Big|_h \qquad 2\text{-}15$$

and using 2-12,

$$c_3{}^2 = h\left(\frac{\partial}{\partial z}U(z)\right)\Big|_h = \frac{3k_B T_V}{m_4}\left(\frac{z_1}{h}\right)^3 \qquad 2\text{-}16$$

we find a simple relation between the film thickness and the wave speed. In fact, to be extremely accurate, there are many factors that can be included:

$$c_3{}^2 = \frac{\rho_s}{\rho}\left(\frac{h-d}{h}\right)\frac{3k_B T_V}{m_4}\left(\frac{z_1}{z}\right)^3 \frac{1}{\left(1+\frac{z}{z_r}\right)} \qquad 2\text{-}17$$

where $\frac{\rho_s}{\rho} = 1$ because we work lower than 1 K, d = the boundary layer, a layer that cannot move because the wavefunction must go to zero at the substrate, and z_r = the retarded potential. (The retarded potential comes from $1/z^3$ -> $1/z^4$ at large distances, approximately 40 layers.) Generally we use equation 2-16 with the value of T_V found in Appendix B.

Using the film thickness, amplitude information, and an understanding of the force on a dielectric, we can directly calculate the power used in driving a wave around the cell. The power is the time average of the force on the film times the fluid velocity. The electric field from the capacitors can be found and used to find the force on the film. Equations 2-4 and 2-5 yield amplitude and velocity information. The derived expression for power can be rewritten in terms of the experimental relative amplitude,

the phase relative to resonance, and a collection of factors that come from Bessel functions and geometry.

Mathematically we find the power by taking the time average of the force on the film dotted into the fluid velocity and integrating over the volume of the cell.

$$P = \int \langle f \cdot v \rangle_{time} dV \qquad 2\text{-}18$$

We can derive the force, assuming the electric field between the plates is

$$E_1^{\,2}(r,\phi) = \sum_{m=-\infty}^{\infty} \sum_{n=-\infty}^{\infty} A_{mn} J_m(k_{mn} r) e^{i(m\phi - \omega t)} \quad \text{for D1} \qquad 2\text{-}19$$

and

$$E_2^{\,2}(r,\phi) = \sum_{m=-\infty}^{\infty} \sum_{n=-\infty}^{\infty} B_{mn} J_m(k_{mn} r) e^{i(m\phi - (\omega t + \phi_0))} \quad \text{for D2.} \qquad 2\text{-}20$$

where ϕ_0 is inserted into equation 2-14 because the two drive plates are driven out of phase. To isolate and determine A_{mn}, we need to separate the time dependence and apply orthonormality relations to equation 2-19. We multiply both sides by $J_n(x)e^{-in\phi}$ and integrate over the area of the drive:

$$\int_0^{2\pi} \int_0^{a} \sum_{m,n} A_{mn} J_m(x) J_n(x) e^{im\phi} e^{-in\phi} r dr d\phi = \frac{V^2}{g^2} \int_0^{\frac{\pi}{2}} \int_0^{a} e^{-in\phi} J_n(x) r dr d\phi \qquad 2\text{-}21$$

where

$$x \equiv k_{mn} r$$

$$E_1^{\,2}(r,\phi) = \begin{cases} \frac{1}{2}\frac{V^2}{g^2} & 0 < \phi < \frac{\pi}{2} \\ 0 & \frac{\pi}{2} < \phi < 2\pi \end{cases}$$

(the electric field must only exist in the quadrant of the drive plate)

g = the size of the gap

$$\int_0^{2\pi} e^{im\phi} e^{-in\phi}\, d\phi = 2\pi\delta_{m,n}$$

and

$$\int J_m(x_{mn}) J_m(x_{mn}) x dx = \frac{1}{2x_{mn}^2}(x_{mn}^2 - m^2)\left(J_m(x_{mn})\right)^2$$

(Abramowitz and Stiegun, 1972).

Dividing through, we solve for A_{mn}.

$$A_{mn} = \frac{\frac{V^2}{g^2}\frac{i}{mk_{mn}^2}\left((-i)^m - 1\right)\int_0^{x_{mn}} J_m(x) x dx}{2\pi\frac{a^2}{x_{mn}^2}\left(x_{mn}^2 - m^2\right)\left(J_m(x_{mn})\right)^2} \qquad 2\text{-}22$$

$$= \frac{1}{2}\frac{V^2}{g^2}\frac{i}{m\pi}\left((-i)^m - 1\right)\frac{\int_0^{x_{mn}} J_m(x) x dx}{\left(x_{mn}^2 - m^2\right)\left(J_m(x_{mn})\right)^2}\,. \qquad 2\text{-}23$$

Similarly,

$$B_{mn} = \frac{1}{2}\frac{V^2}{g^2}\frac{i}{m\pi}\left((-1)^m - (-i)^m\right)e^{i\phi_D}\frac{\int_0^{x_{mn}} J_m(x) x dx}{\left(x_{mn}^2 - m^2\right)\left(J_m(x_{mn})\right)^2} \qquad 2\text{-}24$$

where in this case $E_2{}^2(r,\phi)$ is non-zero from $\frac{\pi}{2}$ to π, which is accounted for by ϕ_D.

With these parameters, we can find the force:

$$\vec{f} = -\frac{1}{2}\frac{(\varepsilon - \varepsilon_0)}{\rho}\vec{\nabla}E^2 \qquad 2\text{-}25$$

where

$$E^2 = E_1^{\,2} + E_2^{\,2}\,, \qquad 2\text{-}26$$

and E^2 represents the spatial electrical influence.

Having established a way to find the force, the next step to finding an expression for the power is to derive an expression for the fluid velocity. Using equation 2-5, the velocity can be found from the amplitude of the wave oscillation

$$\eta = \eta_0 J_m(x) e^{i(m\phi - (\omega t - \phi_{res}))}\,. \qquad 2\text{-}27$$

ϕ_{res} accounts for the wave motion being shifted 45° relative to the way the drive plates were defined. By looking at only the oscillatory terms and eliminating second order terms, Newton's second law can be rewritten as the following:

$$\frac{\partial \vec{v}}{\partial t} = -g\vec{\nabla}\eta\,. \qquad 2\text{-}28$$

g in this case is the acceleration from the van der Waal's attraction to the substrate. At this point we could take the gradient in equation 2-28 and integrate to find the velocity, but it is far easier mathematically to leave equation 2-28, and for that matter equation 2-25, as they are.

The original expression for the power can be written as an integral over the mass instead of the volume:

$$P = \int \langle f \cdot v \rangle_{time} dM\,. \qquad 2\text{-}29$$

To that we may apply Green's first identity:

$$\int_V \vec{\nabla}\phi \cdot \vec{\nabla}\psi \, dV = \int_S \phi \, \hat{n} \cdot \vec{\nabla}\psi \, dS - \int_V \phi \, \nabla^2\psi \, dV \qquad 2\text{-}30$$

so that

$$P = \frac{1}{2}\mathrm{Re}\int \phi \nabla^2 \psi dM\,. \qquad 2\text{-}31$$

Let

$$\phi = -\frac{1}{2}\frac{(\varepsilon - \varepsilon_0)}{\rho}E^2 \qquad 2\text{-}32$$

so that

$$\vec{f} = \vec{\nabla}\phi \qquad 2\text{-}33$$

and

$$\psi = \frac{g}{i\omega}\eta \qquad 2\text{-}34$$

so that

$$\vec{v} = \vec{\nabla}\psi\,. \qquad 2\text{-}35$$

The first term in 2-30 is zero because there is no velocity component normal to the surface, i.e., outside the cell. Now the power can be written as an area integral:

$$P = \frac{1}{2}\left(\frac{1}{2}\frac{(\varepsilon - \varepsilon_0)}{\rho}\right)\left(\frac{g}{i\omega}\right)\int E^2\bar{\nabla}^2\eta^*\rho h dA \qquad 2\text{-}36$$

$$= \frac{\pi}{2}\frac{(\varepsilon - \varepsilon_0)c_3^{\,2}}{i\omega}\int_0^{x_m}\left(A_{mn}J_m(x)e^{i(m\phi-\omega t)} + B_{mn}J_m(x)e^{i(m\phi-(\omega t-\phi_D))}\right)\eta_0 J_m(x)e^{-i(m\phi-(\omega t+\phi_{res}))}xdx \qquad 2\text{-}37$$

$$= \frac{1}{8}\frac{(\varepsilon - \varepsilon_0)c_3^{\,2}\eta}{\omega m}\frac{V^2}{g^2}\mathrm{Re}\left\{\left((-i)^m - 1 + \left[(-1)^m - (-i)^m\right]e^{i\phi_D}\right)e^{i\phi_{res}}\right\}\int_0^{x_{mn}}J_m(x)xdx \qquad 2\text{-}38$$

$$= \frac{1}{2}\frac{(\varepsilon - \varepsilon_0)c_3^{\,2}\eta}{\omega m}\frac{V^2}{g^2}\sin^2\left(\frac{m\pi}{4}\right)\int_0^{x_{mn}}J_m(x)xdx \qquad 2\text{-}39$$

where we have neglected the subscript on η. We may define P_0 as the power required to maintain an oscillation that empties and fills the cell to a height h:

$$P_0 = \frac{1}{4}\omega C_0 V_0^2\frac{h}{g}\left(1 - \frac{\varepsilon_0}{\varepsilon}\right) \qquad 2\text{-}40$$

where

$$C_0 = \frac{\varepsilon_0\pi a^2}{g}. \qquad 2\text{-}41$$

A compact form for the power emerges:

$$P = \xi_m P_0 \frac{\eta}{h} \cos(\phi - \phi_{res}) \qquad 2\text{-}42$$

where

$$\xi_m = \frac{2}{m\pi x_{mn}^2} \sin^2\left(\frac{m\pi}{4}\right) \int_0^{x_{mn}} J_m(x) x dx \qquad 2\text{-}43$$

for maximized signal for each mode. The form in equation 2-42 was chosen because the geometrical constants, Bessel constants, and the experimentally measured quantities, amplitude and phase, are all represented in separate terms.

High Amplitude Third Sound Waves and Overdriven Modes

We use the power calculation to analyze the results of driving high amplitude third sound waves, waves with amplitudes one-quarter to one-third of the film thickness, around the cell. Most of the experiments in the following chapters involve driving these waves to change the circulation of the film. Prior to these experiments, a drive of only 10 V was used across the drive capacitors, and the circulation state of the film could not be changed. Increasing the drive voltage to 30 V with the addition of a transformer box gives us the power to change the circulation with any of the three lowest modes, but not all the time. At thin films we are unable to swirl any of the modes, but as the frequencies decrease and Q's increase with increasing film thickness, the lowest frequency modes begin to respond, until at very thick films our ability to swirl again drops off. Using geometric considerations we concluded that to drive the (1,1) and (3,1) modes the drive plates should be 90° out of phase (ϕ_0 in equation 2-20), but logically we could not decide between driving the (2,1) with 90° or 180° since neither should couple. Experimentally we have determined that 180° is the optimum phase.

Mode Shapes and Different Ways to Plot Them

To understand our swirling models, it is necessary to first study resonance behavior. The simplest resonance structure is the simple harmonic oscillator, where

$$m\ddot{x} = -kx, \qquad 2\text{-}44$$

and the solution is

$$x = x_0 e^{i\omega t}. \qquad 2\text{-}45$$

Adding both a driving force and some damping makes the amplitude more complicated:

$$m\ddot{x} = -kx - \gamma\dot{x} + f_0 e^{i\omega t} \qquad 2\text{-}46$$

$$x = \frac{\frac{f_0}{m} e^{i\omega t}}{\omega^2 - \omega_0^2 + i\frac{\omega\omega_0}{Q}}. \qquad 2\text{-}47$$

where ω_0 is the resonance frequency and Q is a measure of the resonance decay time. The amplitude can be plotted one of two ways. The standard graph is of amplitude as a function of frequency, which is a Lorentzian curve. Figure 2-3a is an example of a Lorentzian curve slightly distorted by a background signal. That amplitude is a combination of the real and imaginary parts of the data (figure 2-3b). The amplitude can also be plotted as the imaginary part vs. the real part, which more readily reveals phase information (figure 2-4), as it yields a circle (figures 2-5 and 2-6). The beginning of the circle, to the right of the origin, is where the driving frequency is well below the resonance, and a mass on a spring would oscillate in phase with the driver. As the driving frequency approaches resonance, it steps faster in phase, and the steps are farthest apart on resonance where a mass would oscillate ninety degrees out of phase. As the phase swings to 180° out of phase, where the frequency is too high, it completes the circle.

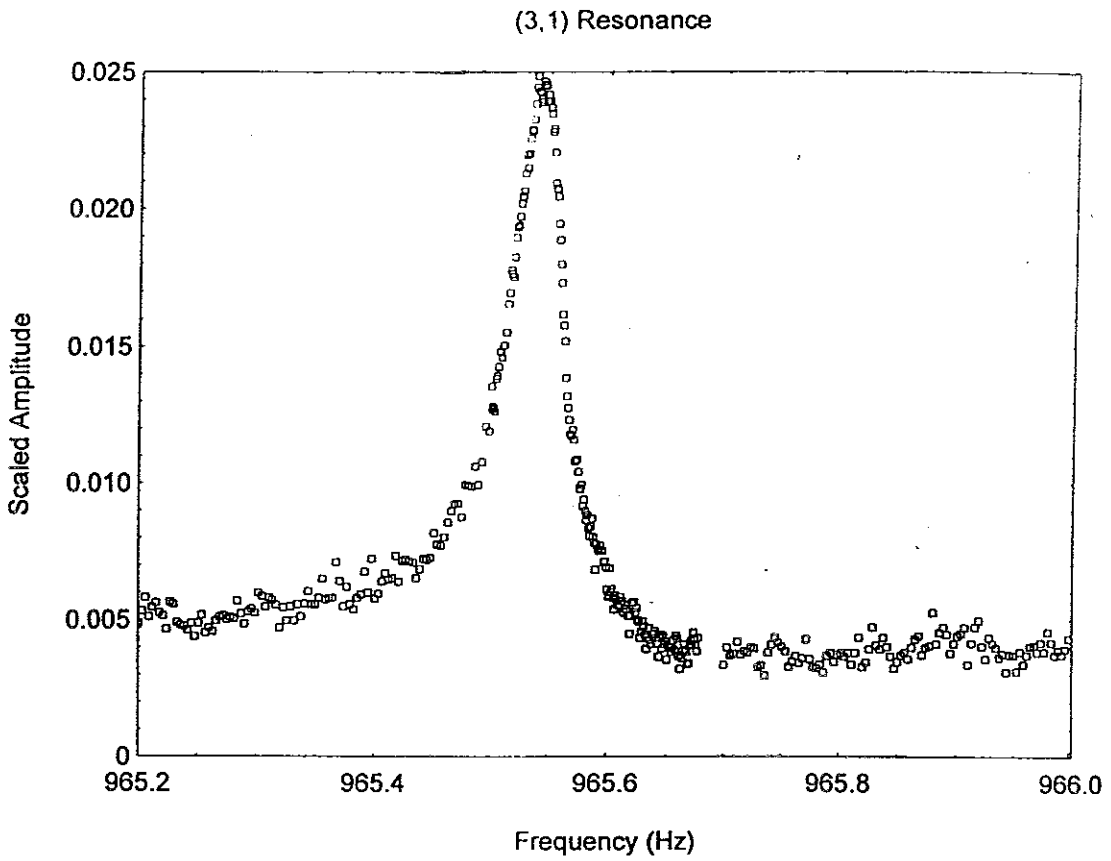

Figure 2-3a: Amplitude data from a scan of the frequency over the (3,1) mode shows the expected Lorentzian line shape.

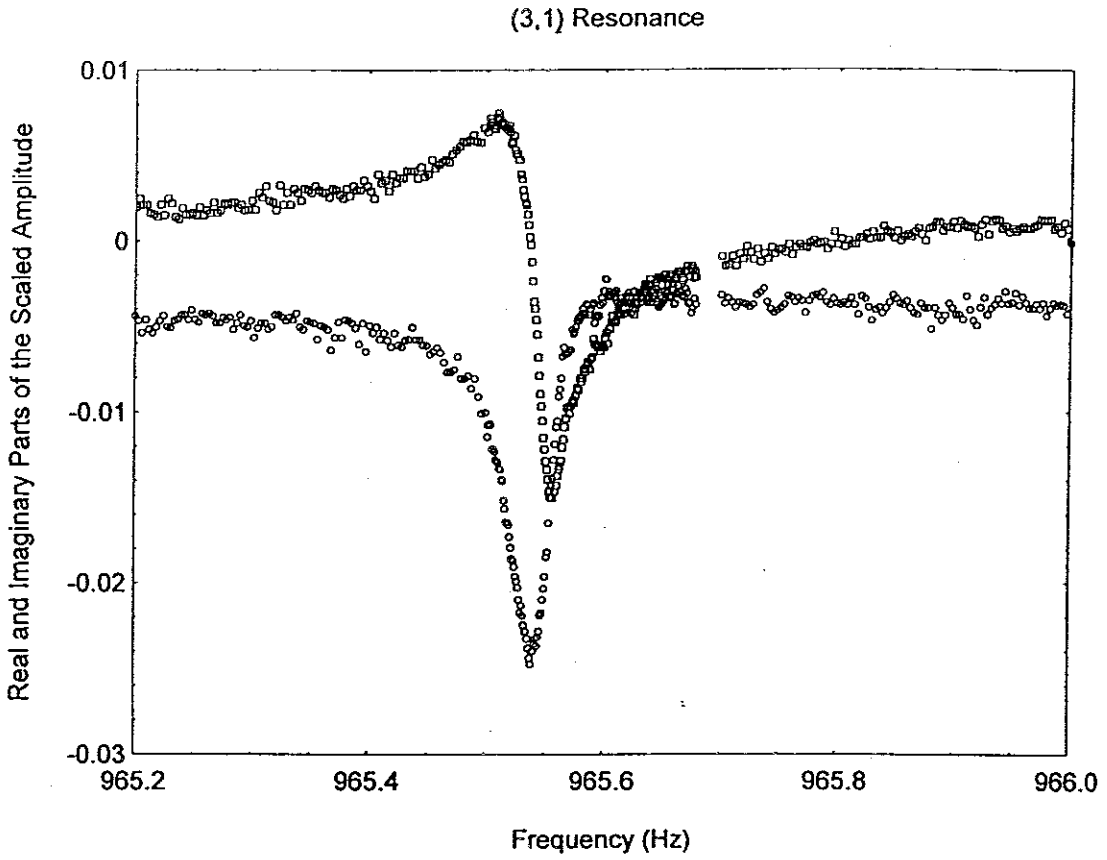

Figure 2-3b: A plot of the real and imaginary parts of the resonance amplitude as a function of frequency.

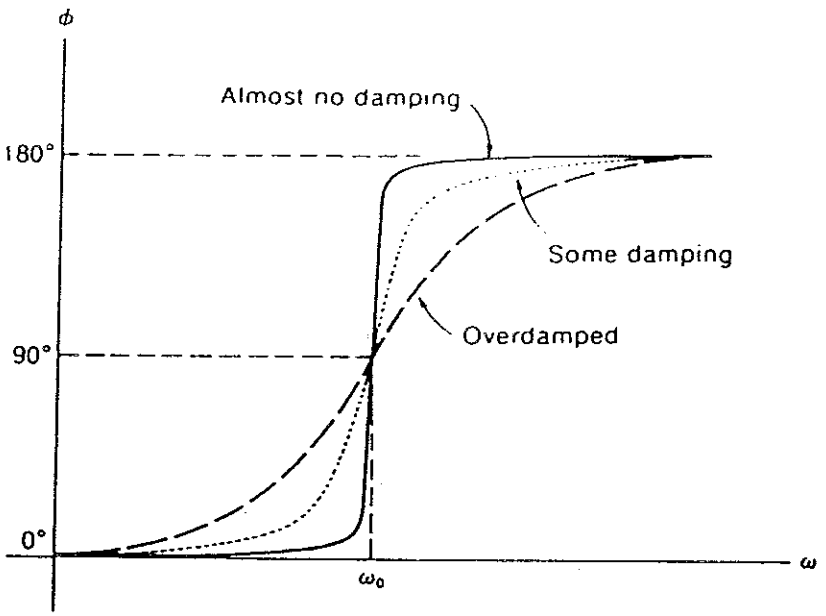

Figure 2-4: Phase of a resonance as a function of frequency.

$$\eta := \left[\frac{\eta_0}{1 - \left(\frac{\omega}{\omega_0}\right)^2 + \frac{i \cdot \omega}{\omega_0 \cdot Q}} \right] \cdot e^{-i \cdot \omega \cdot t}$$

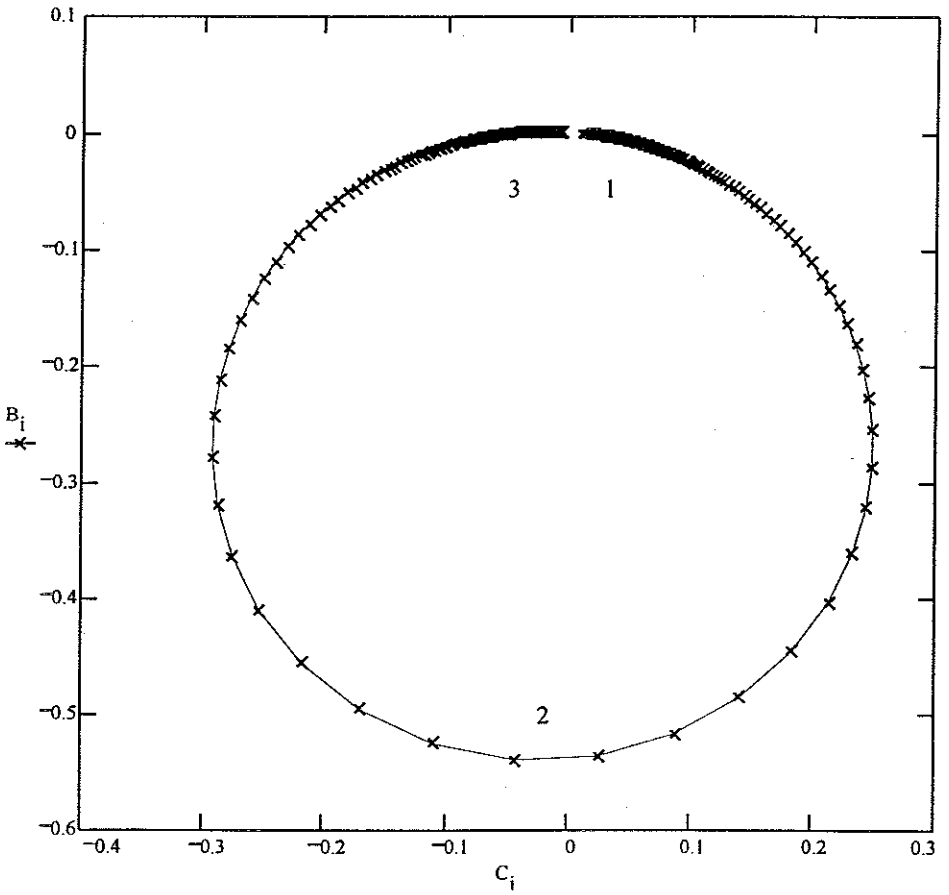

Figure 2-5: resonance plotted as real and imaginary components.

1. Below resonance, the theoretical mass oscillates in phase with the driver.
2. On resonance, the system is 90^0 out of phase. The steps in frequency are constant throughout the scan, but the phase changes more rapidly on resonance, so the points on the graph are spread out.
3. Above resonance, the system is 180^0 out of phase with the driver.

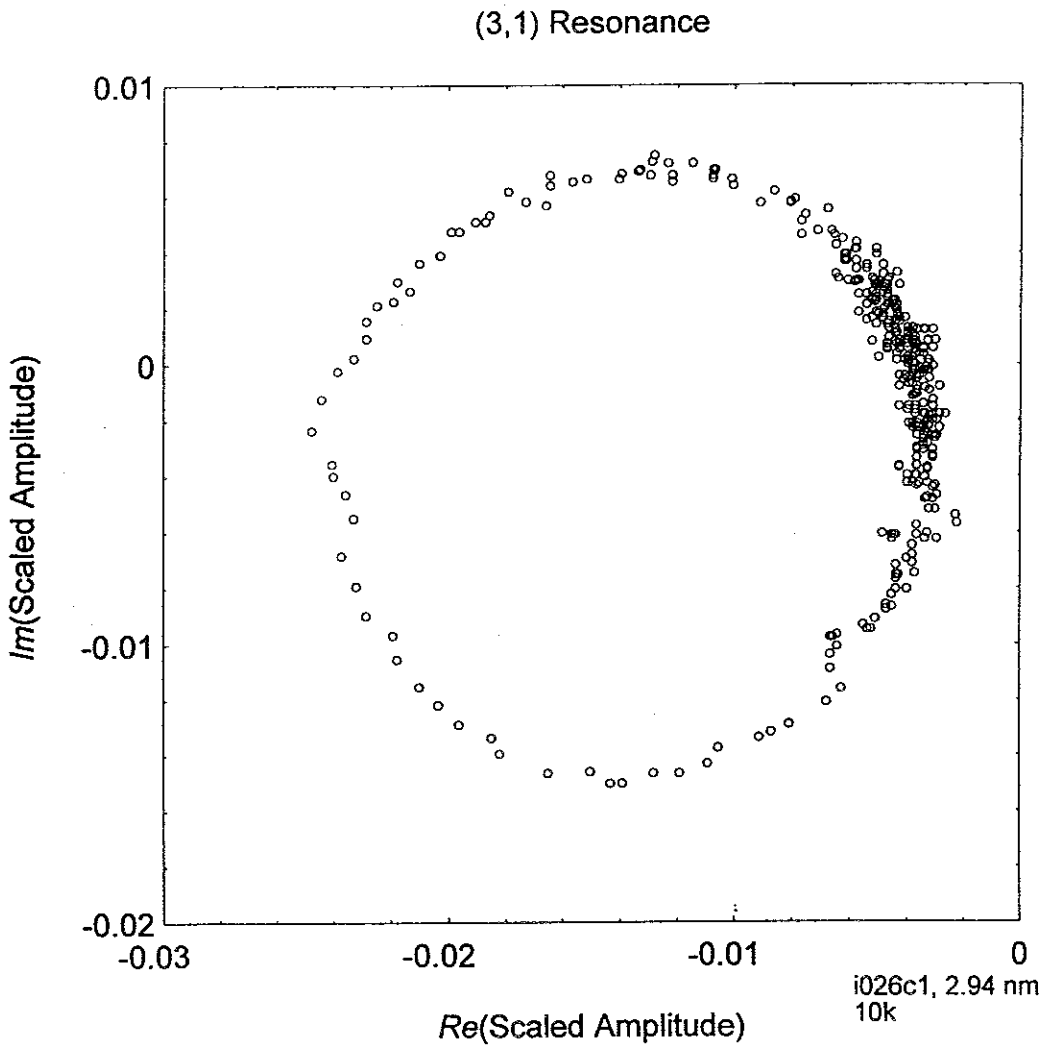

Figure 2-6: Data from figure 2-3a, plotted as the real and imaginary parts

There is a background signal and phase shift that offsets and rotates the circle depending on its direction and magnitude at the resonance frequency. The background comes from the phase shifts and other complications from the electronics. We can easily subtract the background at a point near the resonance, but the circle may still be rotated; it is still easy to fit and extract the frequency, Q, and other relevant data.

Mode Splittings

In an ideal, quiescent film, a wave can travel around the cell in either direction in the same amount of time. If the film has been swirled, the two modes split; one frequency is Doppler shifted up, and the other down. By measuring the splittings of several modes we can determine the velocity field of the circulation state inside the cell.

Even when there is no flow in the cell there is still a small splitting that can be explained by asymmetries in the cell—imperfect alignment of the holes in the two glass pieces or a non-circular glue seal. Typical non-swirled splittings are $6x10^{-4}$ for the (1,1), $3x10^{-4}$ for the (2,1), and $2x10^{-4}$ for the (3,1). When the film is swirled, these geometrical splittings are negligible, but it is useful at small splittings to be able to separate the swirling splitting from the geometrical one.

A useful model is that of a two level system. The model assumes two energy levels far from the rest but close to each other, a situation that is exactly related to the splitting of one mode. When a perturbation is introduced, such as a DC flow in the cell, the effects on the modes are predictable. (This is very reasonable, except in the case of the (1,2) mode, which interacts with the (4,1), which if we had a perfect cell,

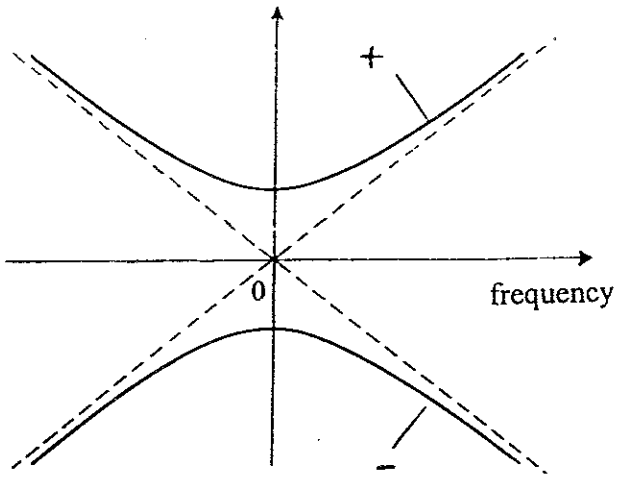

Figure 2-7: Splitting diagram. Because of geometrical asymmetry in the cell, the splitting can never be zero. The upper and lower modes instead follow the hyperbolic paths when the circulation is changed.

we could not see.) This analysis results in a picture of the energy splitting where the split modes do not split linearly but each branch follows a hyperbola (figure 2-7). Thus we can separate the two kinds of splittings:

$$\begin{aligned} \delta &= \pm\sqrt{\gamma^2 + \Delta^2} \\ &= \pm\frac{\Delta\omega}{\omega} \end{aligned} \qquad 2\text{-}48$$

where γ = splitting from flow, and Δ = splitting from geometry. (For more information, please see Cohen-Tannoudji (1977) or Luo (1992).)

CHAPTER 3

Vortex Pinning, Drag, and Interactions with Moving Fluid

Background information about vortex motion and pinning is required before the models of Chapter 4 or the power analysis in Chapter 5 can be understood. The first step towards this goal is to understand the substrate on which the vortices move. We have examined the gold substrate in our cell with a scanning tunneling microscope [Darryl's thesis] and have modeled the surface as a collection of Gaussian hills. Because of surface tension, the film is slightly thinner over a hill, reducing the length of a vortex line on the hill. With less fluid involved in its motion, the vortex has a smaller kinetic energy. This energetically favorable preference for hills among vortices is called pinning. (It is also possible that vortices pin to defects in the gold, for which we have not constructed a model.)

To unpin a vortex, a force must be applied, and the only force available comes from a flow of fluid past the vortex. The vortex is a rotational velocity field, and if it is placed in a constant linear flow, on one side of the vortex the velocities will add, and on the other they will cancel. The resulting force from the pressure differences [Bernoulli's law] is called the Magnus force (figure 3-1).

$$\vec{F}_m = \rho\kappa h\hat{z} \times (\vec{v} - \vec{v}_s) \qquad 3\text{-}1$$

where ρ = the superfluid density, $\kappa = \frac{h}{m_4}$ (the quanta of circulation), v is the velocity of the vortex core (not to be confused with the rotational velocity field of the vortex), v_s is the background superfluid velocity, and the z-axis is aligned with the vortex core and is perpendicular to the substrate. The pinning force can be modeled as a static friction

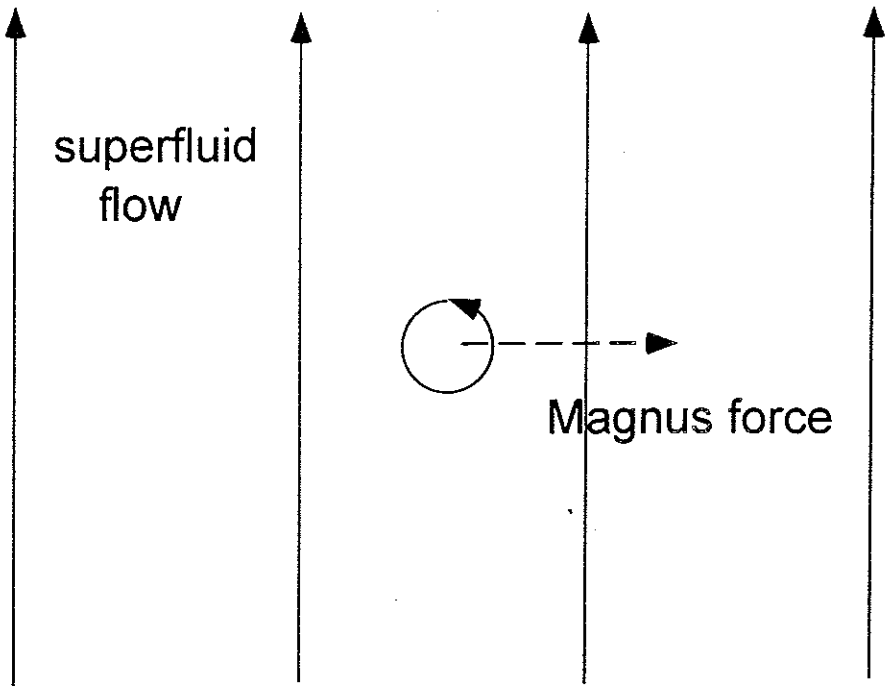

Figure 3-1: Magnus force, $\rho\kappa h\hat{z} \times (v - v_s)$. The z-axis is along the core of the vortex, pointing out of the page.

$$F_p = -f_0 \hat{v}. \qquad 3\text{-}2$$

When the Magnus force exceeds the pinning force, the vortex will slide off the hill. The fluid velocity required for such an event is called the critical velocity, which we can find experimentally by calculating the fluid velocity when the film just begins to swirl. Theoretically, the critical velocity is found by balancing the Magnus force and the pinning force

$$\rho\kappa h v_s = f_0, \qquad 3\text{-}3$$

so

$$v_c = \frac{f_0}{\rho\kappa h}. \qquad 3\text{-}4$$

With the addition of a viscous drag force, the total force on a vortex is

$$F_{net} = \rho\kappa h \hat{z} \times (v - v_s) - f_0 \hat{v} - \gamma \vec{v}. \qquad 3\text{-}5$$

Because the core has no mass, this equation determines the movement of a vortex.

When vortices move, their change in position means that the circulation state of the system has changed. This change can be understood by examining the results of vortex motion on an infinite strip of film. In the film there are two kinds of vortices: positive and negative. They come in equal numbers because they come from a vortex ring that expands as it gains energy until it hits the surface, when it splits into the two opposite vortices (figure 3-2). Given a kinetic drag force to keep the vortices from simply flowing along with the fluid around them, a driven fluid flow will make the vortices move in a direction with a component perpendicular to the flow. The two different kinds of vortices will move opposite directions, which collects positive vortices on one side and negative ones the other. When we turn off the driven flow with all the vortices separated, we can examine the flow between the two rows of vortices from their 1/r fields. Because the vortices circulate in opposite directions,

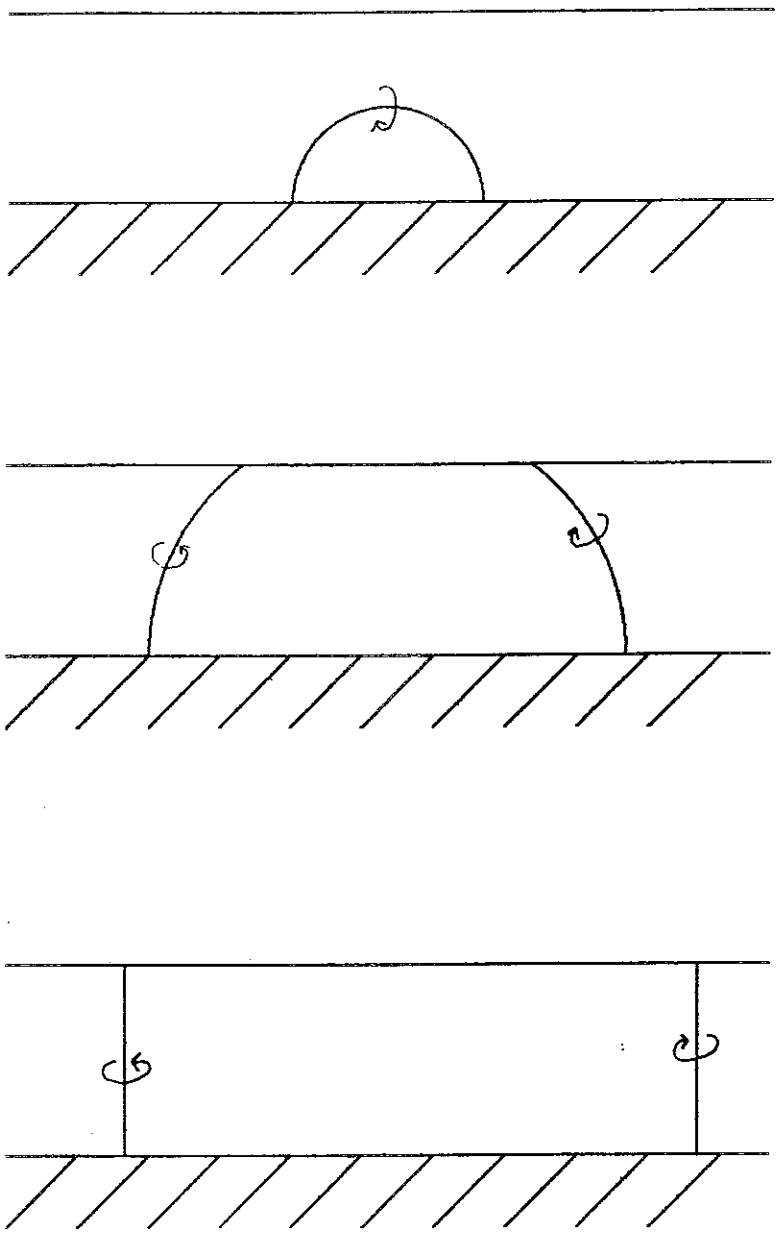

Figure 3-2: Vortex creation. When the film is being cooled through the transition temperature, the turbulence from boiling produces rings, which form two vortices each below T_λ.

their velocity fields add in the middle of the strip, and we can say a flow has been induced.

Our cell can be envisioned as two parallel infinite strips of film attached only at the edges. Given a driven flow that sorts positive vortices to the right and negative ones to the left on the bottom strip, a flow in the same direction on the top strip will sort the vortices in exactly the opposite direction; upside-down vortices circulate the opposite way from their right-side-up comrades. It may seem at this point that at the very edges of the strip there would be a very fast flow that would make the net induced flow on the strip zero, but a negative vortex on the top moves to the same edge as a positive vortex on the bottom and vice versa. When they wrap around the side connection, they annihilate, leaving no backward flow.

This model for vortex sorting can be moved into our cell by bending the two infinite strips and joining them so that one edge forms the boundary to the hole and the other forms the outer radius of the cell. When the vortices are sorted, some may get to the hole or the edge, but many are left sitting in the cell, supporting the flows that are described in Chapter 4.

CHAPTER 4

Programs and Models

SPLIT.BAS

When I entered the lab in 1993, the flow field inside the cell was yet unknown. My first modeling contribution was to write a program that calculated the splittings for the modes given a proposed flow field. By comparing the experimental splittings to the theoretical ones, we hoped to determine the experimental flow field.

To achieve this goal, the program began by integrating Bessel's equation, the components of which we derived from the equations of motion of the superfluid as discussed in Chapter 2:

$$\frac{\partial h}{\partial t} = -\vec{\nabla}\cdot(h\vec{v}) \qquad 2\text{-}2$$

$$\frac{\partial v}{\partial t} = -g\vec{\nabla}h - (\vec{v}\cdot\vec{\nabla})\vec{v} \qquad 2\text{-}3$$

Again, an oscillatory film thickness and velocity were assumed, but this time the velocity has a drift velocity component, v_0.

$$h = h_0 + \eta e^{im\phi}e^{-i\omega t} \qquad 2\text{-}4$$

$$\vec{v} = \hat{\phi}v_o(r) + (\hat{r}v_r(r) + \hat{\phi}v_\phi(r))e^{im\phi}e^{-i\omega t}. \qquad 4\text{-}1$$

The substitution generates the following equations, which when integrated in steps forms a perturbed version of a Bessel function:

$$\frac{\partial \eta}{\partial r} = \left(\omega - \frac{mv_o}{r}\right)v_r + \frac{2v_o}{r}v_\phi \qquad 4\text{-}2$$

$$\frac{\partial v_r}{\partial r} = \left(\omega - \frac{m v_o}{r}\right)\eta + \frac{v_r}{r} - \frac{m}{r} v_\phi \qquad 4\text{-}3$$

$$v_\phi = \frac{m\eta - (v_o + r v_o')v_r}{\omega r - m v_o}. \qquad 4\text{-}4$$

All velocities have been scaled by the third sound velocity so that $v_x \equiv \frac{v_x}{c_3}$,

and η has been scaled by the film thickness so that $\eta \equiv \frac{\eta}{h}$.

From these equations, we can calculate the frequency shifts from the presence of a flow in the cell, and from those, determine splittings for the various modes that we usually measure (figure 4-1). The splittings are found experimentally by

$$\delta = \frac{\Delta\omega}{\omega}, \qquad 4\text{-}5$$

the shift of the mode up or down from the unshifted frequency over the unshifted frequency. Each different flow field plugged into the program produces a different effect on the splittings of each mode. We used velocity fields proportional to 1/r, a constant, and r. Different flow fields have regions of greater flow in different radial locations, so some interact more with the (1,1), where the greatest motion is through the center, and some interact more with higher modes, where most of the action is near the edges of the cell (figure 4-2). A parameter γ_{mn} must be introduced to account for the strengths of the splittings for each of the modes and flow fields.

$$\frac{\Delta\omega}{\omega} = \gamma_{mn} \frac{v_0(a)}{c_3} \qquad 4\text{-}6$$

Here the shift has been explicitly scaled by the third sound speed and the flow at the perimeter of the cell. Previous work has been done to find γ_{mn} using perturbation theory (Appendix C, part 5), and the program confirmed the earlier values (see M_γ,

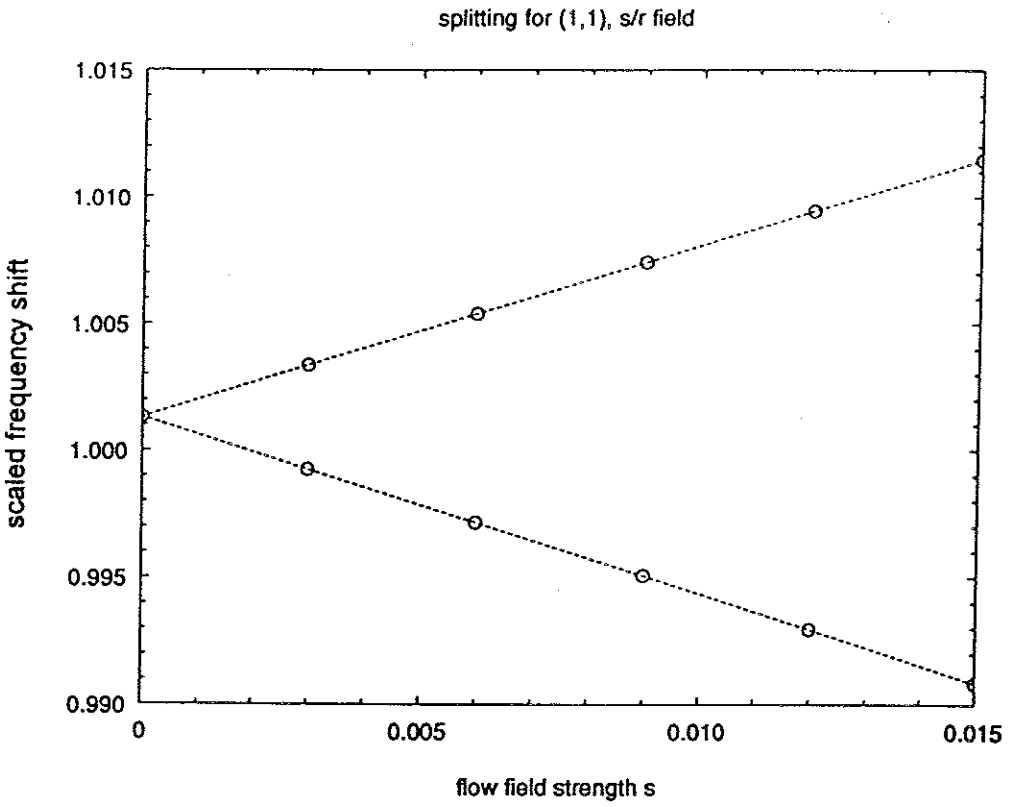

Figure 4-1a: An example of calculated splittings for a 1/r flow field as a function of strength s. This is the flow field that would result from having all the vortices in the center, with s proportional to the number of vortices. Splittings of all modes increase linearly.

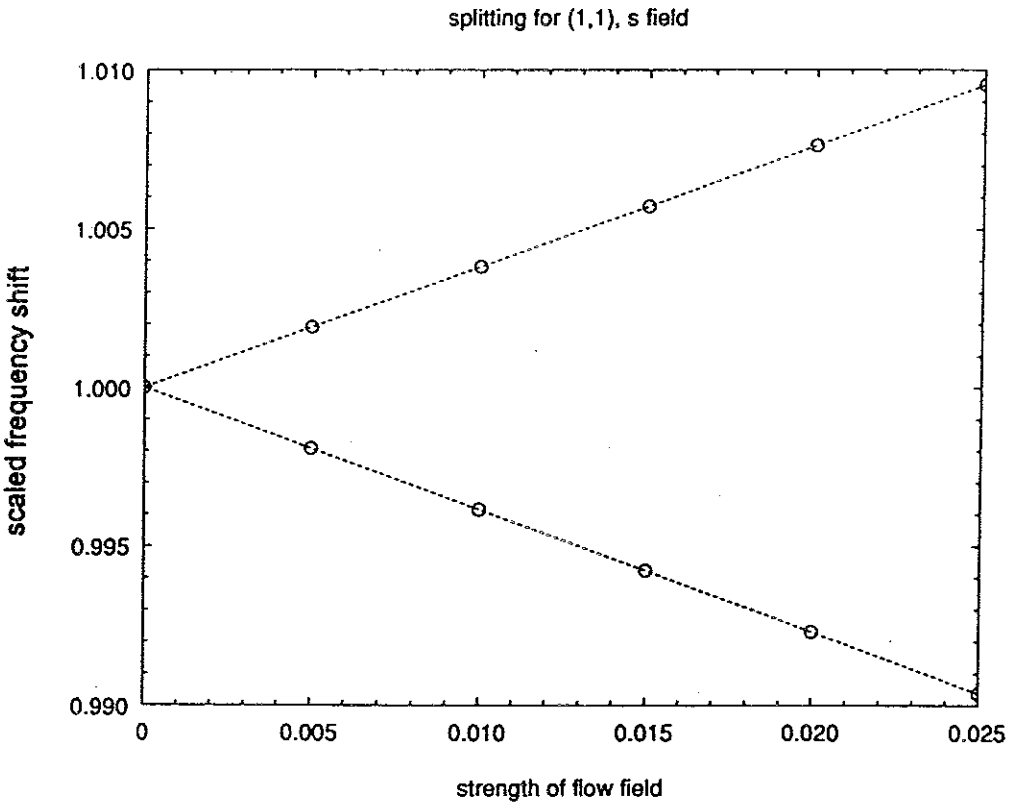

Figure 4-1b: An example of calculated splittings for a constant flow field as a function of strength s. This field would result from having a 1/r distribution of vortices. All splittings are linear.

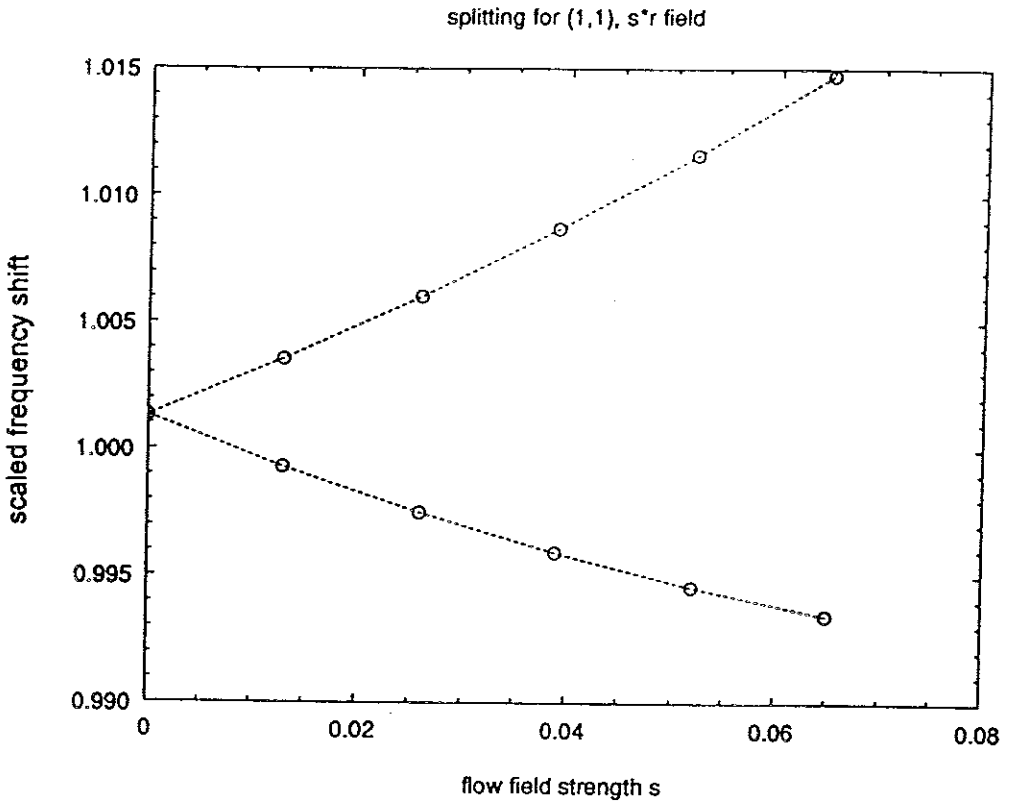

Figure 4-1c: An example of calculated splittings for a flow field proportional to r as a function of strength s. This solid body rotation of the fluid would require a constant distribution of vortices. Although the shifts about the unswirled resonance are not symmetric on the graph for the (1,1) (the lines are curved), the splittings still increase linearly for all three modes.

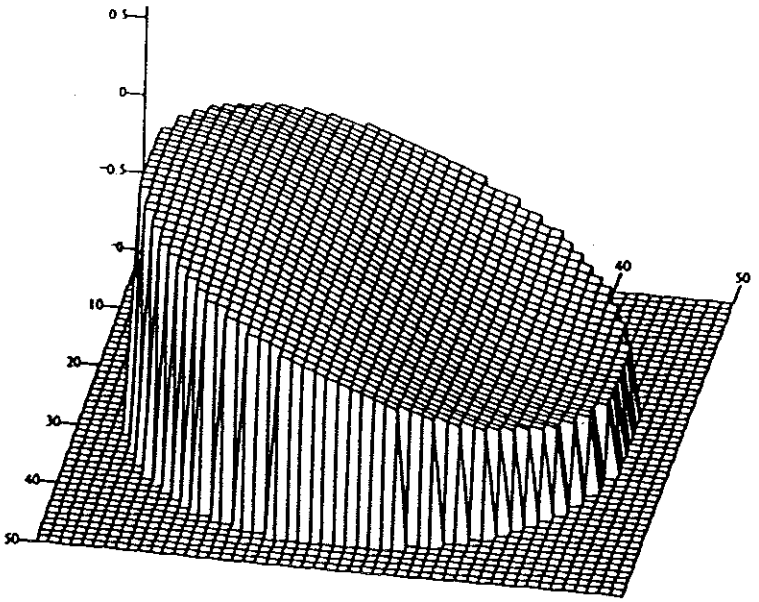

Figure 4-2: The (1,1) and (11,1) modes. Fluid motion for the (1,1) mode is through the center of the cell, while motion for the (11,1) is predominantly around the edges. The splittings of the two modes are sensitive to fluid flow in different locations, and by using the splittings of several modes we can accurately map fluid flow as a function of radius of the cell.

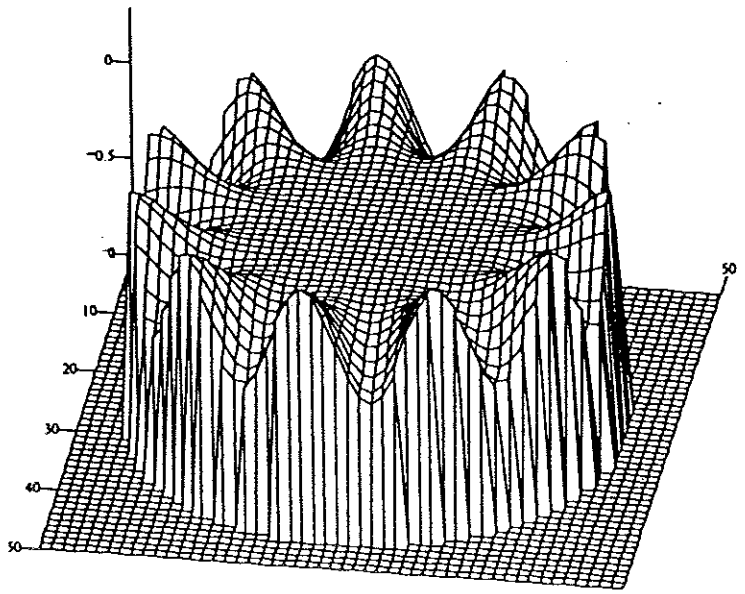

below, Baierlein, private communication). Also the program results verified that the splittings were linear as a function of the strengths of the chosen fields.

Given the ability to produce theoretical splittings, we can use the results of a combination of those to match experimental splittings and find the flow field in our cell (figure 4-3a). The experimental flow field can be written using the three previously mentioned flow fields as a basis set,

$$v(r) = c_3\left(c_0\frac{a}{r} + c_1 + c_2\frac{r}{a}\right), \qquad 4\text{-}7$$

where c_3 is the third sound speed and the other c coefficients are weighting factors. The experimental splittings, here denoted by δ_1, δ_2, and δ_3, can be used to calculate c_0, c_1, and c_2.

$$\begin{pmatrix}\delta_1\\ \delta_2\\ \delta_3\end{pmatrix} = M_\gamma\begin{pmatrix}c_0\\ c_1\\ c_2\end{pmatrix}, \qquad 4\text{-}8$$

where $M_\gamma = \begin{pmatrix}1.27 & .153 & .089\\ 1.17 & .630 & .409\\ 1.13 & .755 & .549\end{pmatrix}$ (columns = 1/r, 1, and r; rows = (1,1), (2,1), and (3,1)).

The resultant combination of theoretical flow fields reveals that while most of the vorticity is trapped in the hole in the center of the cell, vortices are distributed all over the cell. Figure 4-3b shows a representative sample of v(r) and n(r) results. Because the hole was ground in the glass slides, it was expected that vortices would be trapped on the rough surface there, but because the vortices are all over the cell, we postulated the pinning model discussed in Chapter 3.

The vortex distribution and total number of vortices in the cell can be calculated from

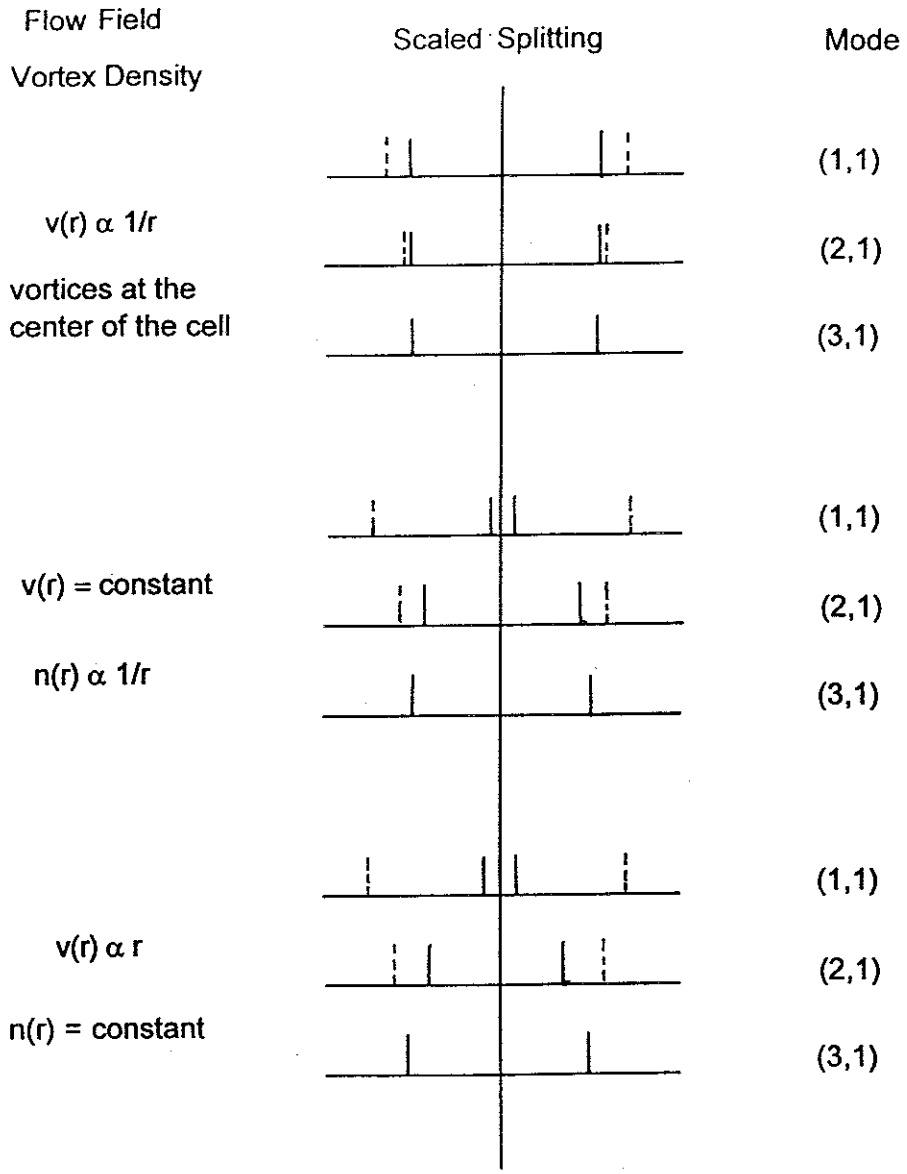

Figure 4-3a: Representations of the scaled splittings for pure flow fields. The dotted splittings are an example of experimental splittings. Experimental splittings are matched using a linear combination of the pure flow fields.

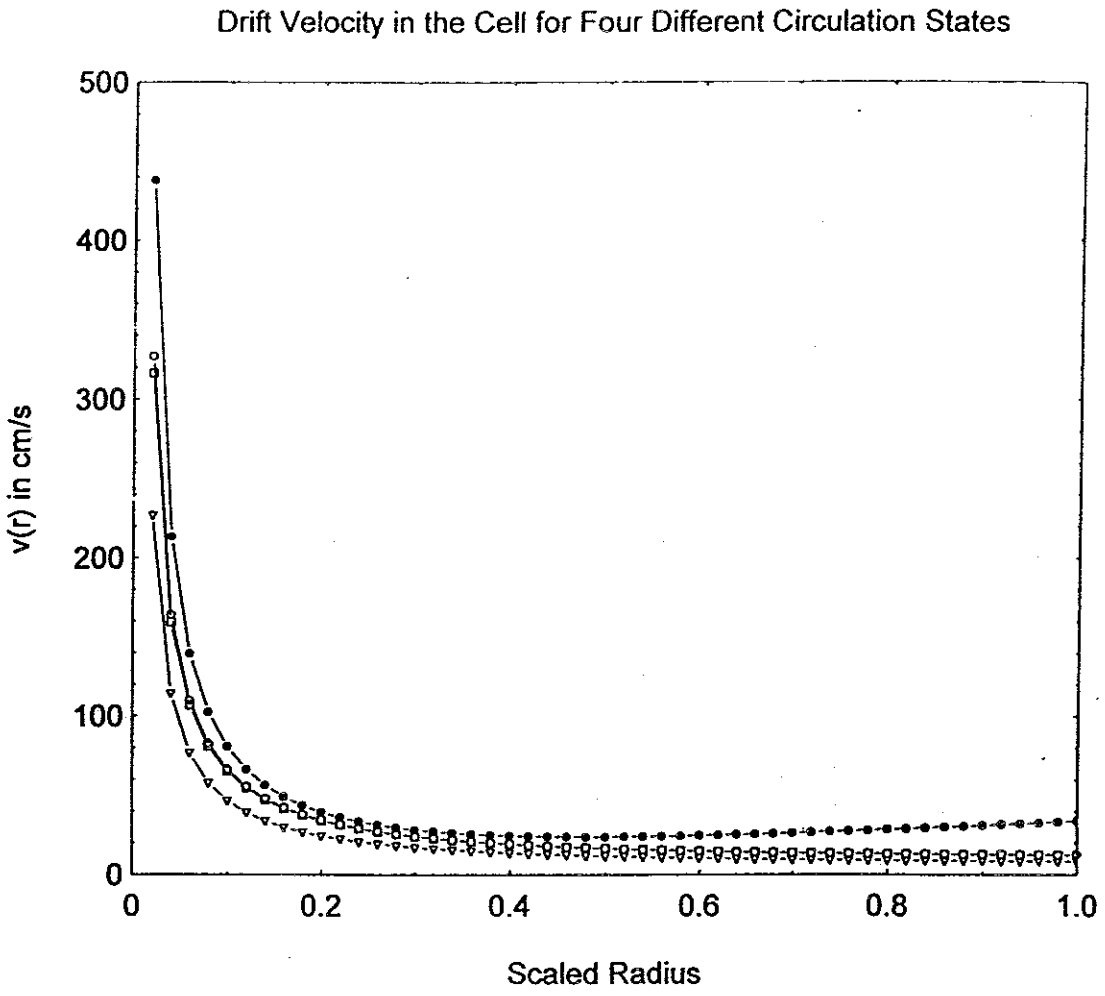

Figure 4-3b: Examples of experimental flow fields and the vortex densities that support them. The different curves each represent a different field.

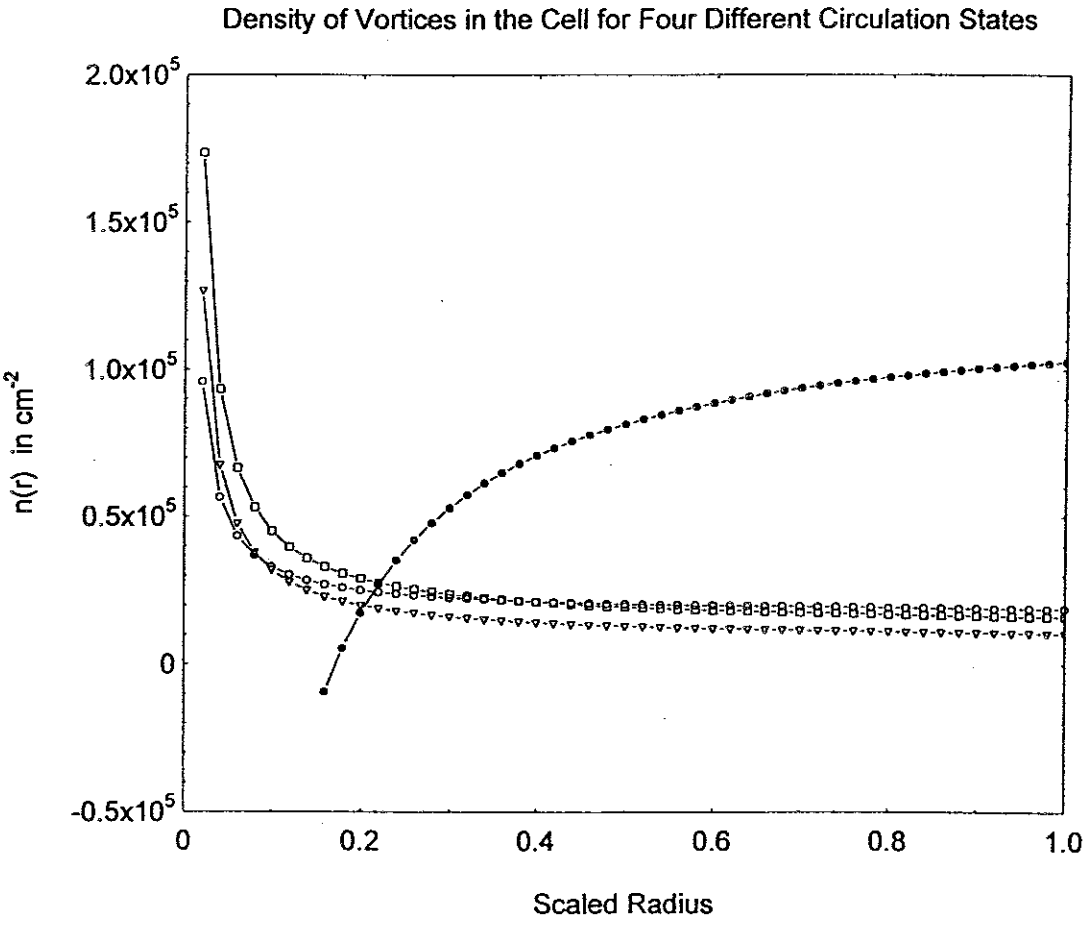
Density of Vortices in the Cell for Four Different Circulation States
2.0x10^5
1.5x10^5
1.0x10^5
0.5x10^5
0
-0.5x10^5
n(r) in cm^-2
0
0.2
0.4
0.6
0.8
1.0
Scaled Radius

the flow field. We begin with the velocity based on a general vortex distribution; some number N_o vortices are trapped in the hole, and a distribution n(r) are in the cell.

$$v(r) = \frac{\hbar}{m_4 r}\left[N_0 + \int_0^r n(r) 2\pi r dr \right] \qquad 4\text{-}9$$

By taking the derivative of both sides we can write n(r) in terms of v(r).

$$n(r) = \left[\frac{\partial v(r)}{\partial r} + \frac{v(r)}{r} \right] \frac{m_4}{2\pi\hbar} \qquad 4\text{-}10$$

This information is the last that we could glean from splitting data. The biggest remaining question was how the vortices arrived at their positions.

FLOWFLD.BAS

The next step on the road to understanding vortices was to use the model of a third sound wave interacting with vortices to calculate a flow field to compare to the measured fields generated by the high amplitude waves. In order to determine what a vortex would do in the cell, we needed to examine the fluid flow there. The flow was not simply a DC current, but an oscillatory flow that interacted with the vortices to create a DC component. The argument leading to the flow under the wave is most easily understood if it is started with a plane wave instead of a circular wave. The film thickness oscillation is sinusoidal

$$\eta = \eta_0 \cos(kx - \omega t). \qquad 4\text{-}11$$

By substituting the amplitude into the one dimensional continuity equation, we can find the velocity:

$$\frac{\partial h}{\partial t} = -h \frac{\partial v}{\partial x} \qquad 4\text{-}12$$

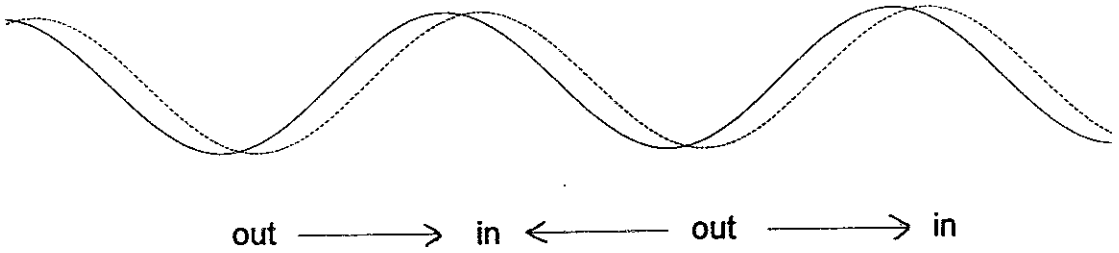

Figure 4-4: Fluid motion under a traveling wave. To move the wave to the right (solid line to dotted line), fluid must flow out from under the old peaks to lower them and under the old troughs to raise them. Accordingly, fluid must flow in under the new peaks and away from the new troughs. Logically, fluid under the peaks flows forward and under the troughs flows backward.

$$v = c\frac{\eta}{h}\cos(kx - \omega t)\,. \qquad 4\text{-}13$$

The velocity and the wave amplitude are both cosines because the time derivative of the thickness oscillation is integrated over x to get the velocity.

Direct comparison of the wave and fluid velocity shows that the velocity of the fluid under the wave is positive under the peaks and negative under the troughs. This unintuitive fact can be explained by examining the position of the wave in the next instant. The peaks and troughs will have moved to the right for a standard traveling wave, and the fluid must flow out of the regions where the new troughs will appear and into those under the new peaks. The fluid flowing forward under the old peak and backward under the old trough accomplishes this motion (figure 4-4). Vortex motion induced under these waves is symmetric. Every motion under a peak or trough is countered under the next trough or peak.

There is a net drift of the wave media; more fluid is moving forward under the peaks than is moving backward under the troughs because of the variations in the film volume under the wave. If the assumption is made that there should be a constant flow rate at all points under the wave in our cell, the waves must be non-linear, which is key to this model of vortex motion. The wave shape is chosen by setting the flow rates, vh, under the peaks and troughs equal. Using the overall film thickness in the following form:

$$h = h_0 + \eta\cos(kx - \omega t)\,, \qquad 4\text{-}14$$

the nonlinear velocity can be found by dividing the linear velocity by the dynamic film thickness

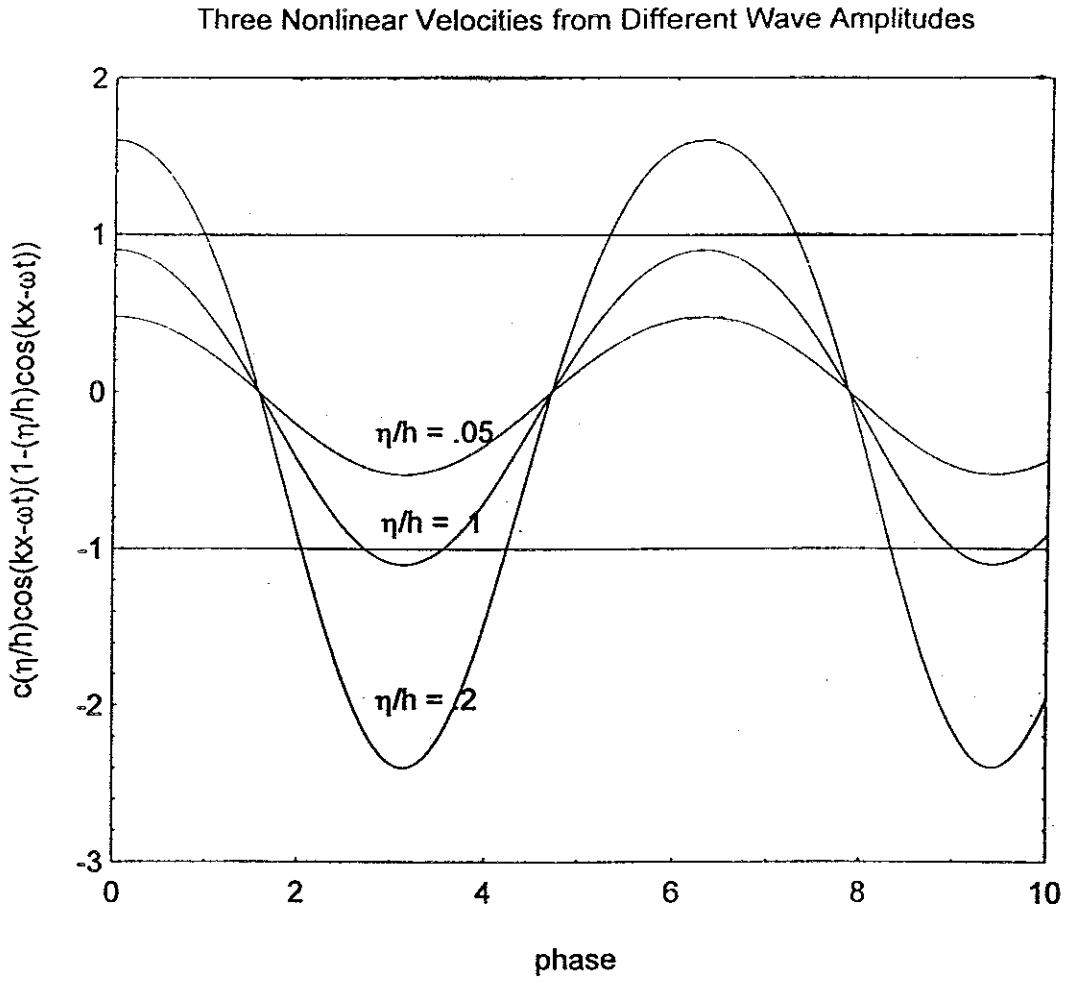

Figure 4-5: Scaled non-linear waves. The third sound speed in this example is ten times larger than the critical velocity. The critical velocity is marked on the graph at ±1. See figure 4-6 for experimental critical velocities.

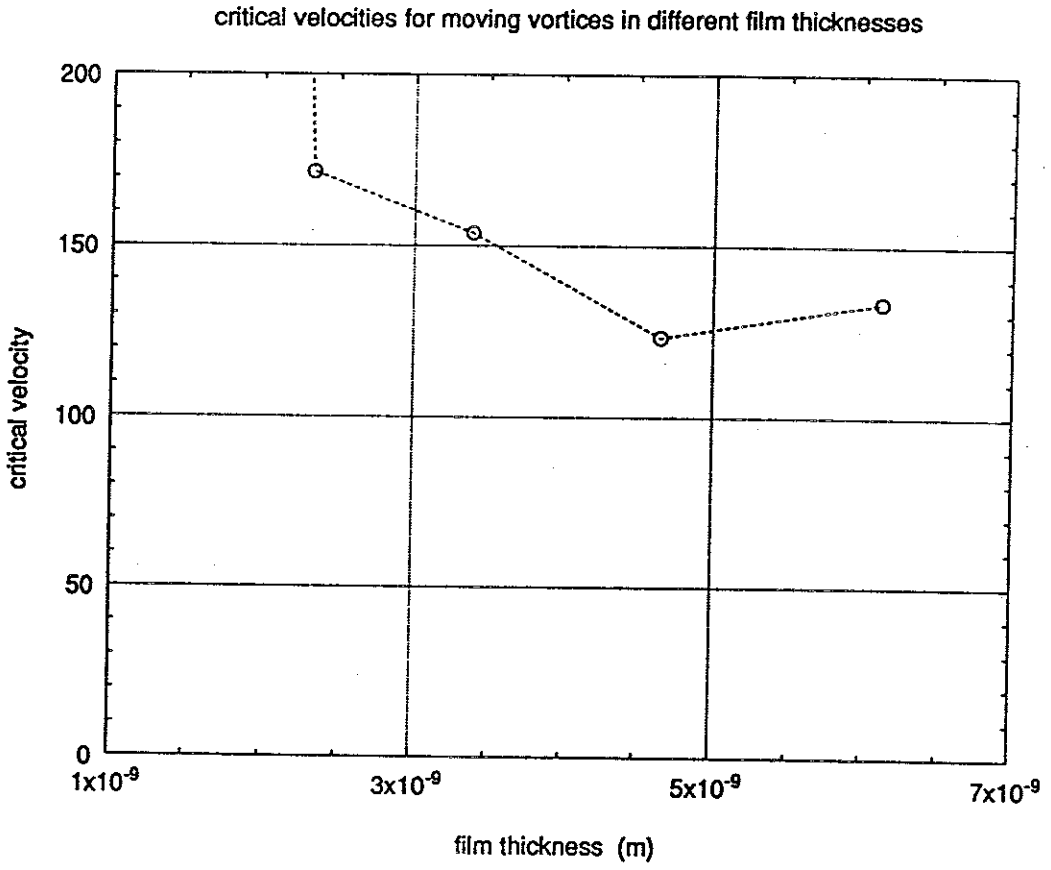

Figure 4-6a: Some sample critical velocities.

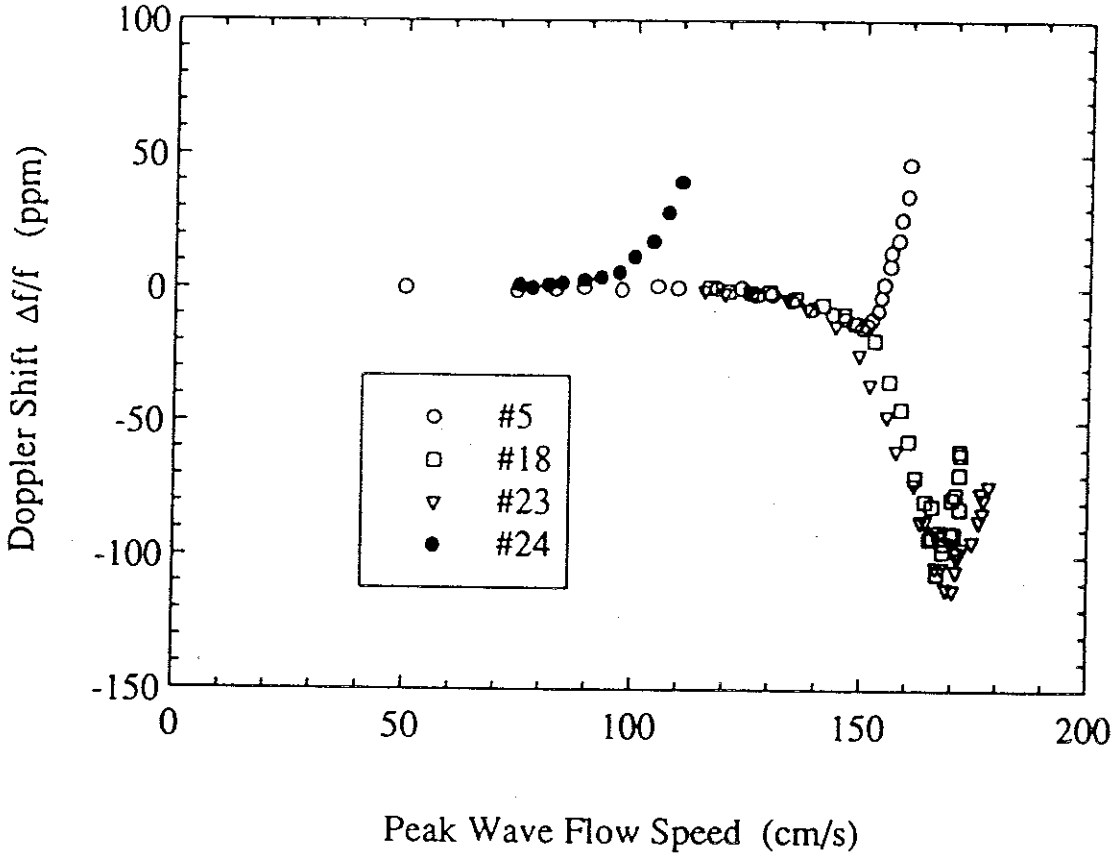

Figure 4-6b: Relative frequency change of the (1,1) mode for increasing maximum flow speed under the wave. The curves continue to rise at the end if the peak flow speed is increased further, but these curves are used to determine critical velocities. Note that the mode sometimes shifts down before its rise.

$$v_{nonlin} = \frac{c\frac{\eta}{h_0}\cos(kx-\omega t)}{1+\frac{\eta}{h_0}\cos(kx-\omega t)}. \qquad 4\text{-}15$$

Expanding,

$$v_{nonlin} = c\frac{\eta}{h_0}\left(1-\frac{\eta}{h_0}\cos(kx-\omega t)\right)\cos(kx-\omega t) \qquad 4\text{-}16$$

(figure 4-5). Henceforth we will neglect the subscripts and refer to h_0 as h. The asymmetric flow can, with a high enough amplitude, produce a net vortex drift.

With the non-linear wave, the fluid velocity may exceed the critical velocity under the troughs or under both the peaks and the troughs of the wave and move vortices. At small wave amplitudes, the critical velocity will never be exceeded. The waves will be essentially linear, but the reason that vortices will not move under them is that the fluid velocity is too small to move vortices off of their pinning sites. As $\frac{\eta}{h}$ increases, the waves become more nonlinear. Because the wave is deeper at the troughs and shallower at the peaks, the trough velocity will exceed the critical velocity first. Then vortex motion occurs in one direction only, according to the fluid flow under the troughs. The vortices stop moving when the induced drift velocity works against the trough velocity and the result no longer exceeds the critical velocity. The drift velocity adds to the oscillating velocity field, shifting it up by a constant until the critical velocity is no longer reached at any point under the wave. Vortex motion stops in this new configuration, and we say that the film has been swirled.

The last possible case, where the critical velocity is exceeded under both the troughs and the peaks, comes to a net drift argument. The vortices move one way under the

troughs and the other under the peaks. The motion under the peaks and troughs must exactly cancel in equilibrium. The locations of the vortices vary over a full wave cycle, but their average positions determine the drift velocity in the cell.

The program FLOWFLD steps along the radius of the cell and calculates v_{nonlin} given an experimental third sound speed, mode, and amplitude. The wave velocity is given in components by

$$v_r = \frac{c\frac{\eta}{h}}{1+\frac{\eta}{h}J_m(kr)\cos(m\phi-\omega t)}\left(\frac{m}{kr}J_m(kr)-J_{m+1}(kr)\right)\sin(m\phi-\omega t) \qquad 4\text{-}17$$

and

$$v_\phi = \frac{mc\frac{\eta}{h}}{1+\frac{\eta}{h}J_m(kr)\cos(m\phi-\omega t)}\frac{J_m(kr)}{kr}\cos(m\phi-\omega t). \qquad 4\text{-}18$$

If the vector sum of these velocities at the specified radius exceeds the critical velocity, then the response of the vortex is determined by a complicated formula in Appendix D. The program integrates the velocity of the vortex over a cycle of the wave and determines whether there has been a net change in the radial position of the vortex. To save steps, the program does not keep track of azimuthal position changes because they do not affect the circulation state of the film. If there has been a shift, the program adds a drift velocity, $v_d(r)$, to v_ϕ and integrates again. When there is no net drift during the cycle, the program moves on to the next radial position and repeats the steps to find the next $v_d(r)$.

The graphs of v_d vs. r (figures 4-7 and 4-8) generated by the program have some odd

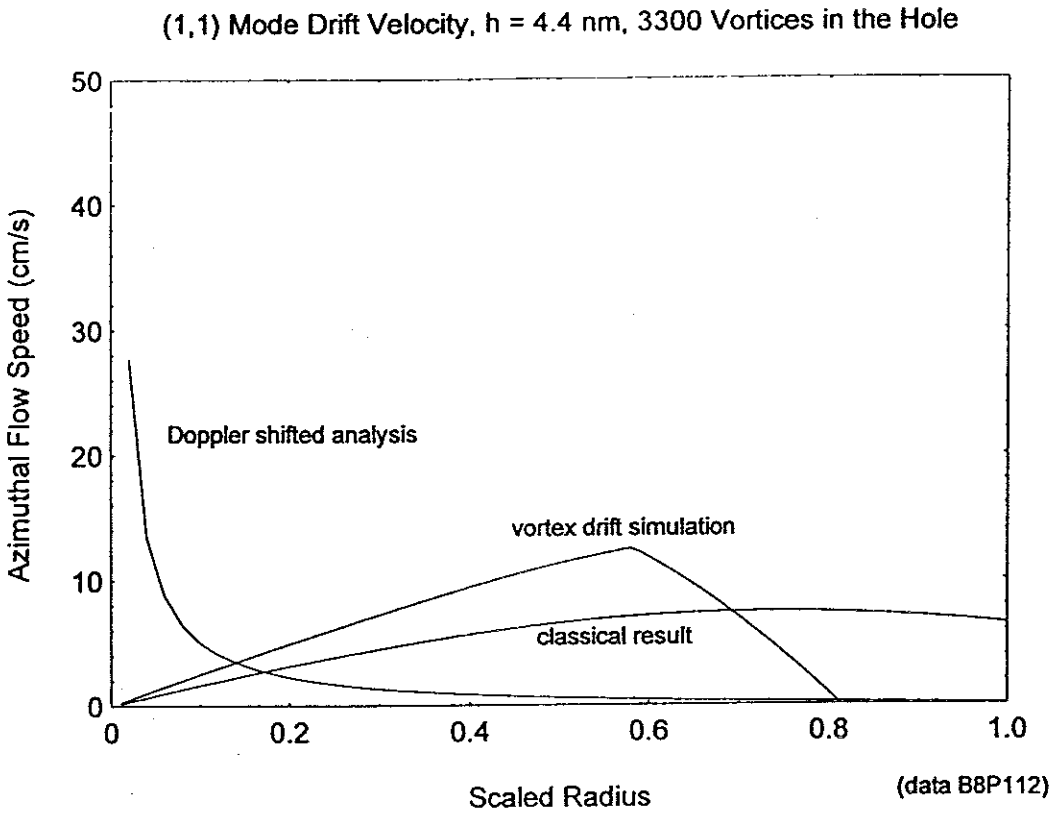

Figure 4-7: Drift velocity (azimuthal flow)as a function of radius. Examples of an experimental flow field (Doppler shifted analysis), the predicted flow field from the programs using experimental parameters (vortex drift simulation), and a predicted field for a classical fluid using the same parameters. The (1,1) mode was difficult to swirl at this film thickness, so the experimental flow field for it is small. The experimental fields for the (2,1) and (3,1) are much larger because they were easy to swirl, but the predicted fields clearly fail to generate any circulation close to the hole.

(2,1) Mode Drift Velocity, h=4.4 nm, 27000 Vortices in the Hole

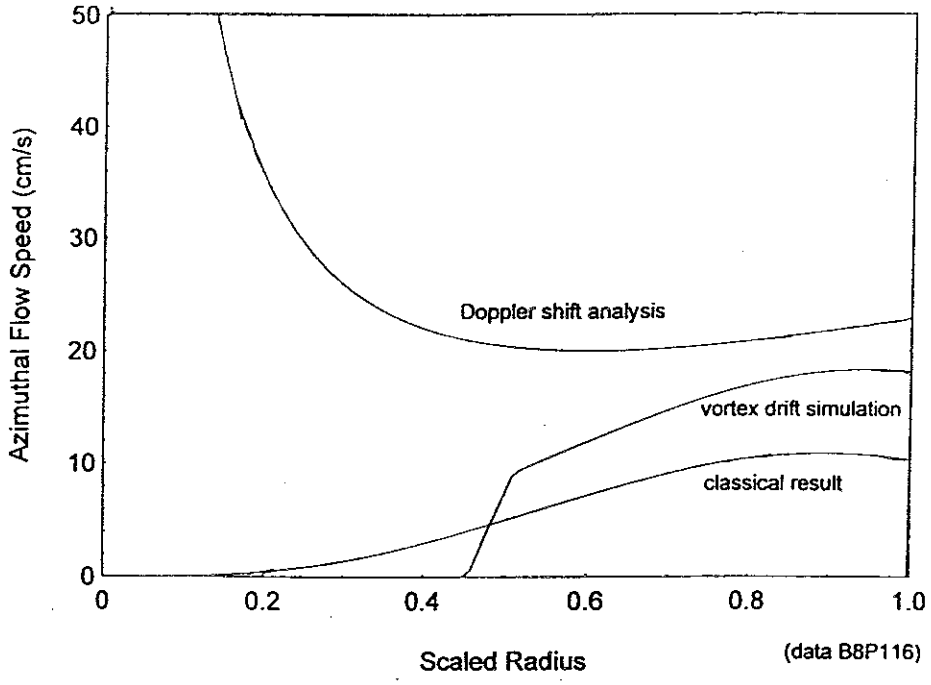

(3,1) Mode Drift Velocity, h=4.4 nm, 41000 Vortices in the Hole

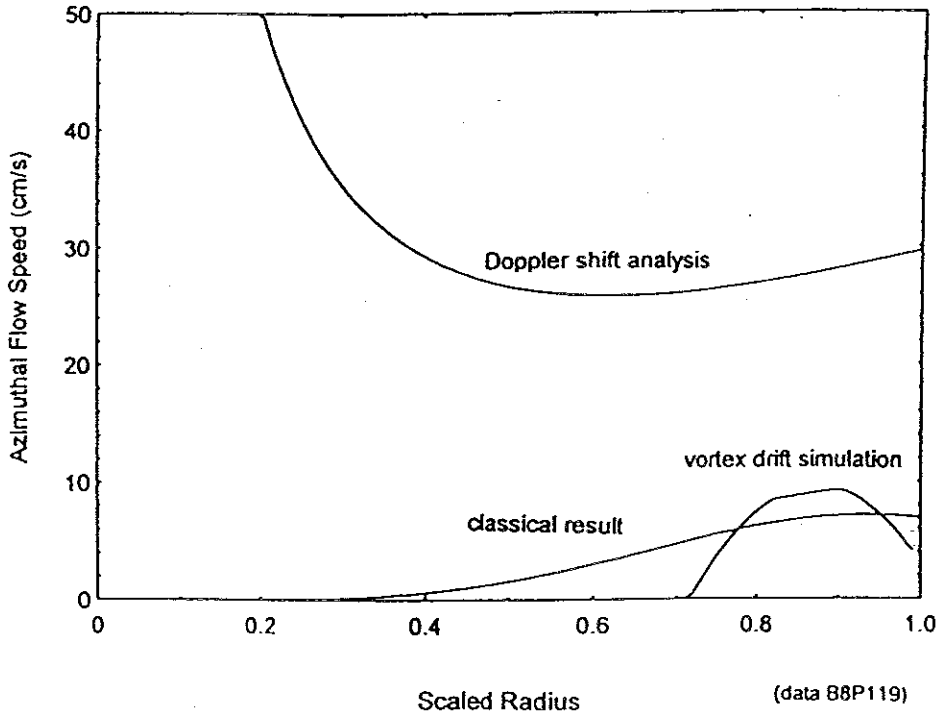

features that occur in different realms of vortex motion. The easiest feature to explain is the sections of the curves where $v_d = 0$. If the wave is too small at some radius in the cell, the critical velocity will not be reached there, and no circulation will be induced. As the number of radial nodes increases, the motion of the film is increasingly concentrated near the edges of the cell, and thus there can be large parts near the center of the cell with no flow. Even for the (1,1) mode, most of the motion occurs away from the center because the wave is rotating and not standing.

At radii where the trough velocity exceeds the critical velocity, a smooth increase in drift velocity arises as r increases. The rise occurs because the amplitude of the wave varies over the radius of the cell. The region where only the troughs can move vortices spans a range of trough amplitudes that increase with increasing r. As the wave amplitude gets larger, the peak velocity may begin to move vortices. If the peak velocity never reaches v_{crit} under the peaks, then the curve continues smoothly until it reaches either the edge of the high velocity region or the edge of the cell. If the amplitude is large enough that vortices move under the peaks, a kink appears in the curve as v_d levels off. The kink occurs again toward the outer edge of the cell when the peak velocity drops below v_{crit} again.

Comparison of the model to the actual flow field determined that our model was imperfect (figure 4-7). We have since learned that nonlinear waves are not necessary for flow to be induced, and indeed, the model failed to predict the concentration of vortices in the center of our cell. However, it is still interesting to compare our model to the classical drift velocity (figure 4-8):

$$\frac{1}{h}\langle (h+\eta)\bar{v}\rangle_t = \frac{1}{2}c_3\left(\frac{\eta}{h}\right)^2 \frac{m}{kr}\left(J_m(kr)\right)^2 \qquad 4\text{-}19$$

[Ellis, 1997]. In Appendix E we will use this model again in an effort to model the

swirling process.

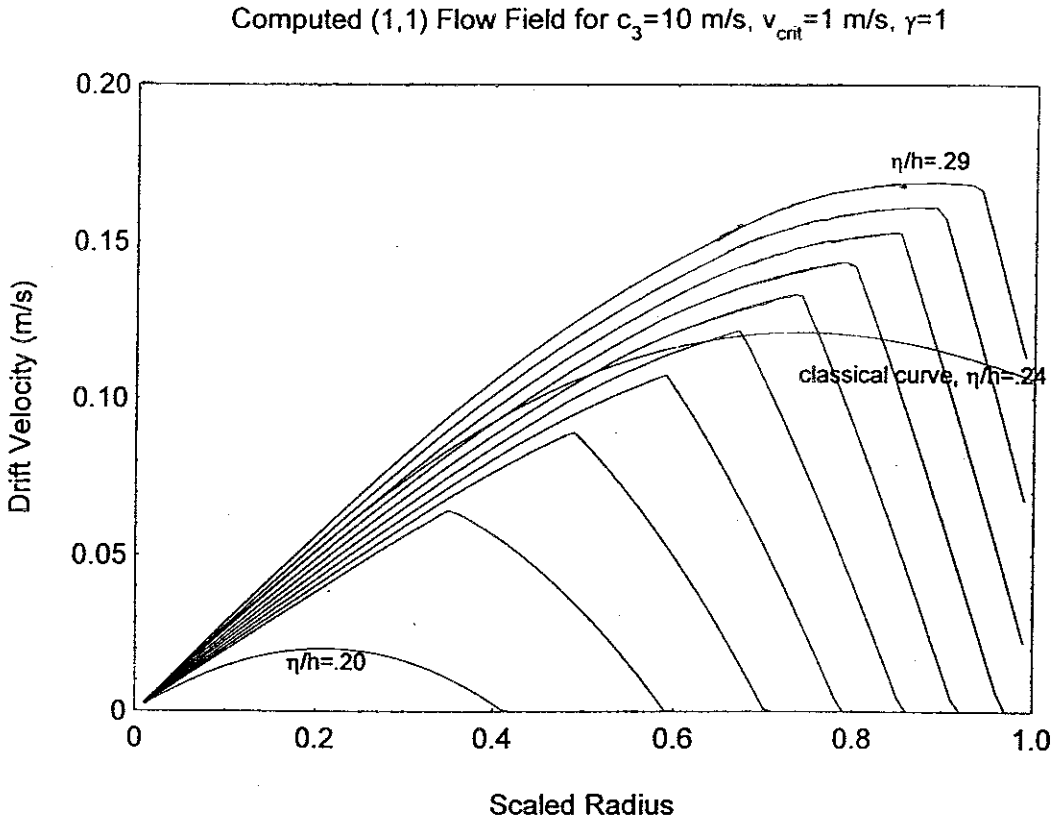

Figure 4-8: Examples of predicted flow fields for different film thicknesses and γ (g) values and classically predicted fields.

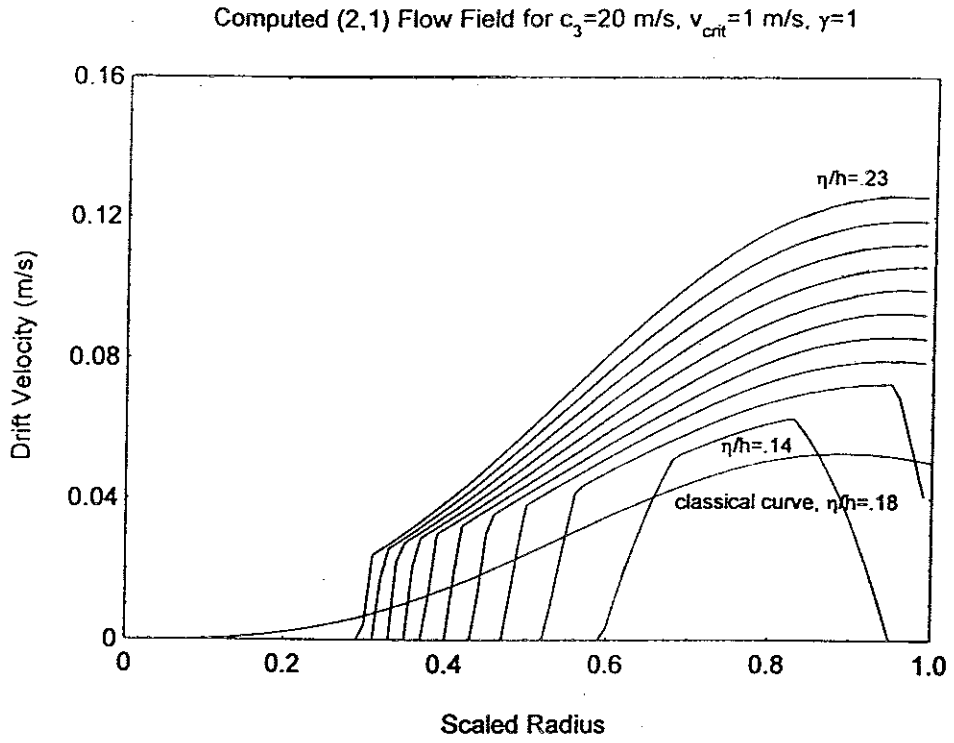
Computed (2,1) Flow Field for c_3=20 m/s, v_{crit}=1 m/s, γ=1
Drift Velocity (m/s)
0.16
0.12
0.08
0.04
0
η/h=.23
η/h=.14
classical curve, η/h=.18
0
0.2
0.4
0.6
0.8
1.0
Scaled Radius

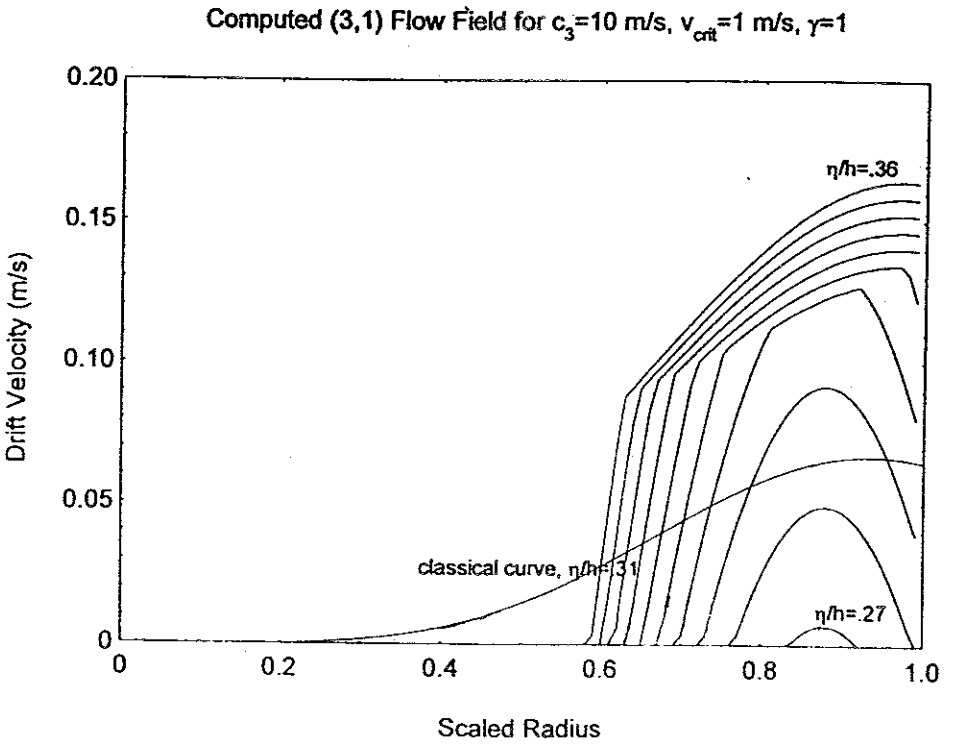
Computed (3,1) Flow Field for c_3=10 m/s, v_{crit}=1 m/s, γ=1
Drift Velocity (m/s)
0.20
0.15
0.10
0.05
0
η/h=.36
classical curve, η/h=.31
η/h=.27
0
0.2
0.4
0.6
0.8
1.0
Scaled Radius

CHAPTER 5

Effects of High Amplitude Waves

When we first added the transformer that allowed us to swirl the film, we only worked with the (1,1) mode because higher modes logically would either not couple to a rotational drive or the mode overlap would be small enough that swirling would seem unlikely. It was found that a high amplitude scan down through the upper branch of the (1,1) [the (1,1)+] could increase the circulation. The shape of the resonance during such a scan was smeared downward, so that the amplitude "crashed" down off the peak. The amplitude at the crash point was much larger than the maximum amplitude that could be achieved on resonance. When approached from below, the amplitude popped up and coasted down, but hysteretically—the pop was higher in frequency and closer to the resonance than the crash (figure 5-1). It also failed to swirl the film. Similarly, the splitting (circulation) could be decreased with a down crash through the lower branch of the (1,1) [the (1,1)-].

The shape of the resonances can be explained by modeling our system as a driven, damped harmonic oscillator with a nonlinear restoring force.

$$m\ddot{x} = -kx + \frac{k}{\lambda^2}x^3 - \gamma\dot{x} + f_0 \cos\omega t \qquad 5\text{-}1$$

Here we must assume a solution for x that includes a cubic (following Baierlein, 1983)

$$x = c_1 \cos\omega t + c_2 \cos 3\omega t + \ldots \qquad 5\text{-}2$$

When x is substituted back into the previous equation and the assumption that $c_1 >> c_3$ is made, the coefficients of the powers of e can be isolated and set to zero. These machinations yield c_1 and c_3 (approximately, but well enough), and the solution

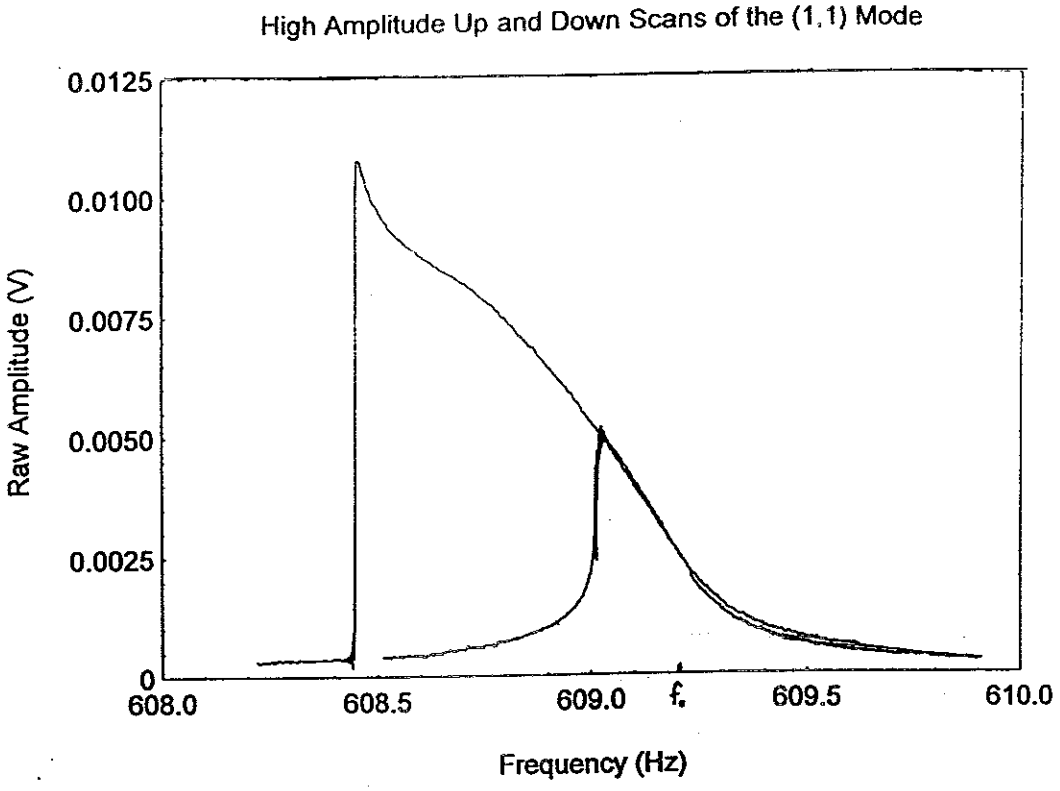

Figure 5-1a: Scans from above and below a (1,1) resonance. The hysteretic effect is clearly visible.

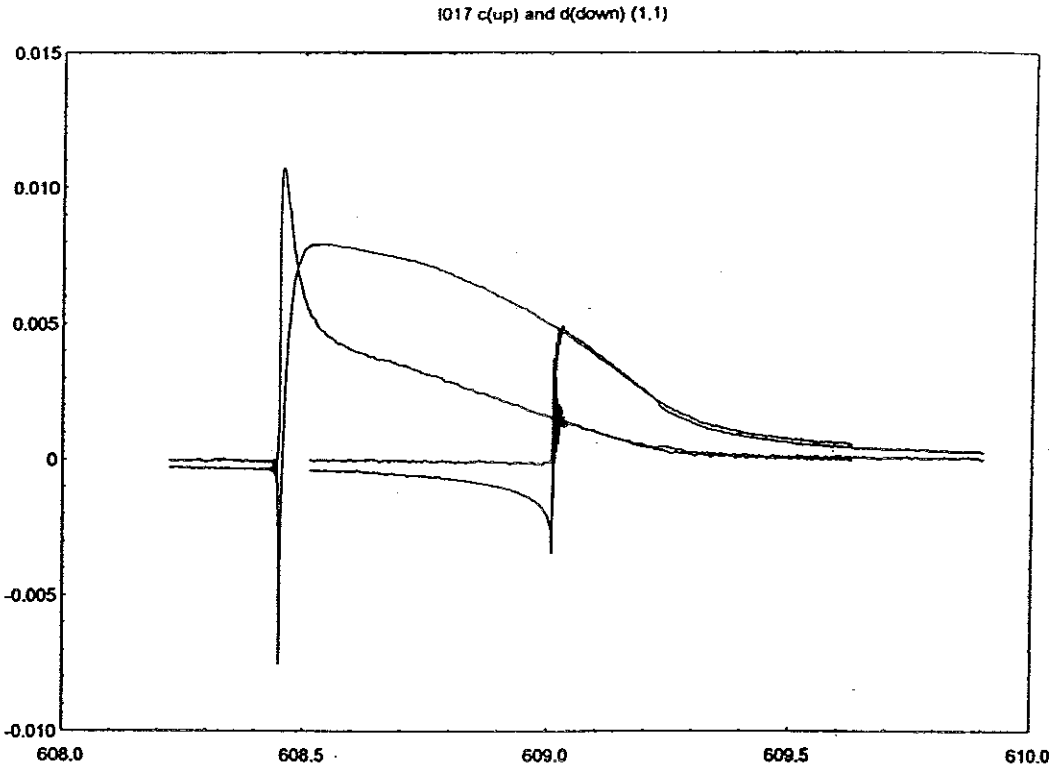

Figure 5-1b: The same scans shown as the real and imaginary parts of the amplitude vs. frequency.

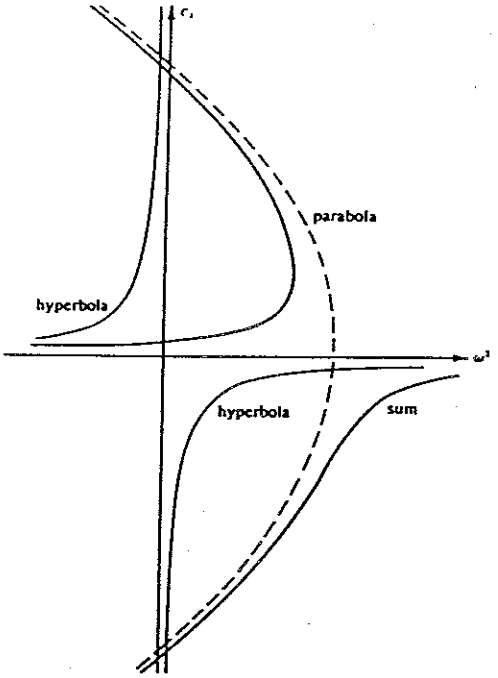

Figure 5-2: The sum of the parabola and the hyperbola (after Baierlein, 1983) yields a non-Lorentzian shape with a hysteretical effect. Approaching this resonance from above, the amplitude follows the top of the curve until it reaches point b, where it abruptly crashes to zero. In the reverse direction, the amplitude precipitously leaps to the upper curve at point a.

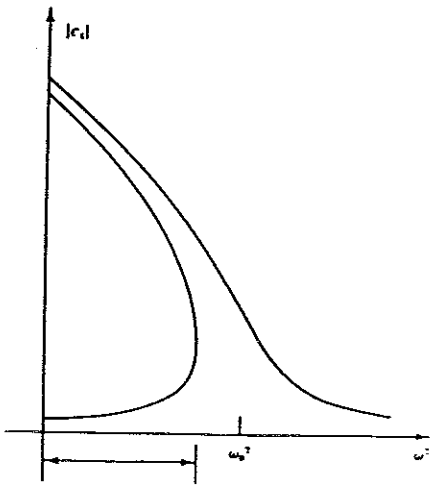

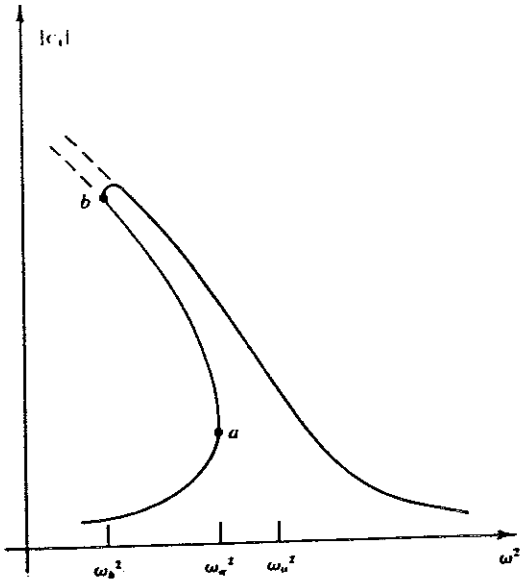

Figure 5-3: As amplitude increases, the effects of the non-linear restoring force become more noticeable (after Baierlein, 1983).

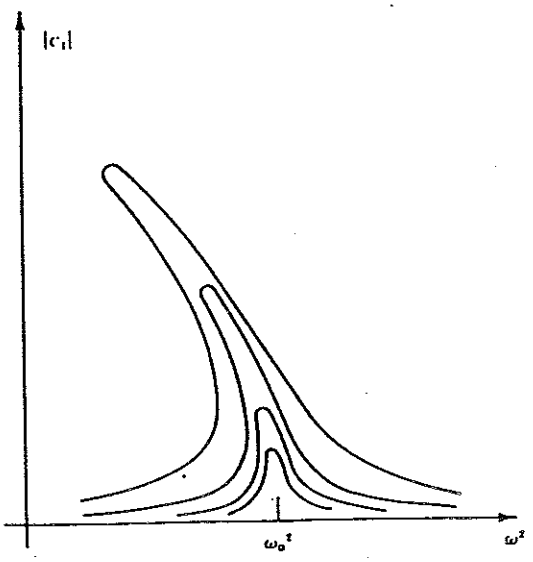

for c_1 is a triple valued function that is a combination of a parabola and a hyperbola approximately the same shape as our experimental curves (figures 5-2 and 5-3).

To further investigate the mechanics of the swirling process, a program, FChart, was created to move the peaks along. It works by following a specific point on the resonance as determined by the phase. The operator of the program finds the amplitude and phase where the resonance begins to move. When the drive frequency has been set manually as close as possible to the crash point but not actually crashing, the program is started. The program then attempts to stay at that phase on the resonance even as it moves, and to do that, it must increase the drive frequency. The (1,1) typically moves at about 0.1 Hz/hour.

A different program, SurfDat, steps the frequency across the resonance, and the data plotted as the real and imaginary parts shows clearly where the peak starts to swirl. When the peak moves, the origin of the circle moves, and the circle is distorted (figure 5-4). The points in the distorted part of the curve can be matched to those on amplitude vs. frequency plots where the curve turns up right before the crash (figure 5-5). The amplitude of the moving peak increases quickly before the crash because the frequency step is effectively larger.

During the summer of '95 we attempted to swirl the (2,1). We thought it might be possible because we had seen some odd behavior (the (2,1) "funnies") there before (figure 5-6). We noticed that a high amplitude scan up through the (2,1)+ would drag the peak up, and our first assumption was that this behavior was because of a non-linear restoring force with the opposite sign to that of the (1,1).

Plots of the real and imaginary parts of the amplitude reveal that the peaks are still

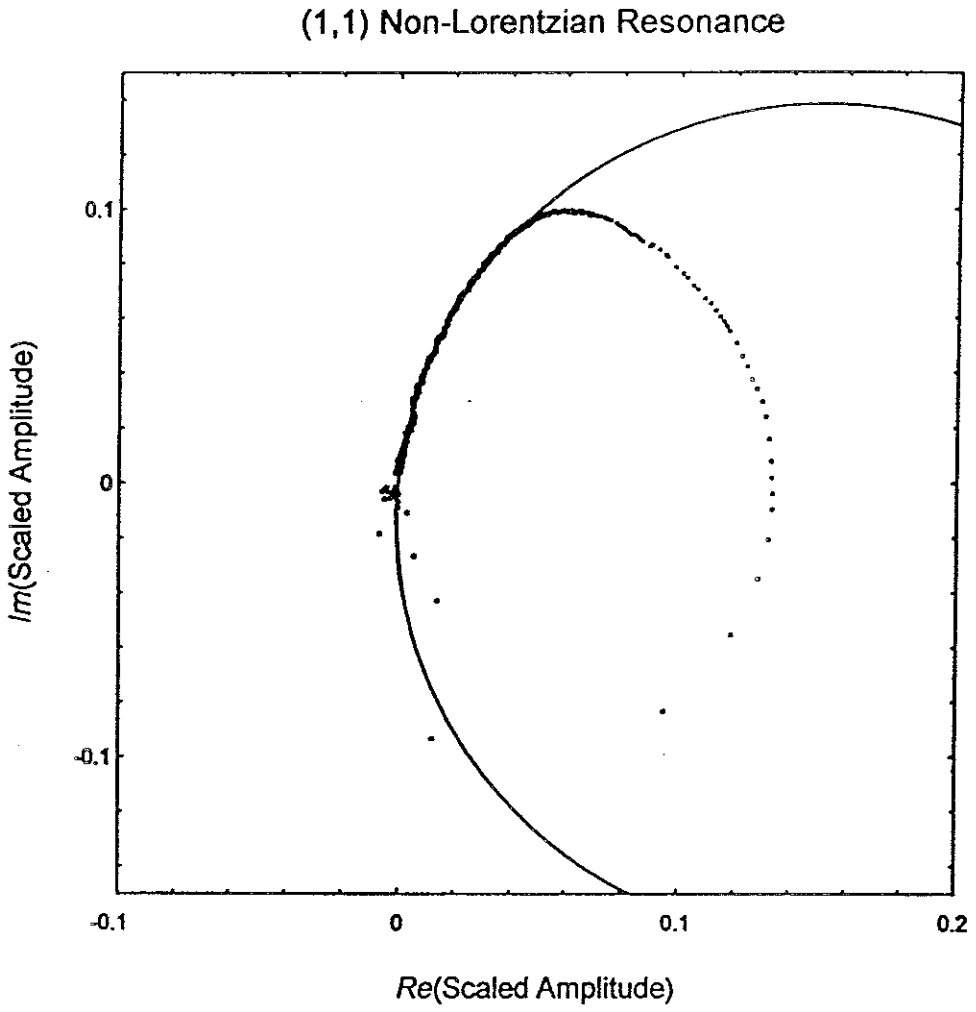

Figure 5-4: This swirling scan of the (1,1) clearly shows its non-linear behavior. The circle is a suggested fit to the beginning of the scan.

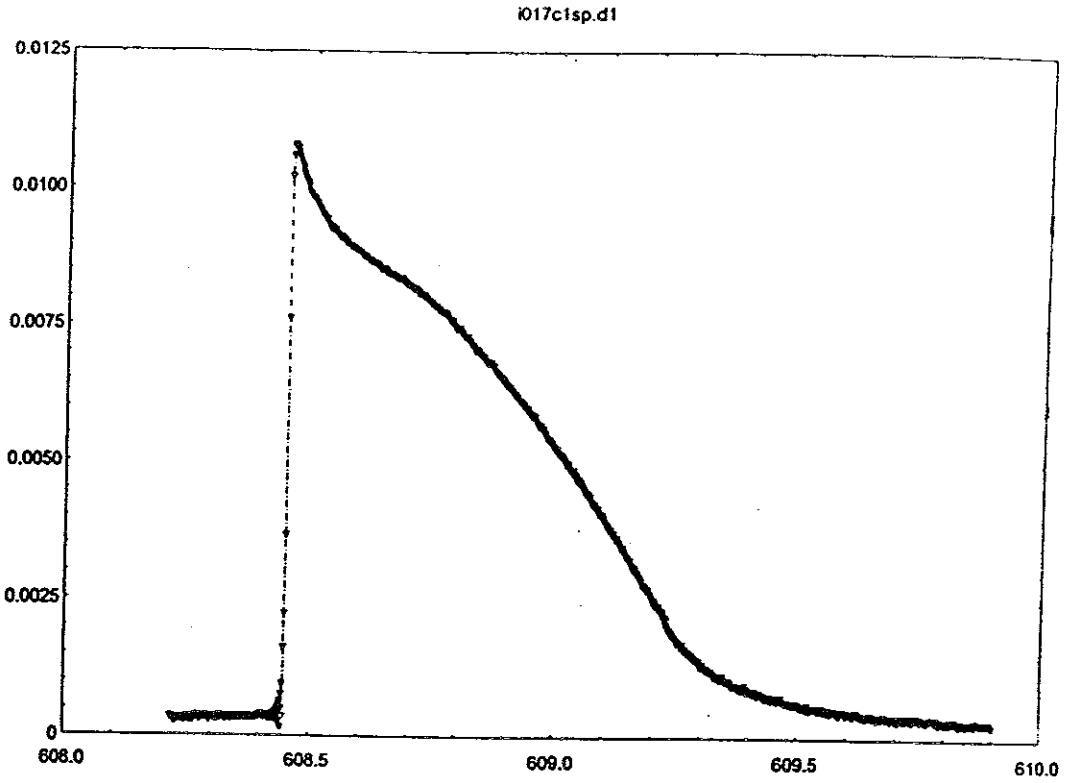

Figure 5-5: This scan of the (1,1) mode at high amplitude swirled the film. The shape would be expected to lean over farther to the left before reaching the peak amplitude on the graph, but the peak moved during the scan. Then the amplitude reached its maximum in the shifted location.

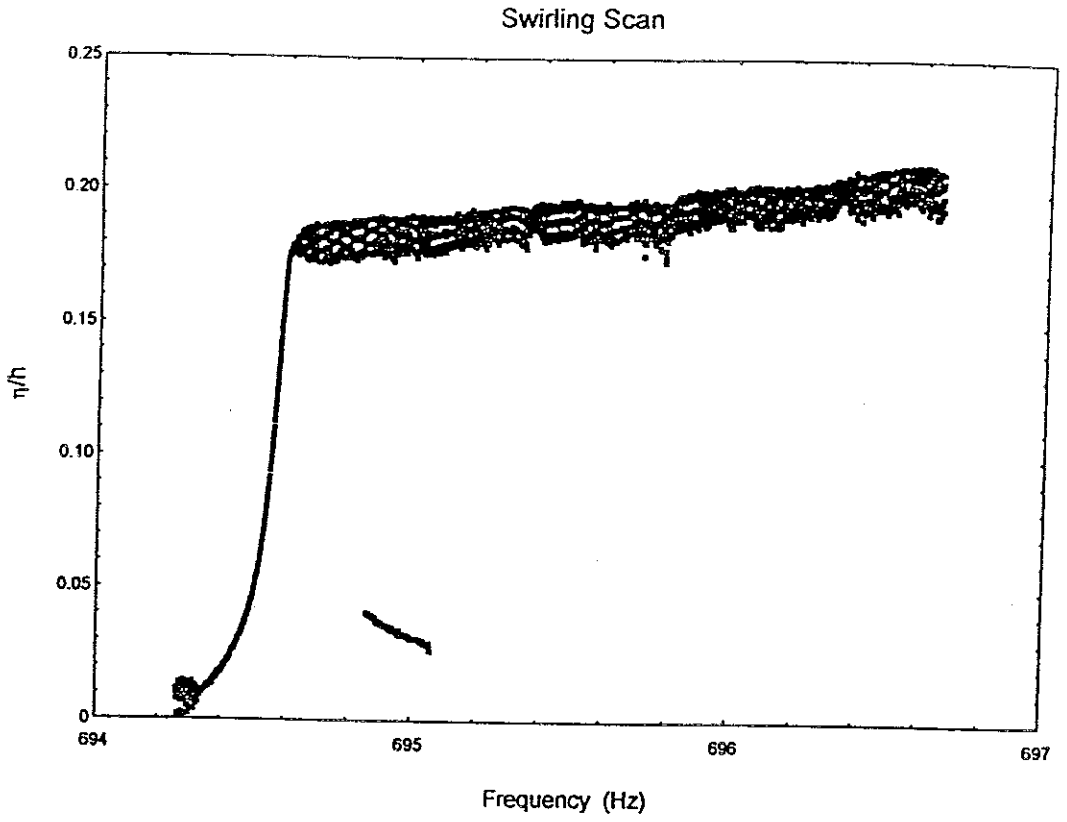

Figure 5-6: (2,1) surf, a.k.a. "funnies."

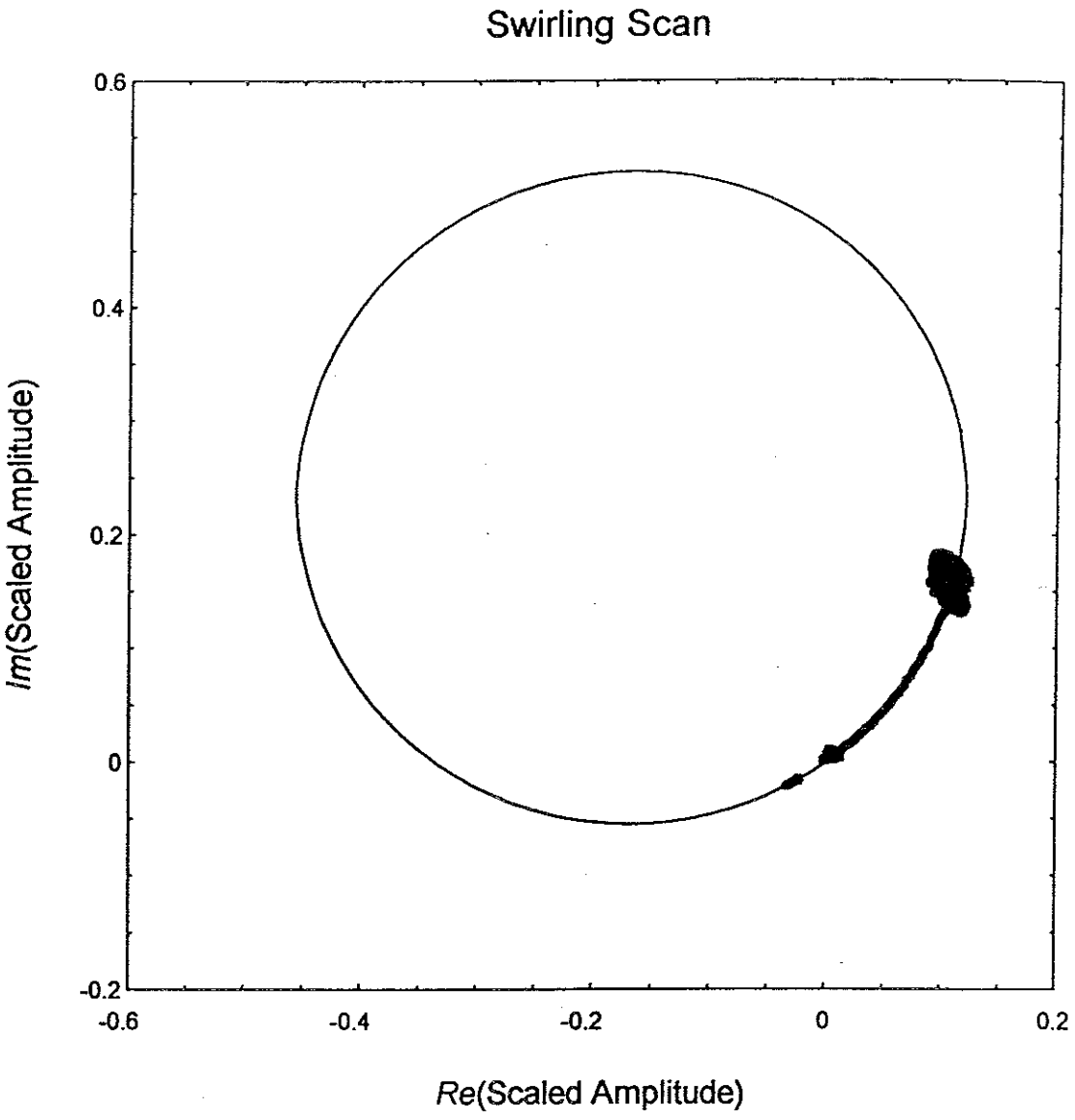

Figure 5-7: Real vs. imaginary part of figure 5-6. The surfing occurs at a fairly constant amplitude and phase, and the variations create the "blob" on the curve. Because the curve does not deviate from the circle its restoring force must be linear.

Lorentzian, so no non-linear restoring force is present (figure 5-7). When the swirling amplitude is reached, the peak moves, and the amplitude stays the same, which is the basis for its nickname of "surfing." Peaks have been surfed as fast as 1 Hz/min once they have gotten started. It is extremely difficult to swirl a film from a standstill using only the (2,1) mode, so a very small circulation of fluid should be started with the (1,1) first. The geometry of the drive plates is such that the drives should not couple to a standing (2,1) oscillation, but after the rotation has been started, it can be increased with the (2,1).

We have also had some success swirling the (2,1) with downward scans, but because the peak moves in the opposite direction to the scan, the down scans are not as effective as surfs. The data is very similar to that of the (1,1), indicating that the nonlinear restoring force is present, but Figure 5-8 shows that there is no hysteresis in the (2,1). Similar amplitudes can be reached under both upward and downward scans, which accounts for the (2,1)'s ability to swirl in either direction.

The (3,1) mode is very difficult to swirl with ScanDat, and a study of its swirling behavior has not been completed. It displays the same behavior as the (1,1) mode (figure 5-9). Interestingly, data from Fchart indicates that the (3,1) mode can move as fast as .3 Hz/hour, but the majority of film thicknesses we have attempted to swirl move much slower or not at all.

In an effort to determine what the vortices are doing when swirling occurs, we decided to examine the power dissipated by the swirling process. We have already established a mathematical form for the power:

$$P = \xi_m P_0 \left(\frac{\eta}{h}\right) \cos(\phi - \phi_{res}) . \qquad 2\text{-}42$$

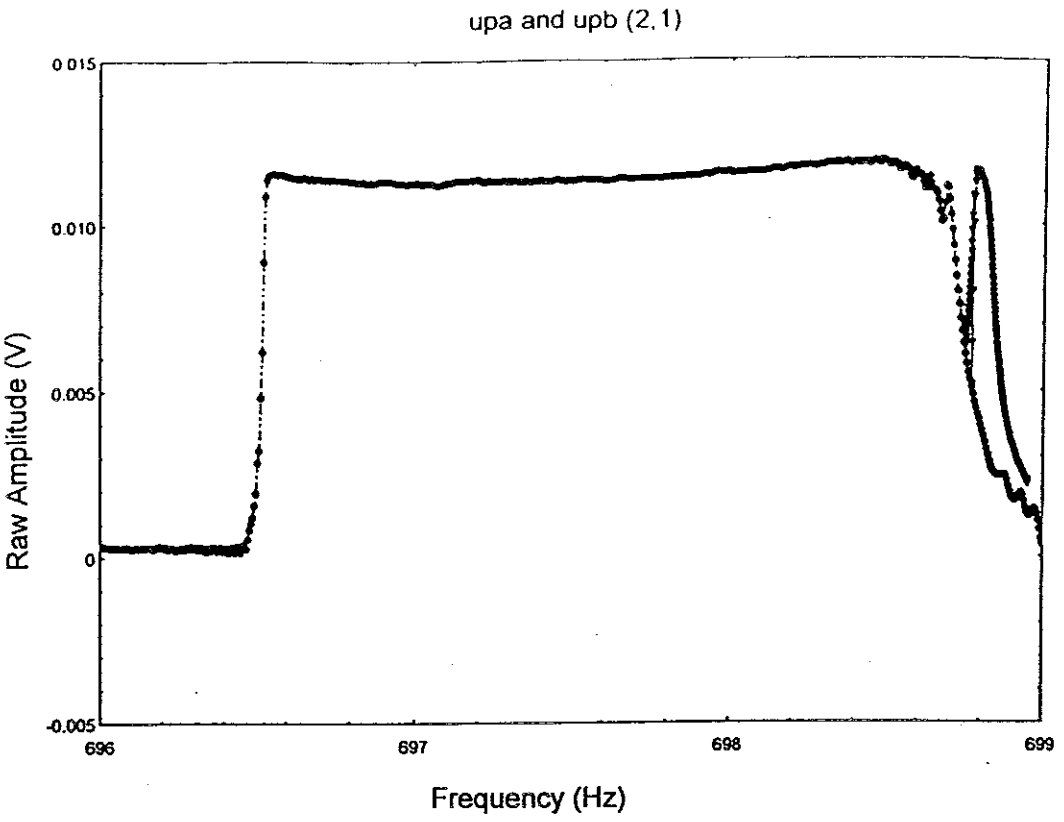

Figure 5-8: Scans from above and below a (2,1) resonance with an unswirled film. Neither swirled the film. Here the (2,1) does not surf or follow the hysteretic model. The same amplitude is reached scanning either direction, and the two curves do not overlap. Figure 5-11 shows that the (2,1) can swirl under scans in either direction under the proper conditions, indicating that it follows both models.

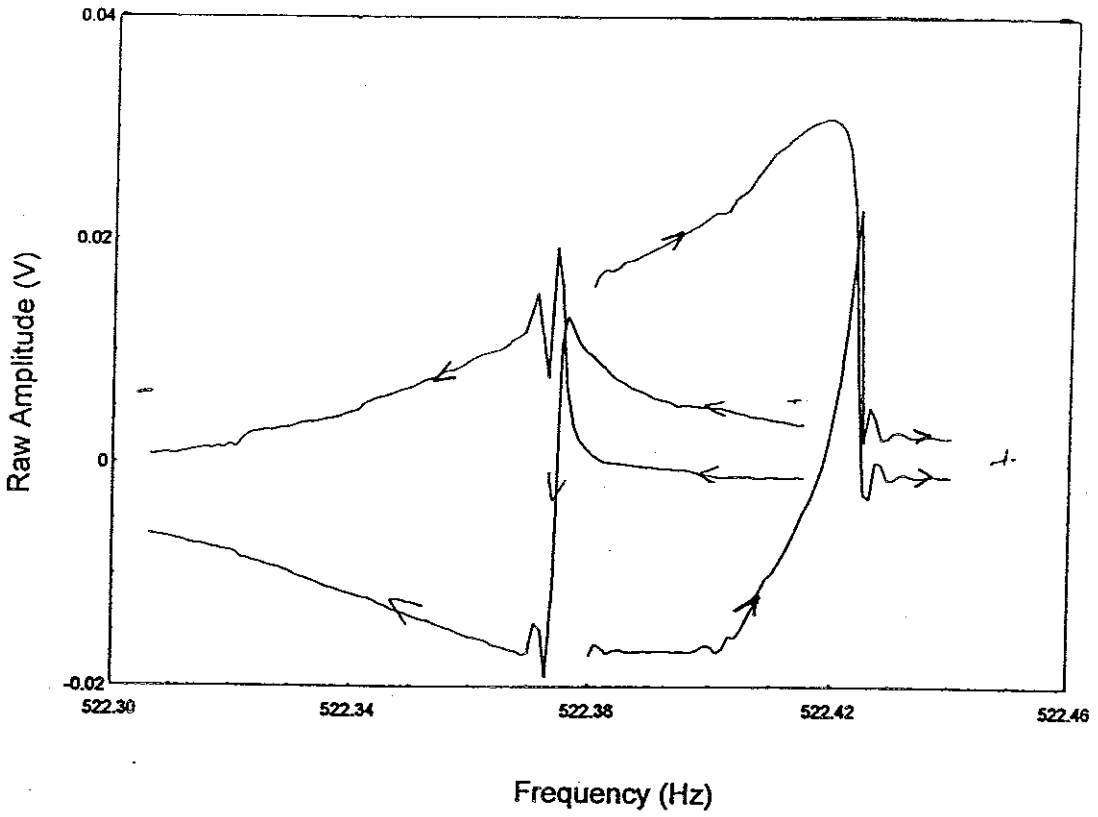

Figure 5-9: Real and imaginary parts of the amplitude from above and below a (3,1) resonance. This example of the hysteretic effect has reversed the roles of the up and down scans, which can be accounted for by changing the sign of the non-linear damping term.

A series of scans over the (1,1) (figure 5-10) and (2,1) (figures 5-11 and 5-12) at different drive amplitudes provided different values of η/h including swirling and non-swirling scans. The scans at smaller amplitudes did not swirl the film and the powers involved could be compared to those at higher drives that did swirl.

By examining many runs on the (1,1) and (2,1) and some on the (3,1), we were able to make some general observations about swirling even before analyzing the power usage. Downward scans always show an upturn in the curve when they swirl the film. Upward scans only surf, and the (2,1) is the only mode that has been observed surfing. Other observations were more subtle. The curves of the (1,1) series of scans fall on top of each other, which at first glance looks correct, until it is pointed out that the 30 V scans crash before some lower voltage scans. In theory, Duffing's equation, and in practice, an increase in drive amplitude means the entire curve's amplitude follows a different path (figure 5-3), so some explanation for the locations of the curves is necessary. The phase vs. frequency data revealed that the curves are phase shifted, and the shift is amplitude dependent. Recent work (Baierlein, 1997) described an amplitude dependent phase shift that we had studied sporadically over the last few years but had not connected with the high amplitudes reached during swirling. When the amplitude is high, coupling between different modes affects the position of the modes. Because the (1,1) and (2,1) frequencies are not multiples of each other, it is difficult to imagine that they couple, but higher overtones interact. To avoid energy level crossings, the (1,1) and (2,1) modes shift down. We do not believe it has anything to do with the swirling process, but is merely a factor to consider when examining the curves.

Continuing our analysis of swirling, we picked off the peak velocities where the film

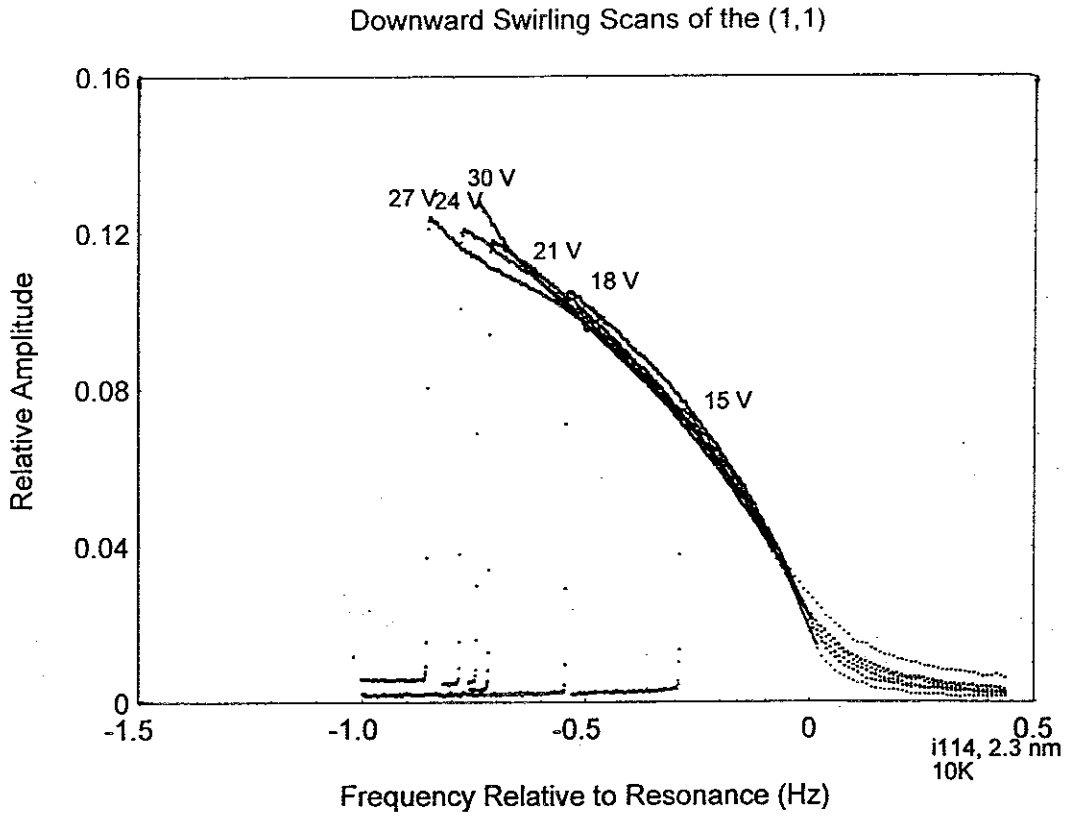

Figure 5-10a: Study of (1,1) swirling at different drive amplitudes. Amplitude vs. frequency.

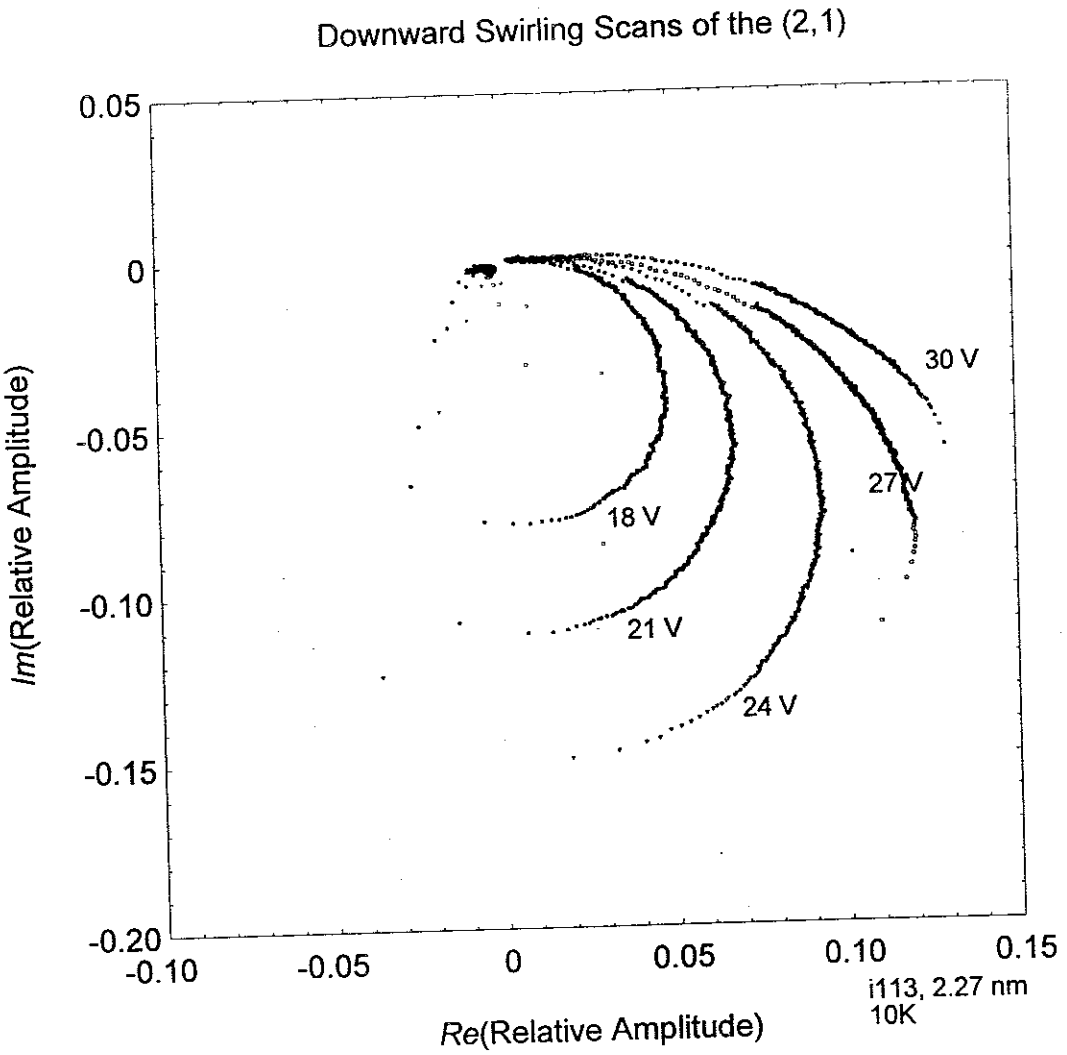

Figure 5-10b: Study of (1,1) swirling at different drive amplitudes. Imaginary amplitude vs. real amplitude.

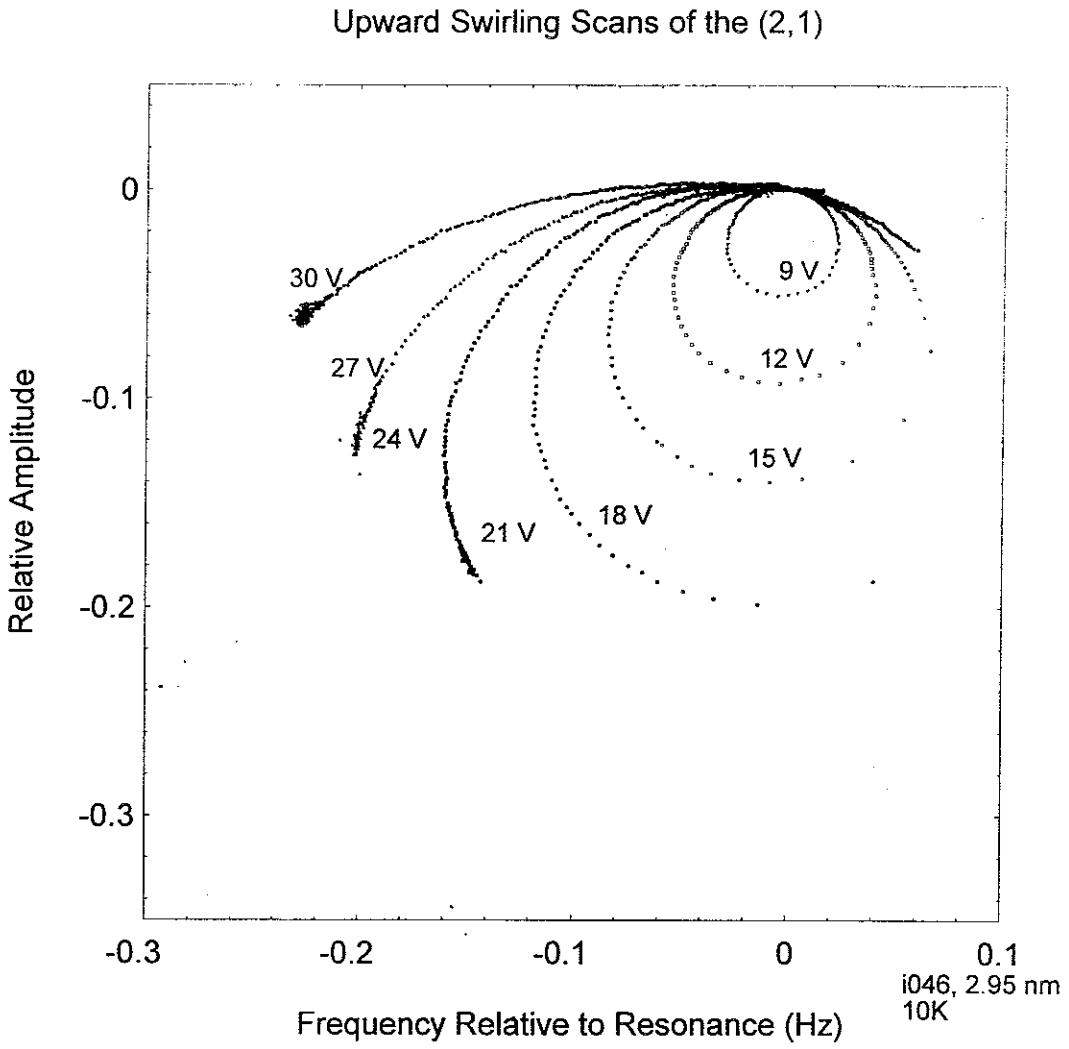

Figure 5-11b: Studies of (2,1) surfing at different drive amplitudes. Crashes show up in this type of diagram as large gaps between points, but unless the film swirls, the circle is completed.

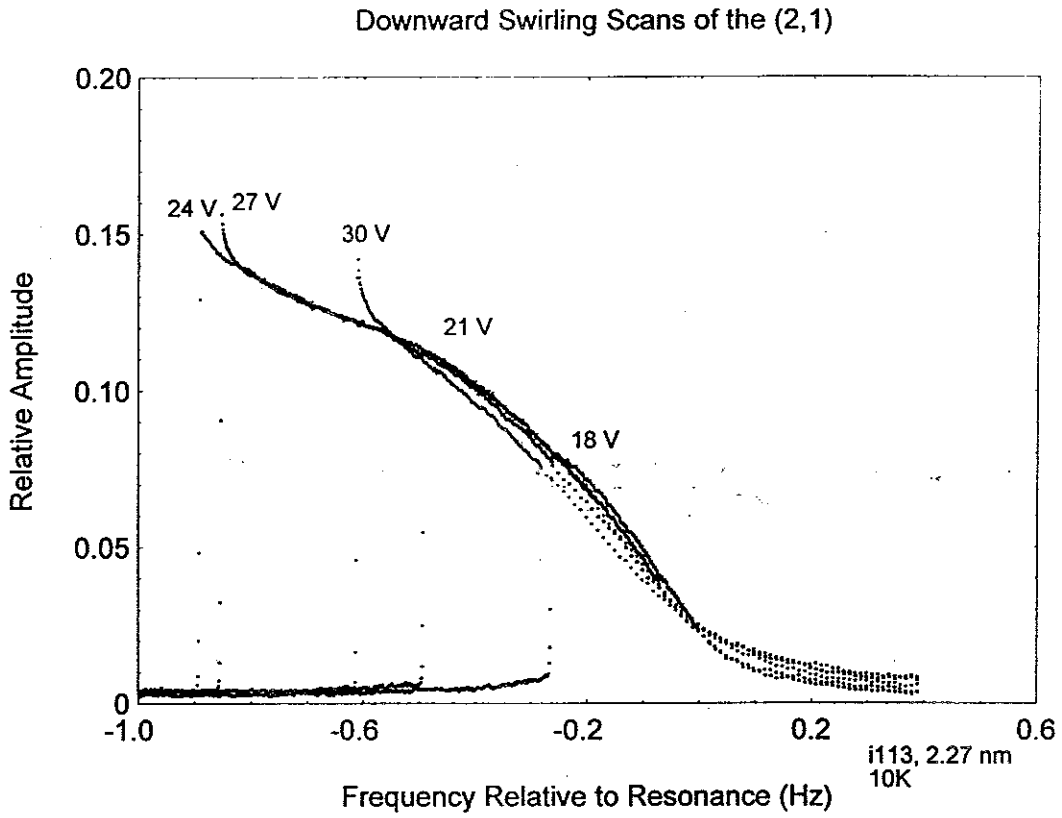

Figure 5-12a: Study of (2,1) swirling at different drive amplitudes under downward scans.

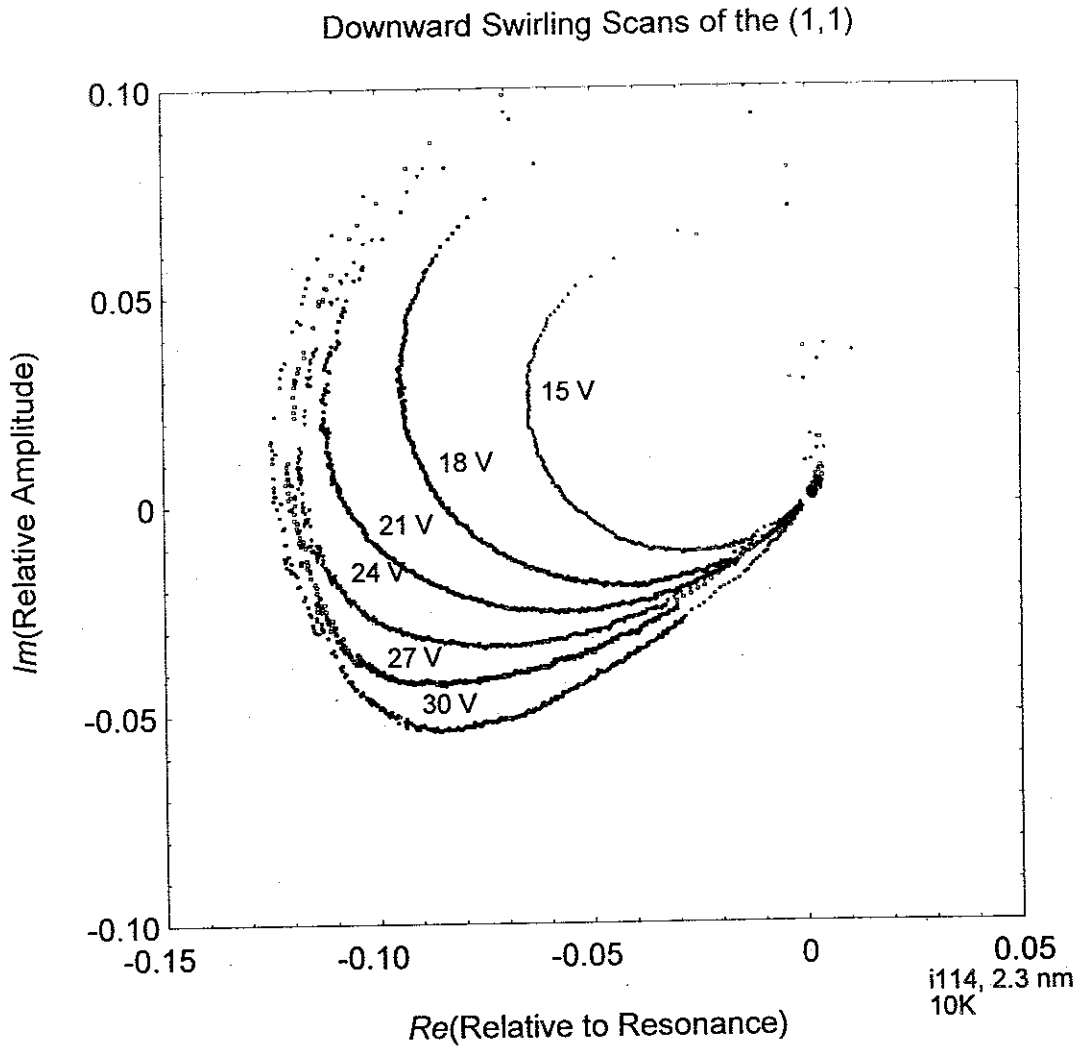

Figure 5-12b: Studies of (2,1) swirling at different drive amplitudes. Crashes show up in this type of diagram as large gaps between points, but unless the film swirls, the circle is completed.

swirled for different modes and film thicknesses (figure 5-13). The data shown includes all of the series data discussed above and some older data at thicker films, and illuminates several trends. One such trend is the low velocities at which the higher modes swirl. Because of the coupling between the drive and the higher modes, it is more difficult to achieve high peak velocities with higher modes. Given the low velocities, it would appear that the higher modes are easier to swirl once those velocities are reached, but the drag forces are comparable to those of the lower modes. A smaller velocity is needed for higher modes because the fluid motion under the higher mode oscillations is perpendicular to the radial vortex motion that increases circulation. For the (1,1) mode, the majority of the fluid motion is through the center of the cell, and therefore higher peak velocities are required. It also appears as though it is easier to swirl thinner films, but at some point the frequencies of thin films get too high to work with easily, and this is not represented in the figure.

The power data extracted from the series studies contained some ambiguities. We expected that a sharp increase in power usage would occur at the onset of swirling. The (1,1) power results (figure 5-14) did indeed turn up, but the powers from both sets of (2,1) series results (figures 5-15 and 5-16) bend only slightly, if at all. To look more closely at the data at the ends of the curves, we extracted the drag force on the vortices, γ, to see if it changed while the film was swirling. We found the drag force by writing the power as the drag on the fluid times the fluid velocity squared:

$$P = \langle F \cdot v \rangle_{time+space} = \langle \gamma v \cdot v \rangle_{time+space} \cdot Area_{cell} \qquad 5\text{-}3$$

Substitution of the peak fluid velocity,

$$v = c_3 \frac{\eta}{h} B_{fac}\,, \qquad 5\text{-}4$$

where B_{fac} (.5 for the (1,1), .36 for the (2,1), and .332 for the (3,1)) comes from the Bessel factors averaged over the cell, yields a form of the drag force inversely

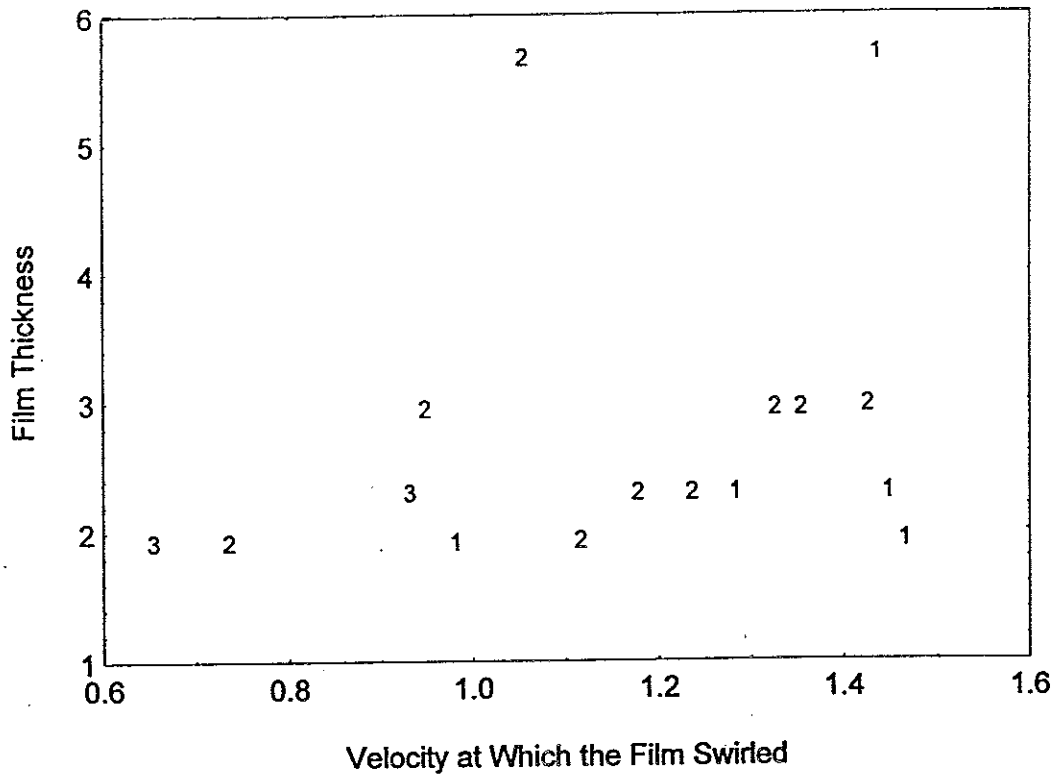

Figure 5-13: Film thickness vs. peak velocity where the film swirled, and by which mode. Some older data at thicker films is included along with the data from the series studies. 1 = (1,1) data, 2 = (2,1) data, and 3 = (3,1) data.

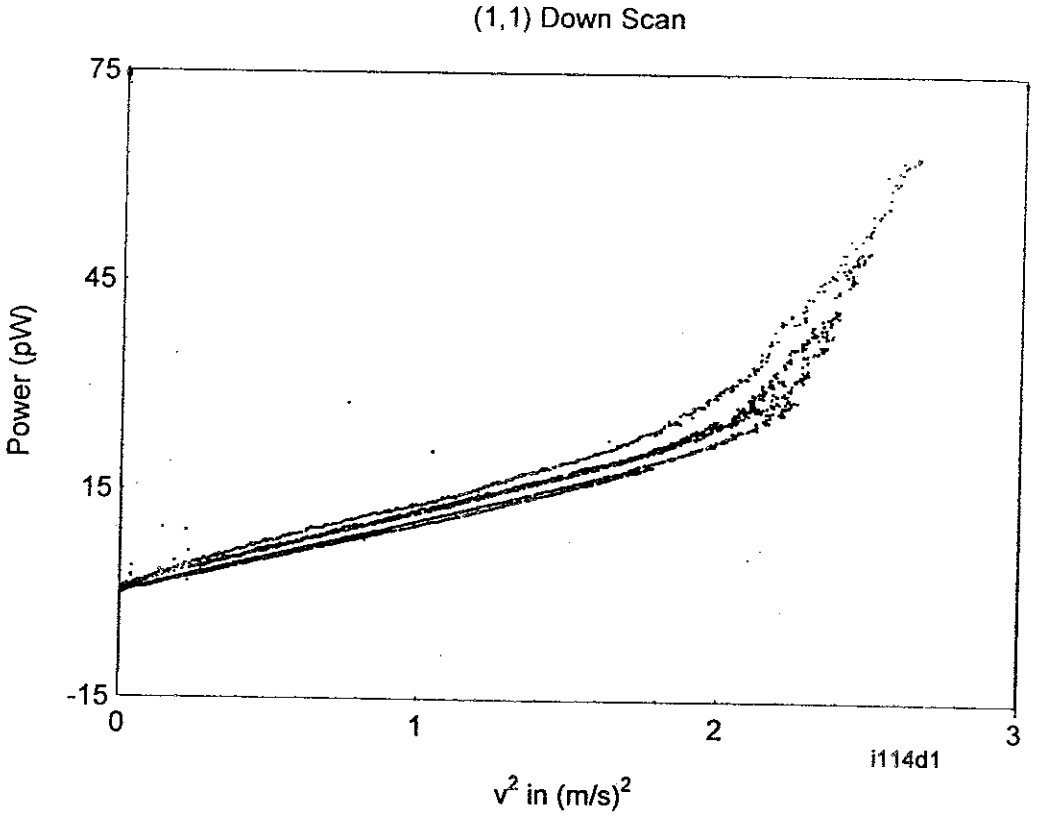

Figure 5-14: Power vs. peak velocity squared for the (1,1) downward scan data in figure 5-10.

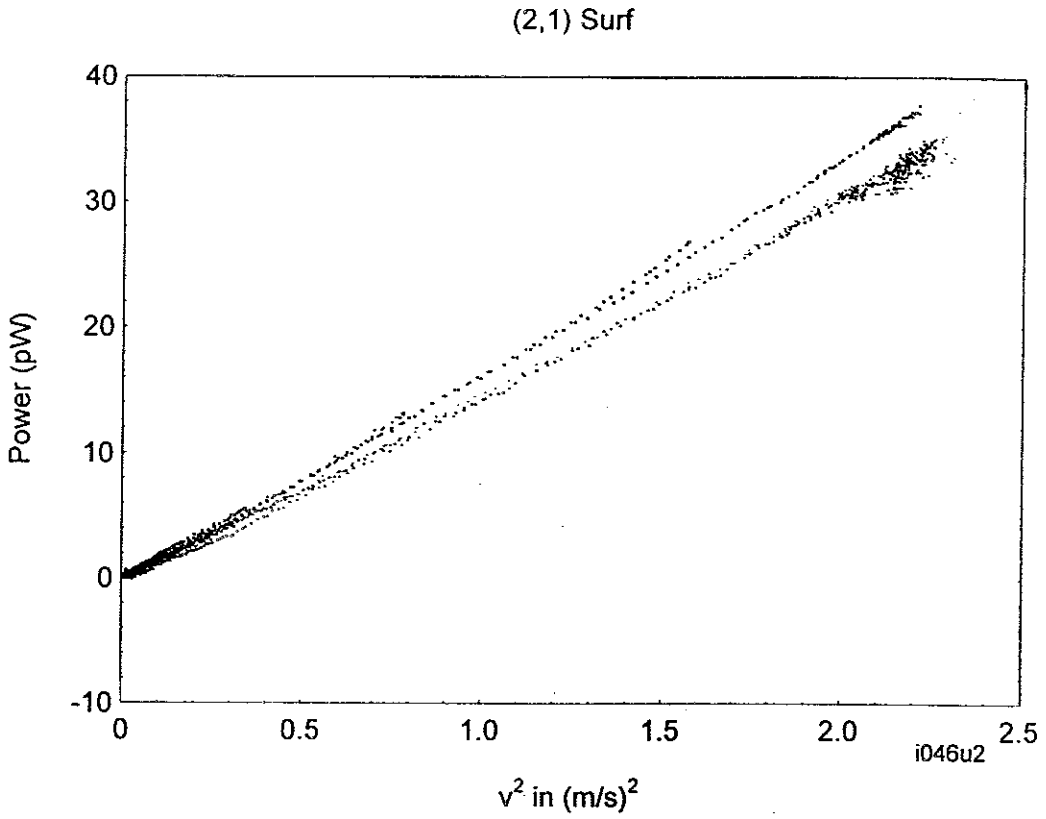

Figure 5-15: Power vs. peak velocity squared for the (2,1) surf data in figure 5-11.

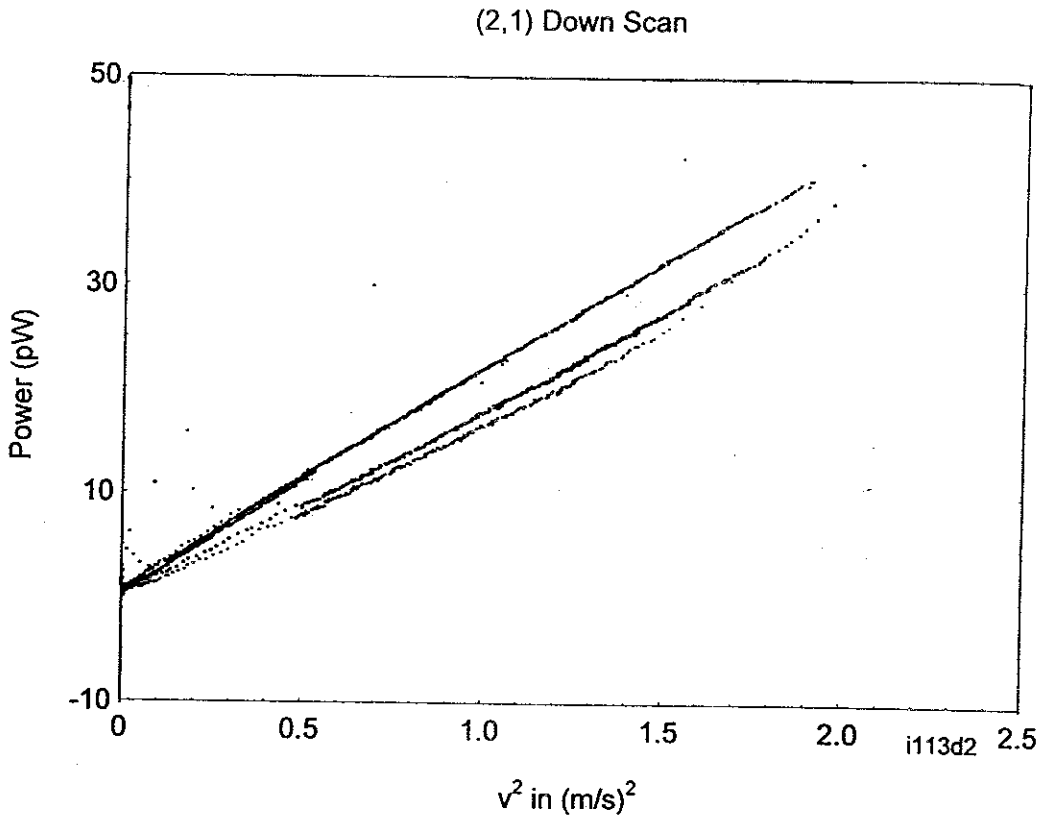

Figure 5-16: Power vs. peak velocity squared for the (2,1) downward scan data in figure 5-12.

proportional to the peak velocity squared

$$\gamma = \frac{P}{v^2 \cdot \pi a^2} \qquad 5\text{-}5$$

The units of γ are force per velocity per area. The power, P, is from the calculation in Chapter 2, and the area (like the Bessel factors in v) comes from the average over the cell area. The drag force data (figure 5-17) did not yield much more information than to confirm that the drag forces are all comparable until the (1,1) force increases. It should be noted that the (1,1) peak velocities are in general higher than those of the other modes, so it is possible that the other modes' forces would increase if the higher velocities were reached.

Given no obvious increase in power usage for the (2,1), we may tentatively conclude that there are many more vortices in the cell than we had previously thought, and that the net shift in vortex position that caused the swirling was a very small part of the overall vortex motion. A preliminary calculation of the power using the FlowFld program with a constant vortex density in the cell predicted that approximately 10^9 vortices would need to move to account for the experimental power. This information is consistent with STM data indicating that there are 10^{10} to 10^{16} pinning sites available in the cell. Fewer than 1 in 100 pinning sites could be occupied, spacing the vortices such that none could feel any significant influence from the others.

More data to investigate higher peak velocities at thicker films is in order. It is clear that there are two ways with which we can swirl the films, but whether the mechanisms behind them are different remains to be seen. If drag forces for the (2,1) and (3,1) modes increase at higher peak velocities, our work will be simplified, but until we can account for the concentration of vortices in the center of the cell after swirling, an understanding of the behavior of the vortices in the cell is still far away.

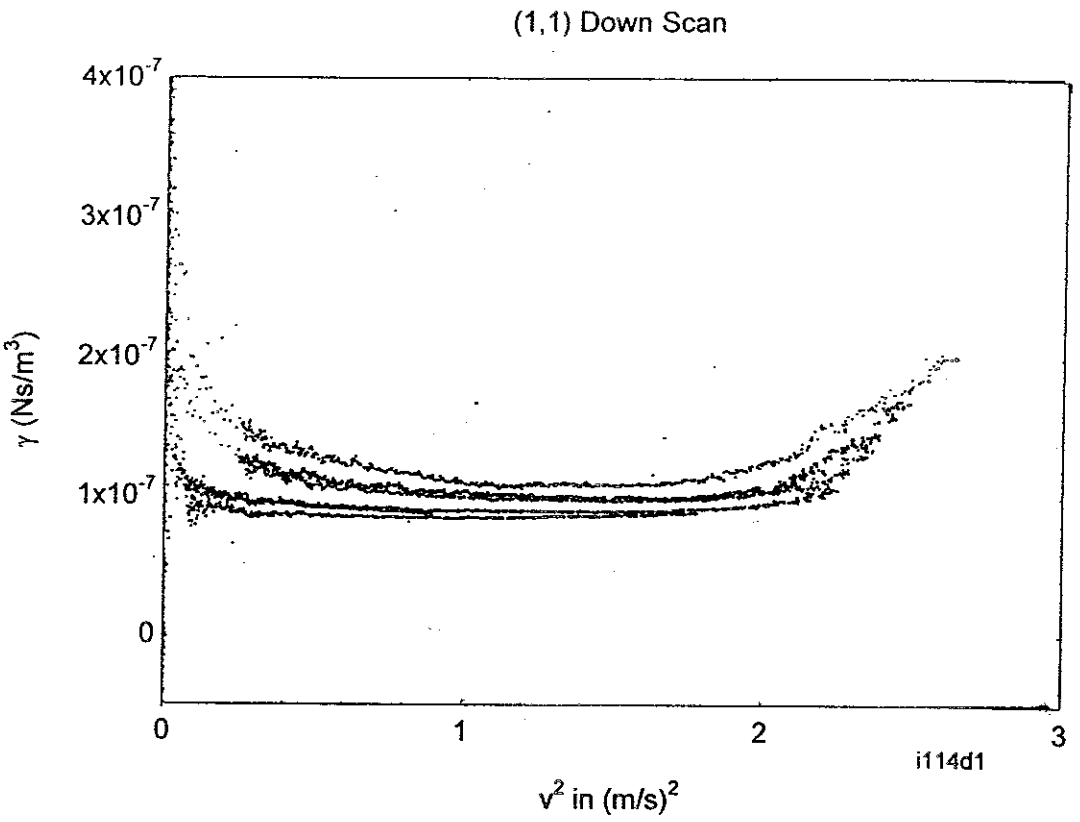

Figure 5-17: Viscous drag forces as a function of peak velocity squared for the data in figures 5-10, 5-11, and 5-12.

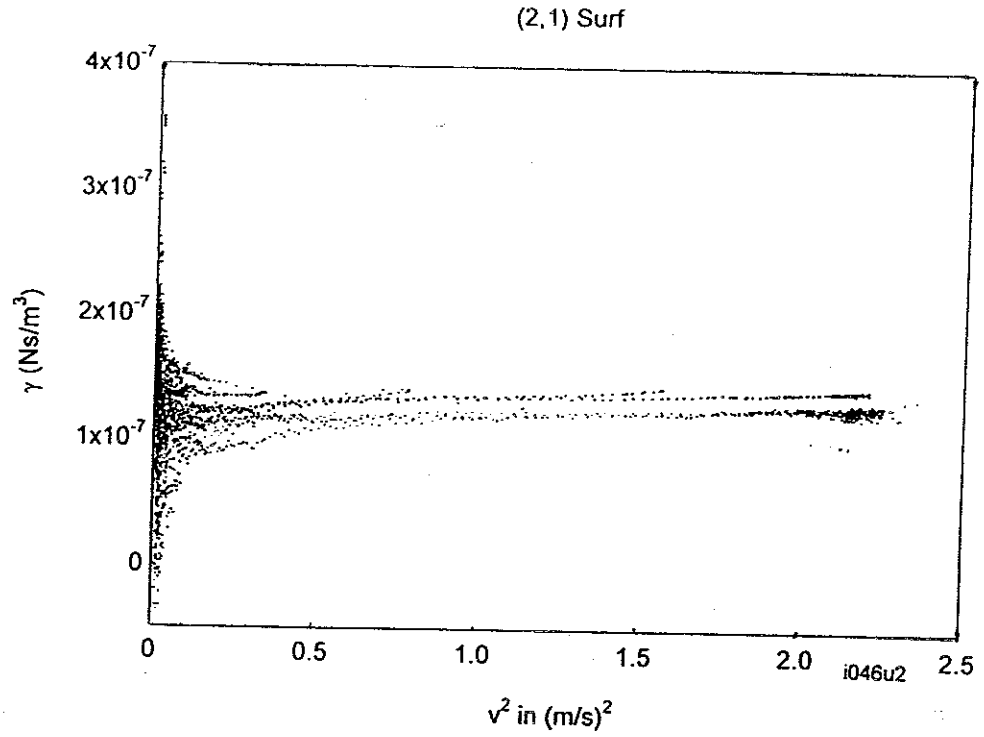
(2,1) Surf
4x10^-7
3x10^-7
2x10^-7
1x10^-7
0
γ (Ns/m^3)
0
0.5
1.0
1.5
2.0
2.5
i046u2
v^2 in (m/s)^2

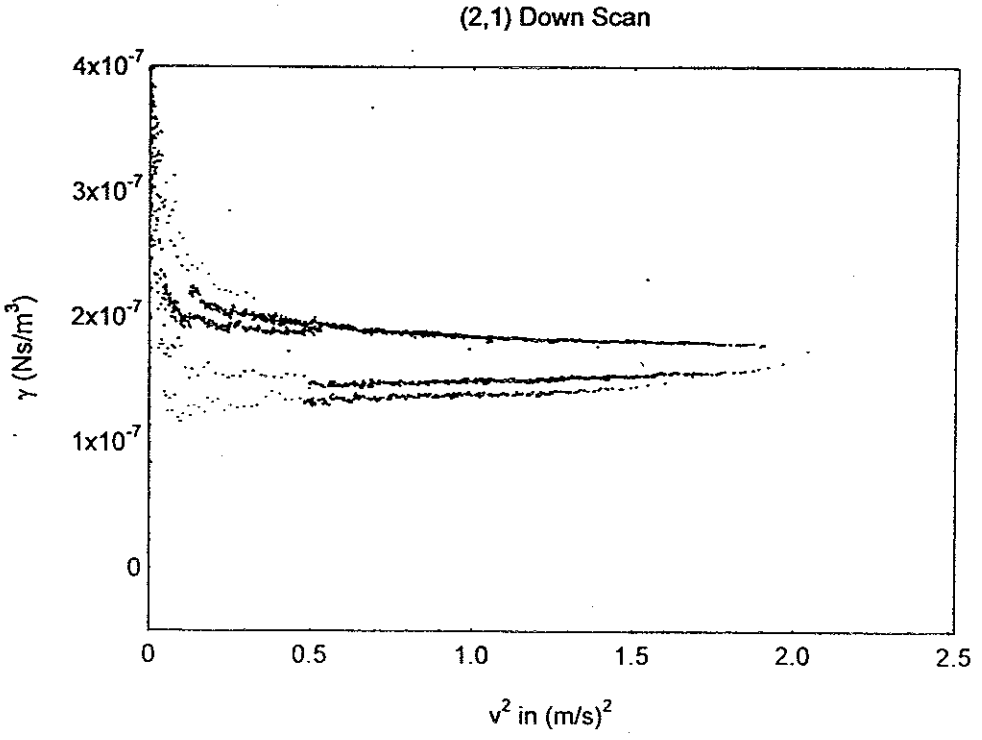
(2,1) Down Scan
4x10^-7
3x10^-7
2x10^-7
1x10^-7
0
γ (Ns/m^3)
0
0.5
1.0
1.5
2.0
2.5
v^2 in (m/s)^2

APPENDIX A

Cell Building Procedures and Methods

This is the history and documentation for a cell to replace the current one. It was not completed at the time of this writing.

We began with the goal of using a substrate other than glass in our capacitor construction because of the inconvenient dielectric properties of glass at low temperatures. Quartz was a logical replacement because we had some large pieces that we had used for the capacitor for the film thickness calibration (Appendix B). Unfortunately, holes were too difficult to drill in the quartz. We had to first etch the pieces coated in wax in hydrofluoric acid and then send them out to a company that could drill the holes with a CO_2 laser. The thickness and size of the etched areas were difficult to predict, as the pinholes in the wax were not uniform and hard to regulate. Also the laser company was not able to drill small enough holes to suit us. After we found a brochure from another company that suggested that holes were much easier to drill in sapphire, and we proceeded with that. Pieces ordered from ESCO were sent to an eximer laser company in NH, where the holes were drilled.

The next hurdle was making gold stick to sapphire. By itself, gold does not stick well to sapphire, even less well than it does to glass, and the In-Pb solder for attaching the silver alloy wires would not wet it. We tried both chromium and titanium under the gold, and if the boat and wire are correctly positioned as described below, either one works. The films and solder both stick very well. We chose to use titanium.

The pieces were prepared by scrubbing them with a kimwipe in ammonium hydroxide

and let them sit in the NaOH in the ultrasonic cleaner for five minutes. It worked best if they were placed in a small plastic cup on edge, propped against the edge of the cup. They were then placed in trichloroethylene in the ultrasonic cleaner, and finally dipped in water and blown dry with dry nitrogen gas. When they were ready to be placed in the evaporator, we put the titanium wire parallel to the gold boat approximately an inch apart with a baffle equidistant between them. Without the baffle, neither titanium nor chromium worked; in both cases, the gold was contaminated during the evaporation of the other metal, and during the gold evaporation the vapor pressure was not high enough to deposit much gold.

The pieces were secured in their masks and properly aligned. The small piece of sapphire had a simple mask made by drilling two overlapping holes in a sheet of brass. The larger hole had a diameter 4 mils larger than the ½''gasket punch, which was actually larger by several mils. The mismatched sizes allow the gasket and the deposited gold to be aligned visually later. The large mask used two crossed wires and a loop to divide the capacitor plates and was more difficult to work with because the wires had to be very tight across the surface of the sapphire. The top wire of the two that crossed was particularly difficult to keep tight. If any of the wires was not close enough to the surface, bridging of the plates by the Ti was inevitable. Fortunately, bridged plates may be reused. The gold comes off in aqua regia, which is 1 part HCl and 3 parts Nitric acid, in about 15 minutes. The Ti will come off after about 3 days in Sulfuric acid.

After 10-20 evaporations the gold became contaminated despite the baffle and had to be replaced. The Ti wire was only good for about 5 evaporations because it gets thinner and more brittle. For the first evaporation, a current of 17 A may be used, but by the fourth or fifth, only 12 A may be necessary. The current must also be turned

up slowly (approximately 2 A/min over 7 A worked well) so that the wire does not burn out prematurely.

The gluing stage was made more complicated by the sapphire also. The etched circle that was in the glass cell would have been very expensive to replicate, and we wanted to avoid having a ditch at the edge of the cell. Instead, we used a paper gasket cut from capacitor spacing paper with gasket cutters to make a ring with an inner diameter of ½'' and an outer diameter of 5/8''. The paper is found in old capacitors, and the oil in it must be removed by soaking it in trichlorethylene and methanol. After the sapphire pieces with newly deposited gold had been wiped on lens paper and the wires attached to the five plates on the big sapphire piece, the big piece was placed on the gluing apparatus. Then the gasket and the small piece were put on top of it. The inside of the paper doughnut was aligned with the outside of the evaporated circle on the smaller sapphire piece. The hole of the small piece had been aligned in the mask. The electrodes on the larger piece were centered on the hole where the wires in the mask crossed before evaportion, and the holes in the two pieces were aligned under the microscope using the microscope light showing through from the bottom. In bright enough light, the cross in the big piece was visible through the small piece as vague purplish lines, which were useful as a guide.

When the paper and the holes were aligned correctly, a small rectangular piece of microscope slide was placed over the top hole to close it and the fingers of the clamp could be lowered. The glass covering was made to fit under the clamp and not obscure the gasket area. The clamp was cranked down so that the unglued cell would not flap when air pressure was applied later.

The gluing process was the most difficult. The first step was to determine which

glues crack at low temperatures. The glue used for the glass cell was gone, and we decided to try something less expensive. We first settled on two-ton epoxy diluted to the proper runny consistency with methanol, but approximately one in ten times the glue formed a brittle surface. It was unclear if an adulterated glue would be reliable. Five minute epoxy and super glue both cracked at 77 K, but the diluted two ton epoxy held even when the pieces were dropped directly in the nitrogen with no prior cool down. Unfortunately the 2-ton epoxy hardened too fast and we had to switch to the Stycast 1266.

The glue was to soak into the paper, and if the center was pressurized correctly, not soak into the center of the cell. The trick was to get the glue in fast but then slow down as it got to the inner edge of the gasket. I found a pressure of 2 PSI over the ambient atmospheric pressure allowed the glue to seal evenly when it was first painted on (with a small brush, as fast as possible without making a big mess). Then the pressure could be reduced to .7 PSI over an atmosphere until the glue got to the boundary, when it should be turned up to .8 PSI to keep it from getting into the cell. (I never had much luck with this, but we ran out of gold and parts before I got too far.) If the gluing stage fails, the cell may be placed in tetrahydrofluorine for about 3 days. The glue is jelly-like at that point, and it gets into the holes in the sapphire and no way to remove it has yet been devised. At this time there are parts for two trial cells left out of five.

APPENDIX B

Capacitor Experiment to Convert Room Temperature Helium Gas Volume to Film Thickness by Measuring the van der Waal's Coefficient of Gold Evaporated on Quartz

Our previous values for film thickness relied on an average of several different values of the van der Waal's coefficient of helium on gold, T_V. We were unable to make our own measurements because useful data was masked by the peculiar dielectric properties of our glass substrate at low temperatures, which we eliminated for this experiment by switching to a quartz substrate.

We constructed a 32 pf capacitor by evaporating a 1000A layer of gold on quartz pieces and gluing the gold faces 12 μm apart. The capacitor was connected to the tunnel diode oscillator (TDO) circuit and placed under the mixing chamber of the dilution refrigerator with a capillary to allow helium into the capacitor region. Because helium is a weak dielectric, superfluid film on the capacitor plates resulted in a change in capacitance in the TDO circuit that was monitored using standard radio frequency detection techniques.

The thickness calibration was carried out by finding a relation between h and the measured frequency. To begin with, we mathematically divided the capacitor into three capacitors in series to account for the film on the top plate, the film on the bottom plate, and the gap between the films.

$$\frac{1}{C} = \frac{1}{C_h} + \frac{1}{C_h} + \frac{1}{C_d} \qquad \text{B-1}$$

h is the film thickness, and d is the gap between the plates minus twice h. Next, the TDO frequency could be found

$$f = \frac{1}{2\pi\sqrt{LC}}. \qquad \text{B-2}$$

By taking some derivatives and rearranging, a relation for the relative frequency change can be derived

$$\frac{\Delta f}{f} = -\frac{1}{2}\frac{\Delta C}{C}. \qquad \text{B-3}$$

Then we find the capacitance of the whole gap

$$C_g = \frac{\varepsilon\varepsilon_0 A}{\varepsilon d - 2h(\varepsilon - 1)} + C_0 \qquad \text{B-4}$$

where ε_0 = permittivity of free space, ε = permittivity of helium, and C_0 = stray capacitance. By taking the derivative of the gap capacitance with respect to h, we can find a relation between the change in film thickness, η, and the RF signal we detect.

$$\frac{\Delta f}{f} = \frac{(1-\varepsilon)\eta}{\varepsilon d}. \qquad \text{B-5}$$

This result is useful, but still fails to tell us the film thickness because we do not know d if we do not know η. Using the change in capacitance from the empty cell to the full cell to calibrate d and employing eqn B-3 we find:

$$\frac{\Delta f}{f} = \frac{2\eta C_f \Delta f_{e-f}}{\varepsilon\varepsilon_0 A f_f} \qquad \text{B-6}$$

where C_f = capacitance of the cell when it has been filled with helium, Δf_{e-f} = the change in TDO frequency from the empty cell to the full cell, A = the area of the cell, and f_f = the TDO frequency when the cell has been filled with helium. A little algebra and the substitution of h for η yields the following:

$$h = \frac{\varepsilon\varepsilon_0 A f_f}{2C_f \Delta f_{e-f}} \frac{f_h - f_e}{f_e} \qquad \text{B-7}$$

where f_h = the TDO frequency when the cell is partially filled. The data can be fit to a line

$$h = K(f_h - f_e) \qquad \text{B-8}$$

where K is the slope, given by

$$K = \frac{\varepsilon\varepsilon_0 A f_f}{2C_f \Delta f_{e-f} f_e}. \qquad \text{B-9}$$

Thus, the film thickness was easily determined (figure B-1).

Having calculated h to our satisfaction, we could compare the experimental h values to the theoretical relation between third sound and h to find our own value of T_V.

$$c_3^2 = h\left(\frac{\partial}{\partial z}U(z)\right)\Big|_h = \frac{3k_B T_V}{m_4}\left(\frac{z_1}{h}\right)^3 \qquad \text{2-16}$$

we find a simple relation between the film thickness and the wave speed. In fact, to be extremely accurate, there are many factors that can be included:

$$c_3^2 = \frac{\rho_s}{\rho}\left(\frac{h-d}{h}\right)\frac{3k_B T_V}{m_4}\left(\frac{z_1}{z}\right)^3 \frac{1}{\left(1+\frac{z}{z_r}\right)} \qquad \text{2-17}$$

After taking the log of both sides of the equation, the data can be fit to a straight line, and the Van der Waal's coefficient can be extracted. From figure B-2, the slope of the line is

$$slope = \frac{1}{2}\ln\left(\frac{3k_B T_V}{m_4} z_1^3\right). \qquad \text{B-16}$$

Having determined the value of T_V, the conversion from c_3 to h is a matter of using

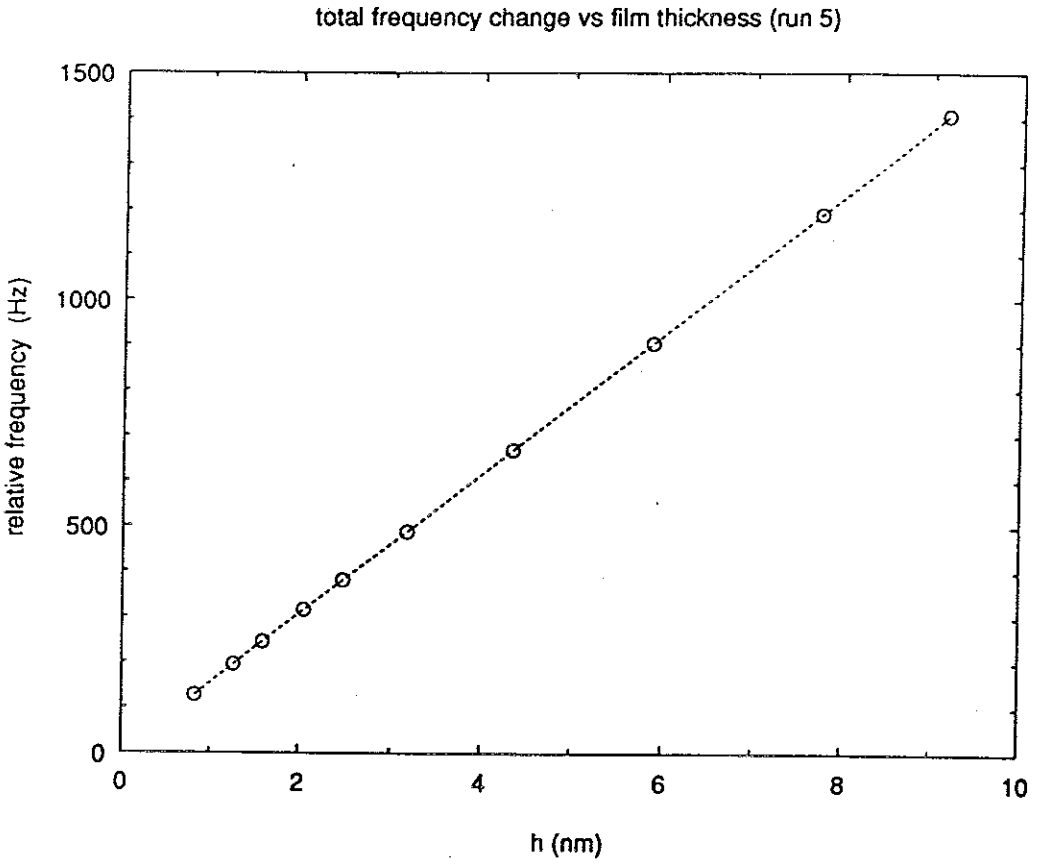

Figure B-1: An example of the total frequency change of the TDO circuit as the film thickness in the single capacitor was increased.

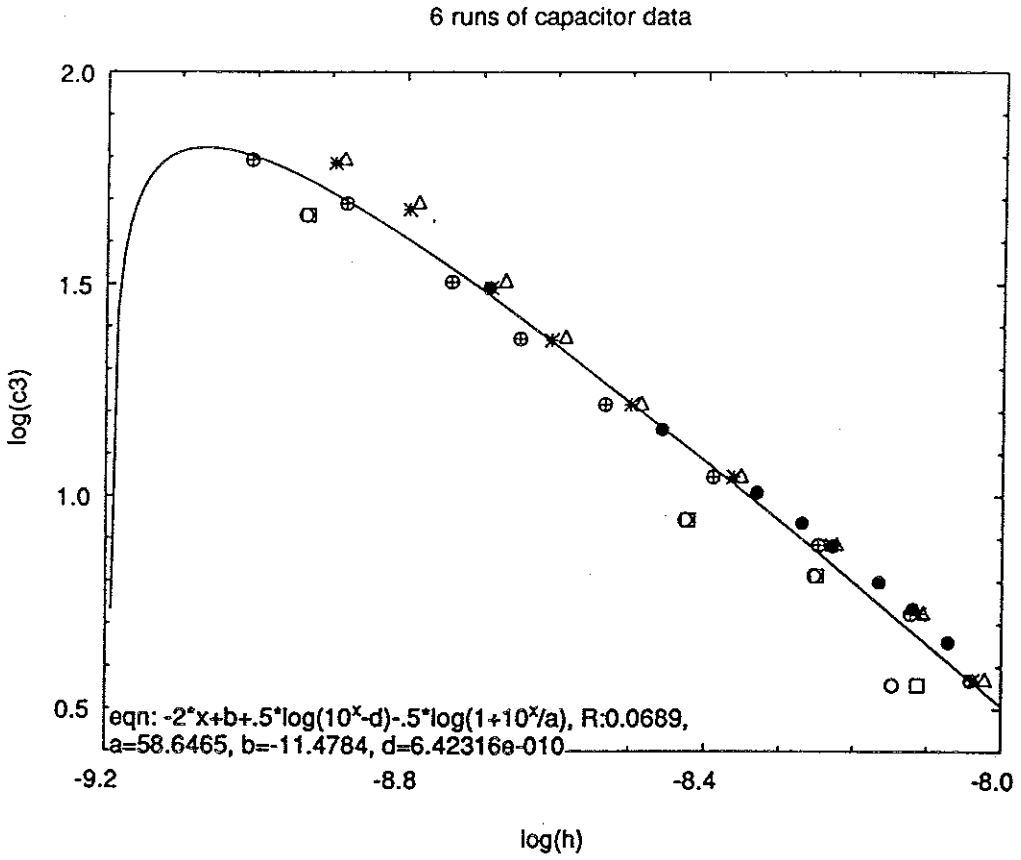

Figure B-2: An example of data used to find T_V.

equation B-15.

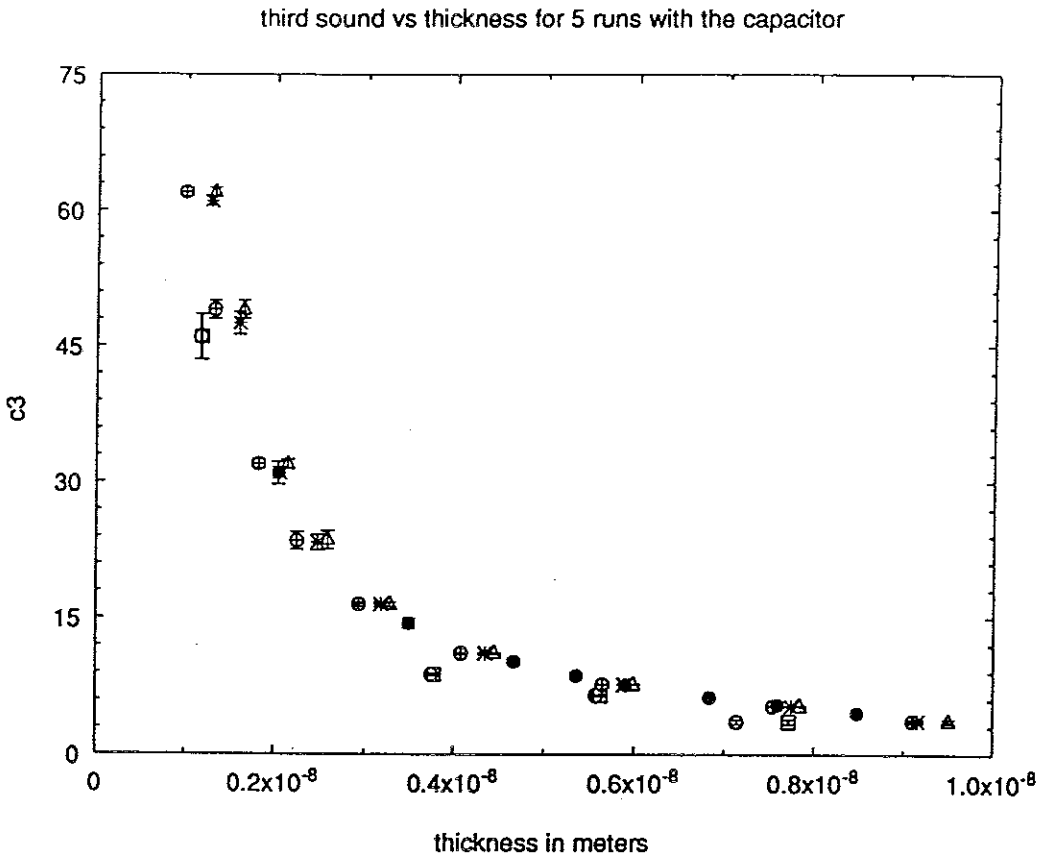

Figure B-3: Our calibration of third sound speed (m/s) vs. the film thickness.

APPENDIX C

MathCad documents:

1. Calculation of the flow field in the cell from splitting data.
2. Back of the envelope power calculation
3. Resonator information
4. Drive and pickup information
5. A mathematical calculation of splitting proportionalities

FLOW FIELD ANALYSIS FROM THE 123 MODE SPLITTINGS - 7/21/93

The matrix M represents the circulation perturbation constants for the (1,1), (2,1), and (3,1) modes, (rows) for flow fields of the form 1/r, 1, and r (columns),

$$M_\gamma := \begin{pmatrix} 1.27 & .153 & .089 \\ 1.17 & .630 & .409 \\ 1.13 & .755 & .549 \end{pmatrix}$$

.e. the shifts of the first three modes due to the flow field

$$v(r) := C_3 \cdot \left(c_0 \cdot \frac{a}{r} + c_1 + c_2 \cdot \frac{r}{a} \right) \qquad \text{is} \qquad \begin{bmatrix} \gamma_1 \\ \gamma_2 \\ \gamma_3 \end{bmatrix} = M_\gamma \cdot \begin{bmatrix} c_0 \\ c_1 \\ c_2 \end{bmatrix}$$

From the experimental shifts of the 1,2, and 3 modes,

$$\gamma := \begin{pmatrix} .0089 \\ .0104 \\ .0110 \end{pmatrix}$$

find the "strengths" of the 1/r, 1, and r flows

$$c := M_\gamma^{-1} \cdot \gamma \qquad \text{or} \qquad c = \begin{pmatrix} 0.00652 \\ 9.64352 \cdot 10^{-4} \\ 0.00529 \end{pmatrix}$$

and plot the flow field, v(r), and the vortex density, n(r).

$C_3 := 1000$ $\quad a := .615$ $\quad n_0 := \dfrac{6.646 \cdot 10^{-24} \, C_3}{6.626 \cdot 10^{-27} \cdot a}$ $\quad N_0 := c_0 \cdot \left(n_0 \cdot 2 \cdot \pi \cdot a^2 \right)$

$x := .02, .04 .. 1$ $\quad v(x) := C_3 \cdot \left(c_0 \cdot \dfrac{1}{x} + c_1 + c_2 \cdot x \right)$ $\quad n(x) := n_0 \cdot \left(c_1 \cdot \dfrac{1}{x} + 2 \cdot c_2 \right)$

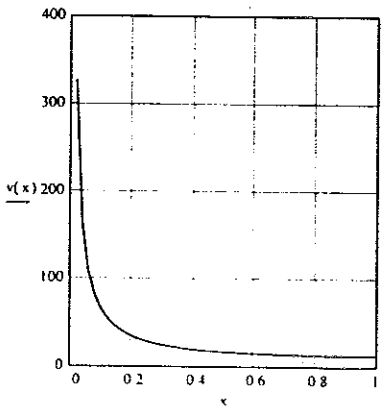

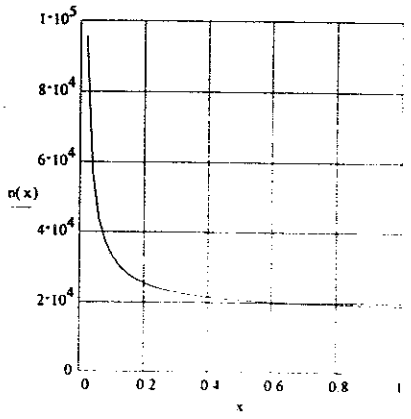

$N_0 = 2.52747 \cdot 10^4$

Now predict the shifts of higher modes based on their perturbation constants. The order of the rows is (1,1), (2,1), (3,1), (1,2), (5,1), (2,2), and (6,1).

First add a zero element to c... $c \quad \text{augment}\left(\text{identity}(3), \begin{pmatrix}0\\0\\0\end{pmatrix}^{T}\right) \cdot c$

Now multiply out perturbation constants...

$$M_\gamma = \begin{bmatrix} 1.27 & .153 & .089 & .074 \\ 1.17 & .630 & .409 & .296 \\ 1.13 & .755 & .549 & .423 \\ 1.36 & .331 & .173 & .104 \\ 1.09 & .849 & .683 & .565 \\ 1.34 & .538 & .284 & .173 \\ 1.08 & .872 & .721 & .609 \end{bmatrix} \qquad \gamma = M_\gamma \cdot c \qquad \gamma = \begin{bmatrix} 0.0089 \\ 0.0104 \\ 0.011 \\ 0.0101 \\ 0.01154 \\ 0.01076 \\ 0.0117 \end{bmatrix} \qquad (\text{exp}) = \begin{bmatrix} .00817 \\ .00668 \\ .00588 \\ .00980 \\ .00543 \\ .01160 \\ .00549 \end{bmatrix}$$

$a_{x\cdot 50} := x$

$den_{x\cdot 50} := n(x) \qquad vd_{x\cdot 50} := v(x)$

WRITEPRN(density) := augment(a, den)

WRITEPRN(vdrift) := augment(a, vd)

DRIVE CAPACITOR POWER

Assume that the film adsorbed on both surfaces a parallel plate capacitor is oscillating in response to an oscillating applied voltage. Find the mechanical power applied to the film by calculating the electrical power supplied by the drive source.

drive voltage $V(t) \equiv V_0 \cdot \cos\left(\frac{\omega \cdot t}{2}\right)$ note that the drive is half the frequency of the response

film thickness $h(t) \equiv h_0 + \eta \cdot \cos(\omega \cdot t + \phi_0)$

capacitance $C(t) \equiv \frac{C_0}{1 - 2 \cdot \frac{h(t)}{g} \cdot \left(1 - \frac{\varepsilon_0}{\varepsilon}\right)}$

C_0 is the empty capacitance

g is the plate gap

ε is the helium permitivity

The work done in each cycle of thickness oscillation can be found by the electrical work done by the voltage source, and the power is this work times the frequency.

$$dW \equiv V \cdot dQ \equiv V \cdot \left(C \cdot \frac{d}{dt} V + V \cdot \frac{d}{dt} C\right) \cdot dt$$

$$P \equiv \frac{\omega}{2 \cdot \pi} \cdot \int_0^{\frac{2 \cdot \pi}{\omega}} V \cdot \left(C \cdot \frac{d}{dt} V + V \cdot \frac{d}{dt} C\right) dt$$

Expanding the small thickness term in the denominator of the capacitance and throwing away the terms that integrate to zero leads to the result,

$$P \equiv -\frac{1}{4} \cdot \omega \cdot C_0 \cdot V_0^2 \cdot \frac{\eta}{g} \cdot \left(1 - \frac{\varepsilon_0}{\varepsilon}\right) \cdot \sin(\phi_0)$$

Taking the thickness oscillations to be the film thickness, and the phase for maximum power gives the standard power unit for the resonance experiments.

$$P_0 \equiv \frac{1}{4} \cdot \omega \cdot C_0 \cdot V_0^2 \cdot \frac{h_0}{g} \cdot \left(1 - \frac{\varepsilon_0}{\varepsilon}\right)$$

With typical numbers for the present drive plate,

$\varepsilon_0 \quad 8.85 \cdot 10^{-12} \quad \varepsilon \quad 1.055 \cdot \varepsilon_0 \quad a \quad .00615 \quad g \quad 9.6 \cdot 10^{-6} \quad \omega \quad 4 \cdot \pi \cdot 700 \quad C_0 \quad \frac{\varepsilon_0 \cdot \pi \cdot a^2}{4 \cdot g}$

$V_0 \quad 10 \quad h_0 \quad 2.93 \cdot 10^{-9}$

$$\frac{1}{4} \cdot \omega \cdot C_0 \cdot V_0^2 \cdot \frac{h_0}{g} \cdot \left(1 - \frac{\varepsilon_0}{\varepsilon}\right) = 9.58223 \cdot 10^{-11}$$

TWO DRIVES

In the rotating drive configuration, the two drives just add their power together, provided the drives are phased correctly. For odd modes, this is a 90 degree delay in the drive forces for the 90 degree plate. For even modes, the 90 degree plate must be driven at 180 degrees. The thickness oscillation "eta" must be replaced with an average over the drive plate. With the rotating wave definition

$$h = h_0 + \eta_0 \cdot J_m(kr) \cdot \cos(m\phi - \omega t)$$

and power definition

$$P = \xi_m \cdot P_0 \cdot \frac{\eta_0}{h_0} \cdot \cos(\Phi - \Phi_{res})$$

ξ_m is given by

$$\xi_m = \frac{16}{m \cdot \pi \cdot x_m^2} \cdot \left| \sin\left(\frac{m \cdot \pi}{4}\right) \right| \cdot \int_0^{x_m} x \cdot J_m(x)\, dx$$

calculating out...

$m := 1 .. 6$

$$x := \begin{bmatrix} 1 \\ 1.84118 \\ 3.05424 \\ 4.20119 \\ 5.31755 \\ 6.41562 \\ 7.50127 \end{bmatrix}$$

$$\xi_m := \frac{16}{m \cdot \pi \cdot (x_m)^2} \cdot \left| \sin\left(\frac{m \cdot \pi}{4}\right) \right| \cdot \int_0^{x_m} x \cdot Jn(m, x)\, dx$$

m	x_m	ξ_m
1	1.84118	0.85097
2	3.05424	0.43207
3	4.20119	0.16127
4	5.31755	0
5	6.41562	0.06928
6	7.50127	0.07175

CIRCULAR RESONATOR

Bessel function $J_m(kr)\cdot\cos(m\phi)$ with $\frac{d}{dx}J_m(x)=0$ at x_{mn} $\qquad k=\frac{x_{mn}}{a}$

m := 1 n := 1

$x := \pi\cdot\left(n - .674\cdot m^{.844} - .178\cdot\frac{m^{.768}}{n} - .956\right)$ $\qquad x_{mn} := \text{root}\left(\frac{d}{dx}Jn(m,x),x\right)$

not converging

$J_{mn} := Jn(m,\ )$ $\qquad J_{rms} := \sqrt{\frac{1}{2}\cdot\left[1-\left(\frac{m}{\ }\right)^2\right]}^{\cdot\ 2}$ (over area)

= = =

Standing Wave... $h_0 := 1$ $\eta := .04$ $a := 10$ $c := 30$ $k := \frac{\ }{a}$ $\omega := c\cdot$

$h(r,\phi,t) := h_0 + \eta\cdot Jn(m,\ \cdot r)\cdot\cos(m\cdot\phi)\cdot\cos(\ \cdot t)$

$$v(r,\phi,t) := c\cdot\frac{\eta}{h_0}\cdot\begin{bmatrix}-\frac{1}{\ }\cdot\frac{d}{dr}Jn(m,\ \cdot r)\cdot\cos(m\cdot\phi)\\ \frac{m}{\cdot r}\cdot Jn(m,\ \cdot r)\cdot\sin(m\cdot\phi)\end{bmatrix}\cdot\sin(\ \cdot t)$$

$$\delta(r,\phi,t) := \frac{\eta}{\cdot h_0}\cdot\begin{bmatrix}-\frac{1}{\ }\cdot\frac{d}{dr}Jn(m,\ \cdot r)\cdot\cos(m\cdot\phi)\\ \frac{m}{\cdot r}\cdot Jn(m,\ \cdot r)\cdot\sin(m\cdot\phi)\end{bmatrix}\cdot\cos(\ \cdot t)$$

Travelling Wave...

$h(r,\phi,t) := h_0 + \eta\cdot Jn(m,\ \cdot r)\cdot\cos(m\cdot\phi - \ \cdot t)$

$$v(r,\phi,t) := c\cdot\frac{\eta}{h_0}\cdot\begin{bmatrix}-\frac{1}{\ }\cdot\frac{d}{dr}Jn(m,\ \cdot r)\cdot\sin(m\cdot\phi - \ \cdot t)\\ \frac{m}{\cdot r}\cdot Jn(m,\ \cdot r)\cdot\cos(m\cdot\phi - \ \cdot t)\end{bmatrix}$$

$$\delta(r,\phi,t) := \frac{\eta}{\cdot h_0}\cdot\begin{bmatrix}-\frac{1}{\ }\cdot\frac{d}{dr}Jn(m,\ \cdot r)\cdot\cos(m\cdot\phi - \ \cdot t)\\ \frac{m}{\cdot r}\cdot Jn(m,\ \cdot r)\cdot\sin(m\cdot\phi - \ \cdot t)\end{bmatrix}$$

Peak velocities always occurs in azimuthal component

CAPACITIVE THIRD SOUND RESONATOR

Imagine that the mode in question is rigid in the sense that even at DC, the mode retains it's shape. Let the mode be described by an amplitude and a unitless mode function:

$$h(r,\phi,t) = h_0 + \eta \cdot \psi(r,\phi) \cdot e^{-i\omega t} \tag{1}$$

If this is the case, the electrostatic energy change due to the mode within the drive plate is given by

$$\Delta U_e = \int_{drive} u_v \, dV = \int_{drive} \frac{1}{2} \cdot \left(\varepsilon - \varepsilon_0\right) \cdot E^2 \cdot \eta \cdot \psi(r,\phi) \, dA \tag{2}$$

This the Van der Waals energy change associated with the same mode is

$$\Delta U_v = \int_{cell} u_a \, dA = \int_{cell} \frac{1}{2} \cdot \rho \cdot f \cdot \eta^2 \cdot \psi^2 \, dA \tag{3}$$

Equating the derivitives with respect to amplitude gives the DC mode amplitude, written in terms of the flat film DC thickness shift

$$\eta_{dc} = \eta_0 \cdot \frac{\int_{drive} \psi(r,\phi) \, dA}{\int_{cell} \psi^2 \, dA} \qquad \eta_0 = \frac{1}{2} \cdot \frac{\left(\varepsilon - \varepsilon_0\right) \cdot E^2}{\rho \cdot f} \tag{4a,4b}$$

Now, turning on the AC excitation of the mode, noting that the AC oscillations are between 0 and η_{dc}

$$\eta = \frac{\frac{1}{2} \cdot \eta_{dc}}{1 - \left(\frac{\omega}{\omega_0}\right)^2 - \frac{i \cdot \omega}{Q \cdot \omega_0}} \tag{5}$$

With a pickup capacitor that responds to a uniform DC shift by df/dh, the mode will contribute according to its average height:

$$\Delta f = \frac{df}{dh} \cdot \eta \cdot \frac{1}{A_{pick}} \cdot \int_{pick} \psi(r,\phi) \, dA \tag{6}$$

The drive and pickup integrals are more conveniently expressed in terms of normalizations to the whole cell:

$$D = \frac{1}{A_{cell}} \int_{drive} \psi(r,\phi) \, dA \qquad P = \frac{1}{A_{cell}} \int_{pick} \psi(r,\phi) \, dA \tag{7}$$

Put everything together

$$\Delta f \equiv \frac{df}{dh} \cdot P \cdot \frac{A_{cell}^{\,2}}{A_{pick} \cdot \int_{cell} \psi^2 \, dA} \cdot D \cdot \frac{\frac{1}{2} \cdot \eta_0}{1 - \left(\frac{\omega}{\omega_0}\right)^2 - \frac{i \cdot \omega}{Q \cdot \omega_0}} \qquad (8)$$

If the cell is a circle, radius a, with plates symmetric about y=0, only the cosine modes couple...

$$\psi = J_m\left(k_{mn} \cdot r\right) \cdot \cos(m \cdot \phi) \qquad (9a)$$

$$\frac{1}{A_{cell}} \cdot \int_{cell} \psi^2 \, dA \equiv \frac{1}{\pi \cdot a^2} \cdot \int_0^a \int_0^{2 \cdot \pi} \left(J_m\left(k_{mn} \cdot r\right) \cdot \cos(m \cdot \phi)\right)^2 \cdot r \, dr \, d\phi$$

$$\frac{1}{A_{cell}} \cdot \int_{cell} \psi^2 \, dA \equiv \frac{1}{a^2} \cdot \int_0^a J_m\left(k_{mn} \cdot r\right)^2 \cdot r \, dr \equiv \frac{1}{2} \cdot \left[1 - \frac{m^2}{\left(x_{mn}\right)^2}\right] \cdot J_m\left(x_{mn}\right)^2 \qquad (9b)$$

Including this

$$\Delta f \equiv \frac{df}{dh} \cdot P \cdot \frac{A_{cell}}{A_{pick} \cdot \left[\left[1 - \frac{m^2}{\left(x_{mn}\right)^2}\right] \cdot J_m\left(x_{mn}\right)^2\right]} \cdot D \cdot \frac{\eta_0}{1 - \left(\frac{\omega}{\omega_0}\right)^2 - \frac{i \cdot \omega}{Q \cdot \omega_0}} \qquad (10)$$

The pickup capacitor response is found from $\frac{\Delta C_p}{C_p} \equiv 2 \cdot \frac{\Delta h}{g} \cdot \left(1 - \frac{\varepsilon_0}{\varepsilon}\right)$ and $\frac{\Delta f}{f} \equiv -\frac{1}{2} \cdot \frac{\Delta C_p}{C_{total}}$ giving

$$\frac{df}{dh} \equiv -\frac{f_0}{g} \cdot \left(1 - \frac{\varepsilon_0}{\varepsilon}\right) \cdot \frac{C_p}{C_{total}} \qquad (11)$$

The "mode sensitivity" can also be written as

$$f_{mn} \equiv \frac{df}{dh} \cdot \frac{1}{A_{pick}} \cdot \int_{pickup} \psi(r, \phi) \, dA \equiv \frac{df}{dh} \cdot \frac{A_{cell}}{A_{pick}} \cdot P \qquad (12)$$

Summarizing the results of Hai's thesis, for an arbitrary linear combination of the m modes, the D and P should be replaced by the two component vector dot products

$$\vec{a} \cdot D \qquad a \cdot P \qquad (13)$$

The vector a is normalized and has components coresponding to the right (+m) and left (-m) polarized wave components so that the appropriate wave function is

$$\psi(r, \phi) = J_m \cdot k_{mn} \cdot r \cdot a_m \cdot e^{i \cdot m \cdot \phi} \cdot a_{-m} \cdot e^{-i \cdot m \cdot \phi} \qquad (14)$$

The integrals with ψ^2 in (4) and (8) remain integrals over the standing wave function (9a), not (14)

The integrals with ψ in (4) and (8) remain integrals over the standing wave function (9a), not (14),

and D and P have components given by,

$$D_m = \frac{1}{\sqrt{2}} \cdot \frac{1}{A_{cell}} \cdot \int_{drive} J_m\left(k_{mn} \cdot r\right) \cdot e^{-i\, m\phi}\, dA \qquad P_m = \frac{1}{\sqrt{2}} \cdot \frac{1}{A_{cell}} \cdot \int_{pick} J_m\left(k_{mn} \cdot r\right) \cdot e^{i\, m\phi}\, dA \qquad (15)$$

A few of the definitions are different from the notation in Hai's thesis:

1) D and P in (7) have been defined to be the same as the drive and pickup averages in the program fmncalc, and in (15) also include a "normalizing root" 2. The definitions in Hai's thesis also nomalize the integrals as in (4) and (6) as opposed to the cell area.

2) The DC film response (4b) to a field is incorrectly identified without the factor of 1/2 in Hai's thesis. The algebra in the thesis is still OK as he states it.

3) The drive integral in Hai's thesis includes a strength function G. Here it is assumed that the integral over the drive can be broken up to include drive plates with different phases.

CIRCULATION SPLITTING FACTOR CALCULATION

The evaluation of the circulation factors is done in three places, and they all agree.

linearization of the equations of motion and an analytic perturbation (in the circulation) treatment... (notes in the rotational c3 folder)

$$m := 1 \qquad xm := 1.84118 \qquad Jp(x) := \frac{Jn(m-1,x) - Jn(m+1,x)}{2}$$

$J_1'(x)$

$$f(x) := \left(\frac{x}{xm}\right)^{-1} \qquad \gamma_m := \frac{m \cdot \int_0^{xm} f(x) \cdot 2 \cdot Jn(m,x)^2 - \frac{2 \cdot Jp(x) \cdot Jn(m,x)}{x} \frac{d}{dx}(x - f(x))\, dx}{(xm^2 - m^2) \cdot Jn(m,xm)^2}$$

$\gamma_m = 1.278$

the model flow matrix is...

$$M := \begin{pmatrix} 1.278 & .1088 & .0886 \\ 1.170 & .6295 & .4090 \\ 1.129 & .7550 & .5490 \end{pmatrix}$$

The perturbation integral is calculated while the appropriate solution to Bessels equation are integrated. (same notes in the rotational c3 folder and CIRCFAC.BAS)

The linearized equations of motion are direclty integrated. (notes in the rotational c3 folder and DIRECT.BAS and DIRECT1.BAS)

both results for $\varepsilon = .025$ ...

$$M := \begin{pmatrix} 1.263 & .1443 & .0890 \\ 1.171 & .6295 & .4090 \\ 1.129 & .7551 & .5490 \end{pmatrix}$$

Both the m=1, v(r)=v(a) and the m=1, v(r)=v(a)*a/r terms deviate from the analytic perturbation because of the hole, and agree with it in the limit $\varepsilon = 0$

APPENDIX D

Three Different Calculations of the Relative Amplitude of a Wave

The relative amplitude of third sound waves can be theoretically calculated using data on the drive plates and the appropriate electromagnetic theory. Before expounding on the details of the different methods, a common ground for comparison must be established. Depending on where the calculation is used, it may be set in different forms. MathCad documents tend to use the complex formulation, and QB programs use the real version. Both versions can be derived from equation 2-15.

$$\frac{\eta}{h} = \frac{\frac{\eta_0}{h}}{\sqrt{4\left(\frac{\omega}{\omega_0} - 1\right)^2 + \frac{1}{Q^2}}} \qquad \text{D-1}$$

$$= \frac{\omega}{\omega_0} \frac{\frac{\eta_0}{h}}{1 - \left(\frac{\omega}{\omega_0}\right)^2 - \frac{i\omega}{Q\omega_0}} \qquad \text{D-2}$$

1) My way:

$$Q = \omega \frac{E}{P} \qquad \text{D-3}$$

The energy comes from Appendix C, mode_h_v.mcd

$$E = (\rho\pi a^2 h) c_3^2 \left(\frac{\eta}{h}\right)^2 J_{rms}^2(x_{mn}) \qquad \text{D-4}$$

where J_{rms} is defined in Circular Resonator (Appendix C). P is the power in Chapter 2.

Isolating η/h gives us the first value for the relative amplitude:

$$\frac{\eta_0}{h} = \frac{1}{2m\pi x_{mn}^2} \frac{V_0^2 \varepsilon_0 \left(1 - \frac{\varepsilon}{\varepsilon_0}\right)}{g^2 \rho c_3^2 J_{rms}^2(x_{mn})} \frac{\omega}{\omega_0} \sin\left|\frac{m\pi}{4}\right| \int_0^{x_{mn}} J_m(x) x dx \qquad \text{D-5}$$

This same form can be found from whatever.mcd in Appendix C, but using that calculation of ξ_m, the result is ½ the above result.

2) Hai's way:

Following Capacitive Third Sound Resonator in Appendix C,

$$\frac{\eta_0}{h} = \frac{1}{2m\pi} \frac{V_0^2(\varepsilon - \varepsilon_0)}{g^2 \rho c_3^2 J_{rms}^2(x_{mn})} \frac{\omega_0}{\omega} \sin\left(\frac{m\pi}{2}\right) \int_0^{x_{mn}} J_m(x) x dx \qquad \text{D-6}$$

3) Fmncalc's way:

$$\frac{\eta_0}{h} = -\frac{2}{m\pi} \frac{V_0^2 \varepsilon_0 (\varepsilon - 1)}{g^2 \rho c_3^2 J_{rms}^2(x_{mn})} \sin\left(\frac{3\pi m}{4}\right) \int_0^{x_{mn}} J_m(x) x dx \qquad \text{D-7}$$

APPENDIX E

Simulation of the Swirling Process

Using a conglomeration of programs, calculations, and models, we have attempted to simulate surfing. We began by selecting a mode, resonance frequency, and a reasonable critical velocity and then stepping the frequency starting below resonance. A theoretical expression was used at each frequency to calculate the amplitude of the wave and the fluid velocity under the wave. The theoretical amplitude was given by

$$\frac{\eta}{h} = \frac{\frac{\eta_0}{h}}{\sqrt{4\left(\frac{\omega}{\omega_0}-1\right)^2 + \frac{1}{Q^2}}}. \qquad \text{E-1}$$

η_0 was derived from the following relation:

$$Q = \omega \frac{E}{P}. \qquad \text{E-2}$$

where E is the energy used in a cycle

$$E = (\rho\pi a^2 h_0) c_3^{\,2} \left(\frac{\eta}{h}\right)^2 \left(J_{rms}(x)\right)^2, \qquad \text{E-3}$$

and

$$J_{rms} = \sqrt{\frac{1}{2}\left(1 - \frac{m^2}{x_{mn}^2}\right)\left(J_{mn}(x_{mn})\right)^2}. \qquad \text{E-4}$$

Solving for the relative amplitude yields

$$\frac{\eta_0}{h} = \frac{1}{4}\xi_m \frac{\omega}{\omega_0} \frac{\varepsilon_0\left(1-\frac{\varepsilon_0}{\varepsilon}\right)V_0^2}{c_3^2 \rho g^2 J_{rms}^2} \qquad \text{E-5}$$

$$= \frac{1}{2m\pi^2_{mn}} \frac{\omega}{\omega_0} \frac{\varepsilon_0\left(1-\frac{\varepsilon_0}{\varepsilon}\right)V_0^2}{c_3^2 \rho g^2 J_{rms}^2} \sin\left|\frac{m\pi}{4}\right| \int_0^{x_{mn}} J_m(x)x dx \qquad \text{E-6}$$

Several other formulations of the amplitude can be found in Appendix D. At the point where the fluid velocity exceeded the critical velocity, the new flow field was found as in Chapter 4. The amplitude at which the critical velocity was exceeded was given by

$$\eta = \frac{v_{crit}}{c_3 \cdot r_{v_{max}}} \qquad \text{E-7}$$

where the radius, *r*, is the scaled radial position of the peak flow under the wave.

From the new flow field, we calculated the splitting of the mode and the density of vortices

$$v(r) = \frac{\hbar}{m_4 r}\left[N_0 + \int_0 n(r) 2\pi r dr\right] \qquad \text{E-8}$$

$$n(r) = \frac{m_4}{2\pi\hbar}\left(\frac{\partial v}{\partial r} + \frac{1}{r}v(r)\right). \qquad \text{E-9}$$

With a simple accounting of the distance the theoretical vortices move during the flow field calculation and a vortex drag force against the substrate, we can find the power used to swirl the theoretical film at each radial position.

$$power = \frac{v_{crit}}{2\pi}\left|f\sqrt{v_x^2 + v_y^2}\right| d\phi \qquad \text{E-10}$$

where v_x and v_y are defined as

$$v = \begin{pmatrix} a & b & 0 \\ -b & a & 0 \\ 0 & 0 & 1 \end{pmatrix} \cdot v_s \qquad \text{E-11}$$

$$a = \frac{v_s^2(1+\gamma^2)+\gamma^2-1-2\gamma\sqrt{v_s^2(1+\gamma^2)-1}}{v_s^2(1+\gamma^2)^2} \qquad \text{E-12}$$

$$b = \frac{\gamma(v_s^2(1+\gamma^2)-2)+(1-\gamma^2)\sqrt{v_s^2(1+\gamma^2)-1}}{v_s^2(1+\gamma^2)^2} \qquad \text{E-13}$$

(see Appendix D). All velocities are scaled to the critical velocity.

Using p(r) and the vortex density, we calculated the total power used during a swirling attempt:

$$P = 2\pi \int_0^a p(r)n(r)rdr\,. \qquad \text{E-14}$$

We compared the power used by the moving vortices while finding the flow field to the theoretical power calculation to find the phase of the resonance.

$$\sin(\phi_{res}) = \frac{P}{\xi_m P_0 \frac{\eta}{h}} \qquad \text{E-15}$$

The two calculations are not compatible in that in some cases the sine of the angle was found to be greater than one. However, if it was less than one, it provided a satisfactory method for finding the Q of the resonance so that we could use Q, the splitting, and the driving frequency to determine the location of the newly shifted mode and our new position relative to it.

$$Q = \frac{\sqrt{\frac{1}{\sin^2(\phi)}} - 1}{4\left(\frac{f}{f_0} - 1\right)^2} \qquad \text{E-16}$$

$$f_{shifted} = f_0(1+\delta) \qquad \text{E-17}$$

The Q dropped similarly to experimental Q's during the simulated surf, but dropped much more rapidly as a function of shifted frequency. A plot of the theoretical surfing behavior was very foreshortened and did not resemble experimental data.

The following figures show the current progress of this program.

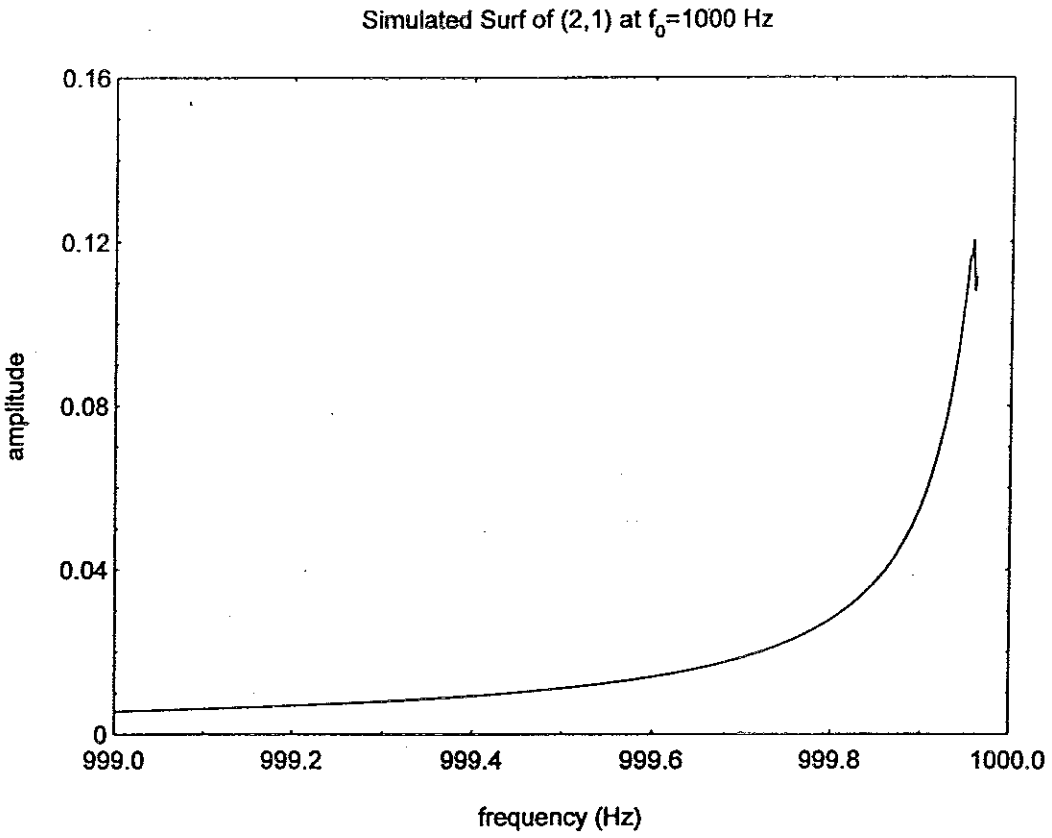

Figure E-1: The program fails to simulate the surfing behavior for more than a few frequency steps.

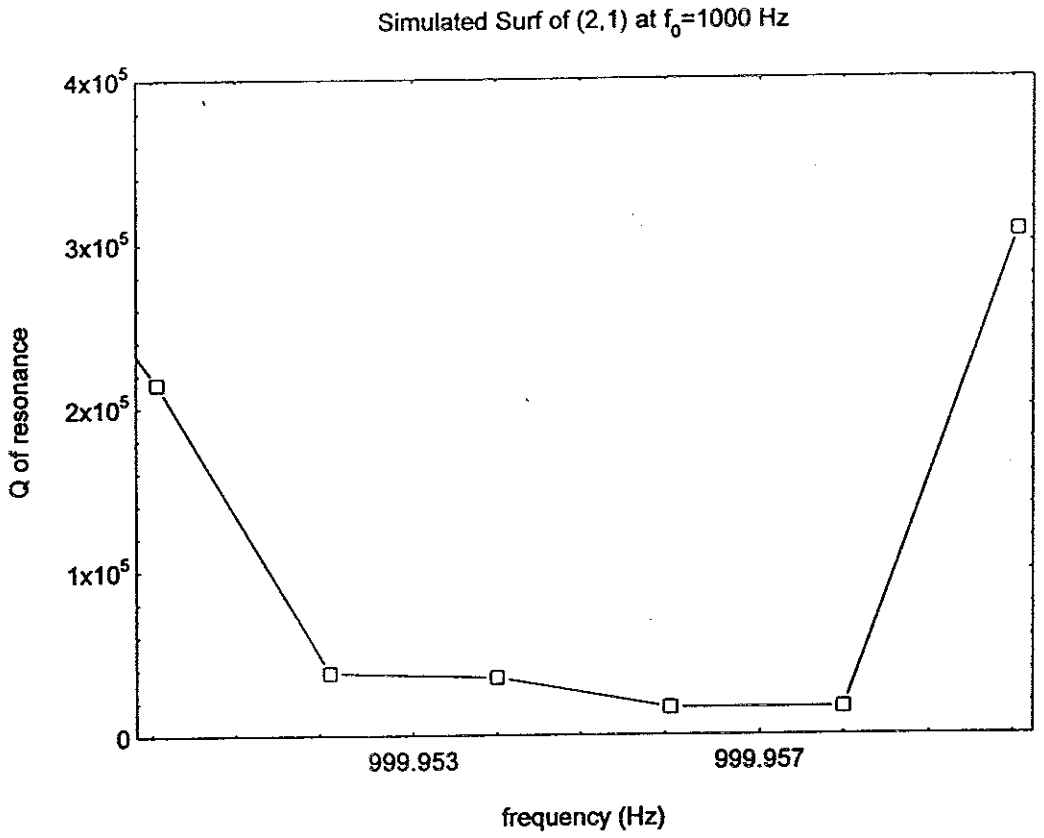

Figure E -2: The Q of the resonance drops, as it should, and is of the same order of magnitude as experimental Q's.

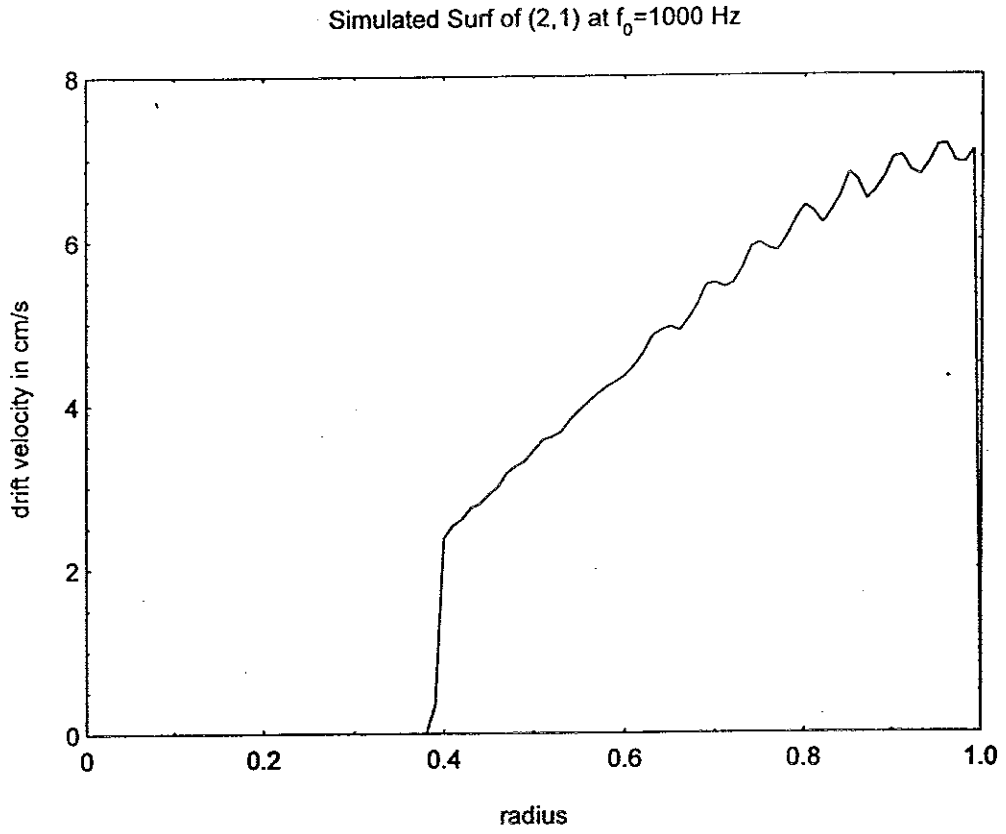

Figure E -3: The flow field generated during the simulated surf.

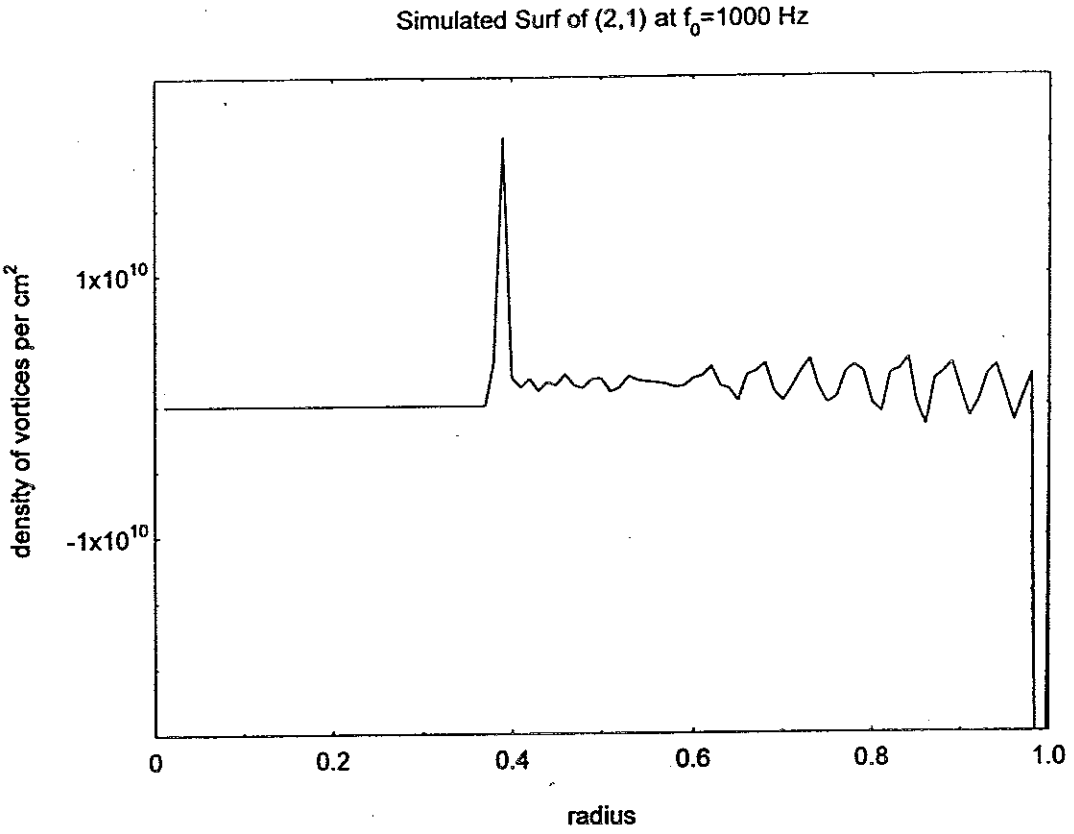

Figure E -4: The density of the vortices as arranged by the simulated surf.

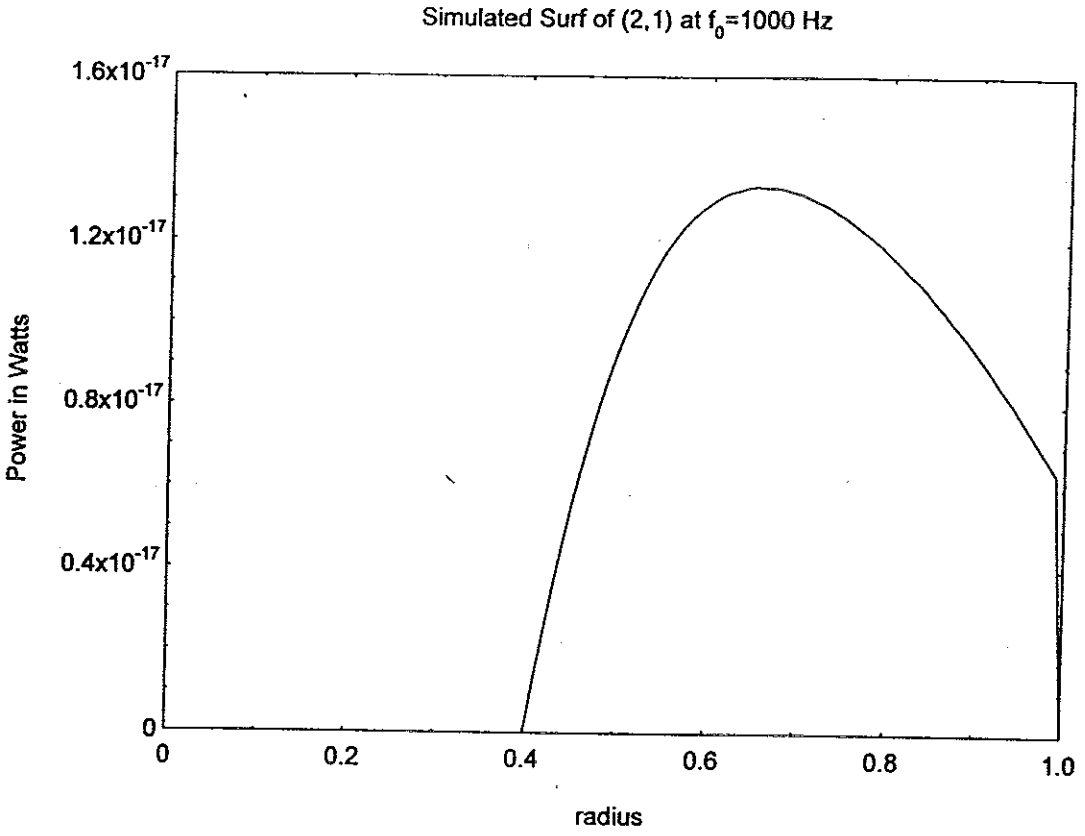

Figure E -5: The power as a function of radius that was used in the calculation of the total power used.

BIBLIOGRAPHY

Allen, J. F. and Misener, A. D., *Proc. Roy. Soc.* **A172**, 467 (1939).

Allen, J. F. and Jones, H., *Nature*, London, **141**, 243 (1938).

Andronikashvili, E. L., *Zh. eksp. theor. Fiz.*, **16**, 780 (1946).

Baierlein, R., Ellis, F. M., and Hai Luo, *J. Low Temp. Phys.*, **108**, 31 (1997).

Baierlein, R., *Newtonian Dynamics* (McGraw-Hill Book Company, New York, 1983).

Cerdonio, M., *Macroscopic Theories of Superfluids*, G.Grioli, ed. (Cambridge University Press, New York, 1991).

Cohen-Tannoudji, C., Diu, B., Laloe, F., *Quantum Mechanics* (John Wiley and Sons, New York, 1977).

Donnelly, R. J., *Quantized Vortices in Helium II* (Cambridge University Press, New York, 1991).

Ellis, F. M. and Zimmermann, C. L., *J. Low Temp. Phys.*, **101**, 475 (1995).

Ellis, F. M., Keeler, L., and Wilson, C., *Physica B*, **194-196**, 673 (1994).

Ellis, F.M.; Li, L., *Phys. Rev. Lett.*, **71**, 1577 (1993).

Henkel, R. P., Kukich G., and Reppy, J. D., *Proc. of the 11th International Conference on Low Temp. Phys.*, Allen, J. F. etc. eds. (University of St. Andrews Press, St. Andrews, Scotland, 1968).

Kapitza, P. J., *Nature*, **141**, 74 (1938).

Kittel, C. and Kroemer, H., *Thermal Physics* (W. H. Freeman and Company, New York, 1980).

Luo, Hai, Ph. D. thesis, (Wesleyan University, 1992).

Pozrikidis, C., *Introduction to Theoretical and Computational Fluid Dynamics* (Oxford University Press, New York, 1997).

Reppy, J. D. and Depatie, D., *Phys. Rev. Lett.* **12**, 187 (1964).

Tilley, D. R. and Tilley, J., *Superfluidity and Superconductivity* (Halsted Press, New

York, 1974).

Tulimeri, D., B.A. thesis (Wesleyan University, 1993).

Wilson, C. L. and Ellis, F. M., *Bull. Am. Phys. Soc.* **41**, 1688 (1996).

Wilson, C. and Ellis, F. M., *J. Low Temp. Phys.*, **101**, 507 (1995).